BABAR Analysis Document # 2566
Version 7. October 14, 2013

Exclusive $B \to \rho^0 \ell \nu$ angular analyses utilizing a hadronically reconstructed $B_{\mathbf{tag}}$ in the full *BABAR* dataset

Biplab Dey*, Owen Long and Bill Gary

[1] *UC Riverside*

*biplabd@slac.stanford.edu

Abstract

Employing the full *BABAR* dataset, we examine the process $\Upsilon(4S) \to B_{\rm tag}B_{\rm sig}(\to \rho\ell\nu)$, where the $B_{\rm tag}$ is fully reconstructed via hadronic decays, allowing for a very clean sample of $B_{\rm sig}$ events. The process $B \to \rho\ell\nu$ is completely described by the four kinematic variables $\Phi \in \{q^2, \cos\theta_\ell, \cos\theta_V, \chi\}$. We study the full 4-dimensional differential rate $d\Gamma/d\Phi$ that allows for a model-independent extraction of the hadronic form-factor shape parameters by performing a unbinned maximum likelihood fit to the data.

Contents

Chapter 1

Introduction and Theory Overview

1.1 The CKM matrix in the Standard Model

In the Standard Model (SM), the electroweak (EW) interaction part has an $SU(2)_L \times U(1)_Y$ structure. Parity is manifestly broken by the left-handed (LH) nature of the $SU(2)_L$ interaction. CP violation (CPV) here is attributed to a single source – an irreducible phase in the so-called CKM matrix. The CKM matrix rotates the quark mass or flavor eigenstates to the weak eigenstates as:

$$\begin{pmatrix} d' \\ s' \\ b' \end{pmatrix}_{weak} = \begin{pmatrix} V_{ud} & V_{us} & V_{ub} \\ V_{cd} & V_{cs} & V_{cb} \\ V_{td} & V_{ts} & V_{tb} \end{pmatrix} \begin{pmatrix} d \\ s \\ b \end{pmatrix}_{mass}, \tag{1.1}$$

and experimentally, we see evidence for a strong hierarchical structure as illustrated by the Wolfenstein parameterization:

$$V_{CKM} \sim \begin{pmatrix} 1-\lambda^2/2 & \lambda & A\lambda^3(\rho - i\eta) \\ -\lambda & 1-\lambda^2/2 & A\lambda^2 \\ A\lambda^3(1-\rho-i\eta) & -A\lambda^2 & 1 \end{pmatrix}, \tag{1.2}$$

with $\lambda \sim 0.22$, $A \sim 0.81$ and $|\rho + i\eta| \sim \mathcal{O}(1)$. Being proportional to λ^3, the element V_{ub} is one of the smallest and most difficult parameters to measure.

By construction, the CKM matrix is unitary:

$$\sum_k V_{ik} V_{jk}^* = 1. \tag{1.3}$$

The unitarity relation connecting the first and the third columns is of particular phenomenological interest and leads to "the" Unitarity Triangle (UT) as depicted in Fig. 1.1. Overdetermination of the UT (its sides and angles) and demonstrating its "closure" has been one of the major goals of High Energy Physics community and going from (a) to (b) in Fig. 1.1 demonstrates the tremendous progress over the last decade or so.

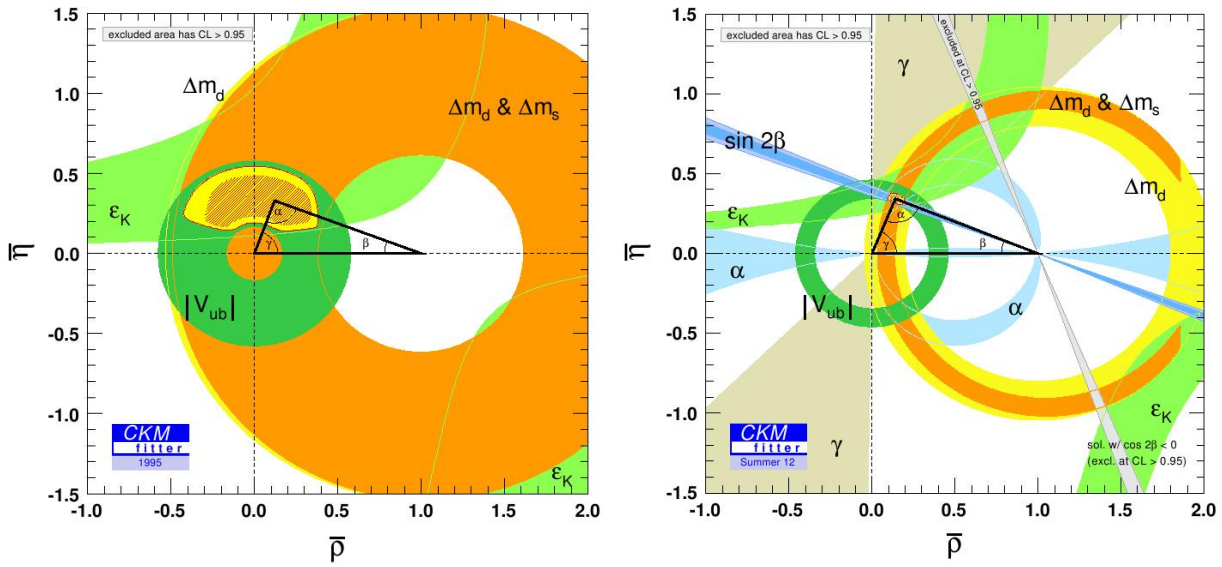

(a) (b)

Figure 1.1: The Unitarity Triangle in (a) 1995, (b) 2012. Note the impressive shrinkage of the error bands due to inputs from the B-Factory measurements. (Source: CKMFitter Group [1])

However, there are several outstanding problems that still remain. As mentioned above, the UT must "close" and any deviation from this would demonstrate a sign of beyond-the-SM (BSM) physics. For example, the angle β in Fig. 1.1 has been measured to better than 5% uncertainty (eg. from $B \to J/\psi K_s$). This constrains the length of the left side of the UT that is proportional to $|V_{ub}|/|V_{cb}|$. The elements $|V_{ub}|$ and $|V_{cb}|$ (and therefore the ratio $|V_{ub}|/|V_{cb}|$) can be measured via the processes $b \to qW^-$, where $q \in \{u, c\}$. However, since $b \to c$ is Cabbibo-favored and $b \to u$ is Cabibbo-suppressed, the relative rates are $\sim 50:1$ and the uncertainty is dominated by $|V_{ub}|$ measurements. Precision measurements of $|V_{ub}|$ are therefore of a high priority in the heavy flavor physics program in general. This is one of the goals of the current analysis, using the full *BABAR* dataset.

1.1.1 The "tension" among different $|V_{ub}|$ measurements

Given that $|V_{ub}|$ and $|V_{cb}|$ are important fundamental parameters in the SM, there is almost a whole industry dedicated to their extractions, both on the theory and experiment side (see Ref. [2] for a nice review). Roughly speaking, $|V_{ub}|$ and $|V_{cb}|$ extractions fall into two categories – exclusive and inclusive $B \to X_{u,c}\ell\nu$, depending on whether $X_{u,c}$ is exclusively detected or not. The inclusive cases involve a sum over all the exclusive modes. The measurments are complementary, employing different theoretical inputs for the QCD calculations, and different experimental signatures. However, there has been a persistent diasagreement between the inclusive and exclusive measurements at the $\sim 3\sigma$ level, as summarized in Fig. 1.2. The latest leptonic $B \to \tau\nu$ Belle results have also been included here, though the

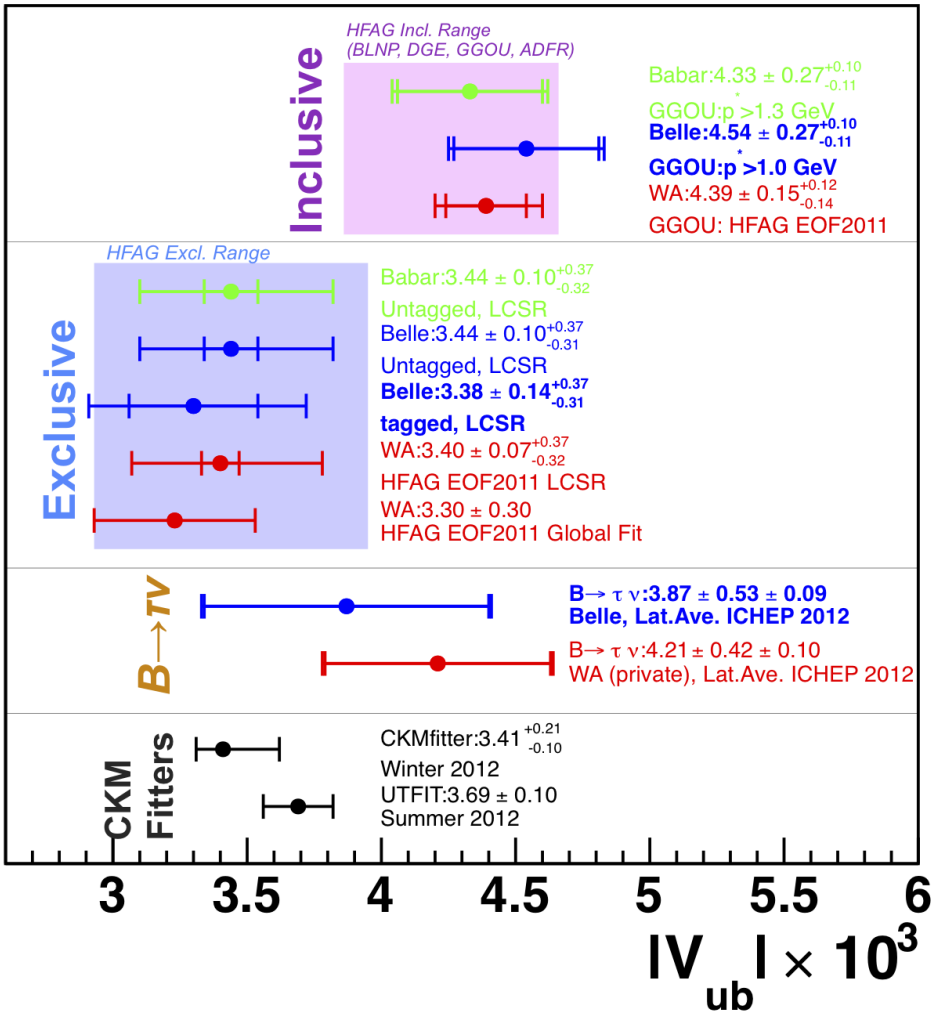

Figure 1.2: ICHEP2012 [3] status of the different $|V_{ub}|$ measurements

error bars are large.

1.1.2 Right-handed currents as a solution?

One proposal to resolve the above scenario of tensions between different $|V_{ub}|$ measurements (a smaller but non-zero tension exists in the $|V_{cb}|$ sector as well) has been to consider [4, 5, 6] a right-handed (RH) admixture in the weak charged-current. In the SM, the weak charged current is of course purely LH and breaks parity maximally. However, extensions of the SM, where the SM is seen as a low-energy effective theory, the RH admixture ϵ_R appears as a phenomenological interaction term. In the work of Buras *et al.* [6], the RH component affects $b \to uW^-$ in inclusive and exclusive semileptonic (SL) decays as well as in leptonic $B \to \tau\nu$, differently, and is seen to significantly reduce the tension. Fig. 1.3 shows a fit by Bernlochner from CKM2012 [7] to several experimental measurements incorporating the RH component.

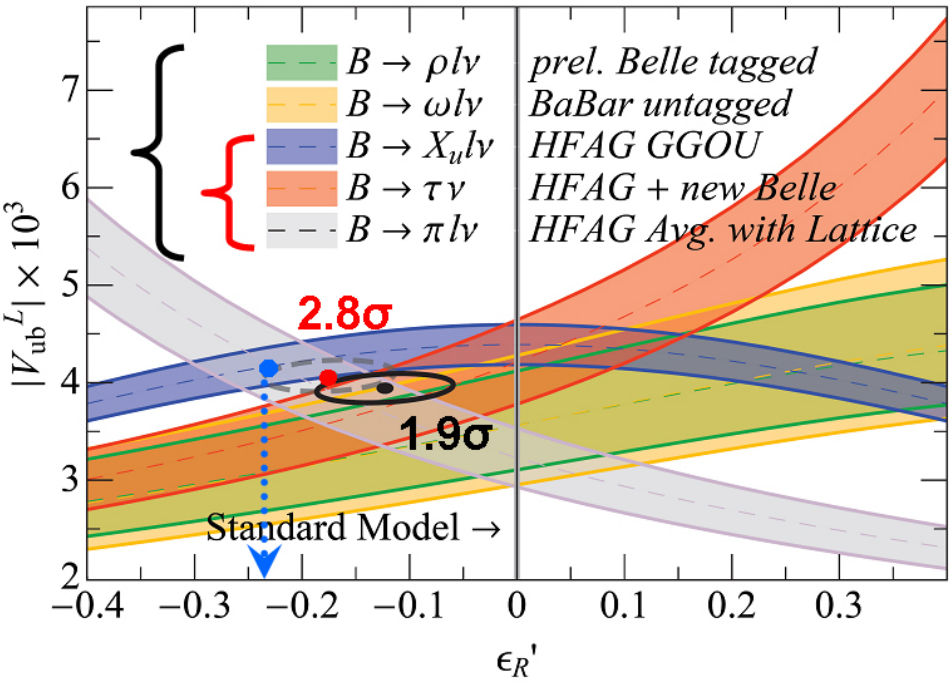

Figure 1.3: Addition of an RH admixture can resolve the tension between different $|V_{ub}|$ measurements [7].

The two most precise measurements, inclusive $B \to X_u \ell\nu$ and exclusive $B \to \pi\ell\nu$ require a rather large ϵ_R, but even a fit including the other measurements show a $\sim 2\sigma$ deviation from the SM prediction of $\epsilon_R = 0$.

As we show later, for $B \to P\ell\nu$, where P is a pseudoscalar, the effect of ϵ_R is simply an overall normalization $\sim (1+\epsilon_R)^2$, which could in principle be absorbed by the QCD calculation part as well. The vector meson case, $B \to V\ell\nu$ is however different. There are three helicity amplitudes which are affected differently (see Eq. 1.27) and the effect of the ϵ_R term can be borne out in the angular distributions, independent of the overall normalization (see work by Yang *et al.* [4]). This is one of our chief motivations for studying the angular distributions.

1.2 Theory of Semileptonic B decays

Consider the SL decay process $\bar{B}(b\bar{q}') \to X(q\bar{q}')\ell\bar{\nu}$ shown in Fig. 1.4, where $\bar{B}$ is a heavy pseudoscalar B-meson and X is a lighter outgoing meson. At the partonic level, in the SM, this is a flavor changing process where a heavy b quark emits a charged W^* (off-shell) and decays into a lighter $q \in \{u, c\}$ quark, with the decay vertex containing the CKM matrix element V_{qb}. The full amplitude is of the form

$$\mathcal{M} = \frac{G_F V_{qb}}{\sqrt{2}} \left([H_\mu L^\mu]_{SM} + [H_S L_S]_{NP} \right), \tag{1.4}$$

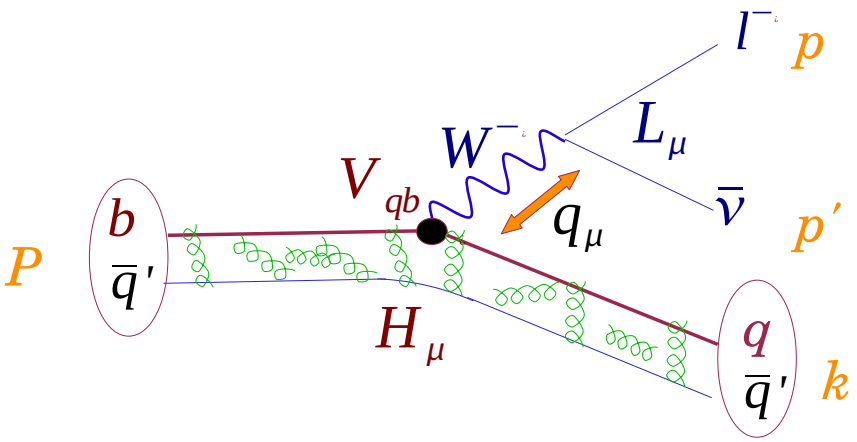

Figure 1.4: The SL B decay $\bar{B}(b\bar{q}') \to X(q\bar{q}')\ell\bar{\nu}$ in the SM.

where the SM part consists of leptonic (L_μ) and hadronic (H_μ) charged currents (spin-1) and we have included new physics (NP) contributions in terms of the exchange of a scalar particle (spin-0). The complicated non-perturbative QCD interactions reside only on the hadronic side. The momentum transfer squared between the leptonic and hadronic systems is typically denoted by q^2. The hadronic side is "probed" by the q^2 dependent form-factors, just like in deep inelastic scattering (DIS), save that $q^2 > 0$ is now timelike, instead of spacelike in the DIS case.

1.2.1 Kinematics

We follow the notation in Gilman *et al.* [8] where the 4-momenta are P, k, p and p' for the parent $\bar{B}(b\bar{q}')$, the daughter $X(q\bar{q}')$, ℓ and ν, respectively. The W^* 4-momentum is $q = (P - k)$, so that

$$q^2 = (P-k)^2 = m_B^2 + m_X^2 - 2m_B E_X \tag{1.5a}$$

$$w \equiv v_B \cdot v_X = \frac{P}{m_B} \cdot \frac{k}{m_X} = \frac{E_X}{m_X} = \gamma_X = \frac{m_B^2 + m_X^2 - q^2}{2m_B m_X}, \tag{1.5b}$$

where E_X and $\mathbf{k}$ are the energy and 3-momentum magnitude of X in the B rest frame (RF). At "zero-recoil", $\mathbf{k} = 0$, $q^2 = q^2_{\rm max} = (m_B - m_X)^2$, and $w = w_{\rm min} = 1$. Let E_ℓ be the lepton energy in the B RF. Similarly, in the W^* RF, define θ_ℓ as the polar angle with the W^*

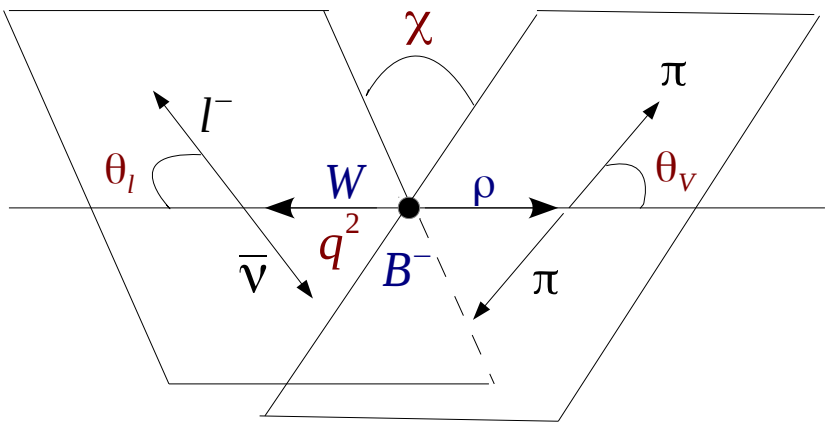

Figure 1.5: The four kinematic variables $\Phi \in \{q^2, \chi, \cos\theta_\ell, \cos\theta_V\}$ for the decay chain $B \to \rho(\to \pi\pi)W^*(\to \ell\nu)$.

momentum direction in the B RF as shown in Fig. 1.5. Following Refs. [9, 10],

$$\mathbf{k} = \sqrt{\frac{(m_B^2 - q^2 + m_X^2)^2}{4m_B^2} - m_X^2} \tag{1.6a}$$

$$E_\ell^{\max,\min} = \frac{1}{2m_B}\left((m_B^2 + q^2 - m_X^2)/2 \pm m_B\mathbf{k}\right) \tag{1.6b}$$

$$E_\ell = \frac{1}{2}\left((E_\ell^{\max} + E_\ell^{\min}) + (E_\ell^{\max} - E_\ell^{\min})\cos\theta_\ell\right) \tag{1.6c}$$

which means that out of the set $\{q^2, E_\ell, \cos\theta_\ell\}$, only two are independent variables. For a given q^2, E_ℓ is of course bound between $E_\ell^{\max,\min}$. For a given E_ℓ, q^2 is bound as

$$0 \le q^2 \le 2m_B E_\ell + \frac{2m_X^2 E_\ell}{2E_\ell - m_B}. \tag{1.7}$$

The lepton energy end-point, ocurring at $q^2 \to 0$ is given as

$$E_\ell^{\max} = \frac{m_B^2 - m_X^2}{2m_B}, \tag{1.8}$$

which is around 2.3 GeV for $B \to D\ell\nu$ and 2.6 GeV for $B \to \rho\ell\nu$. The variable w can be interpreted as the γ factor of X in the mother B RF, so that

$$\mathbf{k} = m_X\sqrt{w^2 - 1}. \tag{1.9}$$

The maximum value of w is at $q^2 = 0$, when the hadronic system is most distrurbed, and is given by

$$w_{\max} = \frac{m_B^2 + m_X^2}{2m_B m_X}, \tag{1.10}$$

Vector meson decay	$\vec{A}$ direction
$D^* \to D\pi$	$\vec{p}_D$
$D^* \to D\gamma$	$\vec{p}_D$
$\rho^\pm \to \pi^\pm\pi^0$	$\vec{p}_{\pi^0}$
$\rho^0 \to \pi^+\pi^-$	$\vec{p}_{\pi^+}$
$\omega \to \pi^+\pi^-\pi^0$	$\vec{p}_{\pi^+} \times \vec{p}_{\pi^-}$

Table 1.1: The analyzing direction $\vec{A}$ in Fig. 1.6 for the different vector mesons.

whence,

$$\mathbf{k}_{\max} = \frac{m_B^2 - m_X^2}{2m_B}. \tag{1.11}$$

When the outgoing meson in a vector meson, its polarization is important as well. For $\rho \to \pi\pi$ shown in Fig. 1.5, the analyzer ($\hat{A}$) is the π momentum direction in the ρ helicity frame with respect to the B RF. For $\omega \to \pi^+\pi^-\pi^0$, the normal to the ω decay plane plays the role of the analyzer. The last additional kinematic variable is χ, the dihedral angle between the W and the vector meson decay planes in the mother B RF. The calculation of the three angular variables for the vector meson case are described next.

1.2.1.1 Sign conventions for the angles θ_ℓ, θ_V and χ

We follow the definition of the angles in Fig. 2 of Gilman-Singleton [8], which is also followed by Richman-Burchat [9]. We first boost everything to the B RF. There are two sets of co-ordinate axes, $\{\hat{x}_\ell, \hat{y}_\ell, \hat{z}_\ell\}$ and $\{\hat{x}_V, \hat{y}_V, \hat{z}_V\}$, as shown in Fig. 1.6a. These are basically the helicity frames of the W^* and the V. The connection is that $\hat{x}_\ell \equiv -\hat{x}_V$, $\hat{y}_\ell \equiv \hat{y}_V$ and $\hat{z}_\ell \equiv -\hat{z}_V$. The dihedral angle $\chi = \varphi_\ell + \varphi_V$, where we note that the azimuthal angles φ_ℓ and φ_V are calculated in two different frames. We set $\varphi_\ell = 0$ by ensuring that the charged lepton ℓ lies in the $\hat{x}_\ell$-$\hat{z}_\ell$ plane and and has the x-component of its momentum > 0. This completely fixes the quadrant of χ. To measure θ_ℓ and θ_V, we boost to the W^* and V rest frames and measure the polar angles of the ℓ and $\vec{A}$, respectively. Here $\vec{A}$ is the analyzing dierction of the vector meson decay as tabulated in Table 1.1.

Korner-Schuler [11] and Hagiwara [12, 13] follow a slightly different convention where both the orientations of the axes for the leptonic and hadronic systems are the same. The relations are

$$\theta_\ell^{\rm KS} \equiv \pi - \theta_\ell^{\rm GS} \tag{1.12a}$$
$$\theta_V^{\rm KS} \equiv \theta_V^{\rm GS} \tag{1.12b}$$
$$\chi^{\rm KS} \equiv \pi + \chi^{\rm GS} \tag{1.12c}$$

where the "KS" superscript refers to Korner-Schuler/Hagiwara and the "GS" superscript to Gilman-Singleton/Richman-Burchat. We use the GS conventions here.

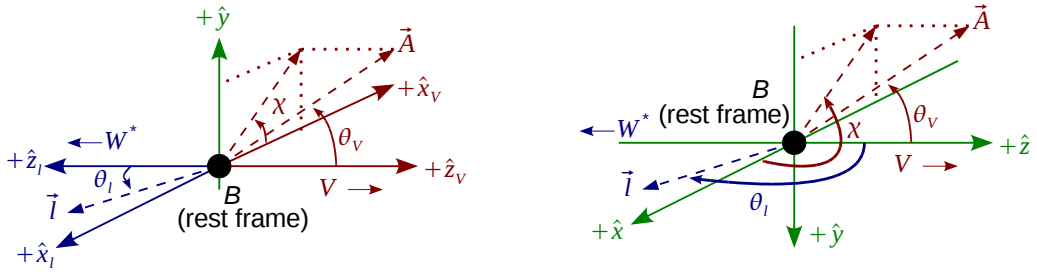

(a) (b)

Figure 1.6: The reference frames for calculating θ_ℓ, θ_V and χ for $B \to VW^*(\to \ell\nu)$ conforming to (a) Fig. 2 in Gilman-Singleton [8] and (b) Fig. 3 in Hagiwara [13]. The relations between the two sets of angles are given in the text.

1.2.1.2 The B polar angle θ_B

Spin-parity dictates that the decay $\Upsilon(4S) \to B\overline{B}$ is a pure P-wave decay with a $\sin^2\theta_B$ distribution, where θ_B is the helicity angle of the B's in the overall c.m. frame. Therefore, in addition to the four angular variables (q^2, $\cos\theta_\ell$, $\cos\theta_V$, χ) introduced earlier, θ_B is yet another independent variable that the full production rate is dependent on.

The P-wave distribution can be utilized to project out the true $e^+e^- \to \Upsilon(4S) \to B\bar{B}$ events, provided the background distribution does not have any $\sin^2\theta_B$ contribution. To project out the P-wave part, we note that

$$\frac{dN_{B\bar{B}}}{d\cos\theta_B} = \frac{3N_{B\bar{B}}}{4}\sin^2\theta_B = N_B\overline{B}\left(\frac{1}{\sqrt{2}}P_0(\theta_B) - \frac{1}{\sqrt{10}}P_2(\theta_B)\right), \tag{1.13}$$

where P_i's are the orthonormal Legendre polynomials. Using the orthonormal property, we have

$$\int_{-1}^{1} -\sqrt{10}P_2(\theta_B)\frac{dN_{B\bar{B}}}{d\cos\theta_B}d\cos\theta_B = N_{B\bar{B}}, \tag{1.14}$$

so that the coefficient $-\sqrt{10}P_2(\theta_B) = 2.5(1-3\cos^2\theta_B)$ can be used as weight for each event, to project out the true $B\overline{B}$ events.

1.2.2 Effective Hamiltonians

Consider the process $b \to q\ell\bar{\nu}_\ell$ (where $q \in \{c,u\}$ and $\ell \in \{e,\mu\}$) in terms of an effective 4-Fermi interaction effective Hamiltonian:

$$\mathcal{H}_{\text{eff}} = \frac{2G_F V_{bq}^L}{\sqrt{2}}\left[\left(g^V\bar{q}\gamma_\mu b - g^A\bar{q}\gamma_\mu\gamma_5 b\right)\bar{\ell}\gamma^\mu\nu_L + \bar{q}\left(g^S + g^P\gamma_5\right)b\bar{\ell}\nu_L\right], \tag{1.15}$$

where we have assumed only LH neutrinos ($\nu_L = \frac{1-\gamma_5}{2}\nu$) and neglected any tensor terms associated with baryon and lepton number violations (leptoquark models [14]). Here, $V_{bq}^L \equiv V_{bq}$

denotes the usual LH CKM matrix element in the SM. The vector and the axial interactions are written as $g_V = (1 + \epsilon_R)$ and $g_A = (1 - \epsilon_R)$ and in general, ϵ_R is allowed to be complex [15] to incorporate additional CP violating effects. There are also two terms, g^S and g^P, corresponding to scalar and pseudoscalar interactions, respectively. To retrieve the SM part, one puts $\epsilon_R = g^S = g^P = 0$.

1.2.2.1 The $\bar{B} \to V\ell\bar{\nu}_\ell$ case

The transition matrix element pertaining to the process $\bar{B} \to V\ell^-\bar{\nu}$ is then $\mathcal{M} = \langle V|\mathcal{H}_{\rm eff}|\bar{B}\rangle$, which is of the form written in Eq. 1.4. We note that a charged lepton and a RH anti-neutrino is being produced (since we have allowed for extra phases, we have to be careful about CP conjugates now). The hadronic matrix elements corresponding to the terms $g^{\{V,A,P,S\}}$ are written as [16]:

$$\langle V|\bar{q}\gamma_\mu b|B\rangle_V = \frac{2iV(q^2)}{m_V + m_B}\epsilon_{\mu\nu\alpha\beta}\varepsilon_V^{*\nu}p_V^\alpha p_B^\beta \tag{1.16a}$$

$$\begin{aligned}\langle V|\bar{q}\gamma_\mu\gamma_5 b|B\rangle_A &= 2m_V A_0(q^2)\frac{\varepsilon_V^*\cdot q}{q^2}q_\mu + (m_B + m_V)A_1(q^2)\left(\varepsilon_{\mu V}^* - \frac{\varepsilon_V^*\cdot q}{q^2}q_\mu\right)\\ &\quad - A_2(q^2)\frac{\varepsilon_V^*\cdot q}{m_B + m_V}\left((p_B + p_V)_\mu - \frac{m_B^2 - m_V^2}{q^2}q_\mu\right)\end{aligned} \tag{1.16b}$$

$$\langle V|\bar{q}\gamma_5 b|B\rangle_P \approx 2m_V A_0(q^2)\frac{\varepsilon_V^*\cdot q}{m_b + m_q} \tag{1.16c}$$

$$\langle V|\bar{q}b|B\rangle_S = 0, \tag{1.16d}$$

where Eq. 1.16c is derived from Eq. 1.16b dotting with $q_\mu = (p_B - p_V)_\mu$ and using the Dirac equation at the quark level. Note the scalar component is zero because of the spin-parity of B and V. Also, for the light leptons, the q^μ terms in Eq. 1.16b go to zero when dotted with the leptonic charged current. Hence, the matrix element is:

$$\begin{aligned}\mathcal{M}_V = \frac{2G_F V_{bq}}{\sqrt{2}}\Bigg\{\Bigg[&g_V\left(\frac{2iV(q^2)}{m_V + m_B}\epsilon_{\mu\nu\alpha\beta}\varepsilon_V^{*\nu}p_V^\alpha p_B^\beta\right)\\ &- g^A\left((m_B + m_V)A_1(q^2)\varepsilon_{V\mu}^* - A_2(q^2)\frac{\varepsilon_V^*\cdot q}{m_B + M_V}(p_B + p_V)_\mu\right)\Bigg]\bar{\ell}\gamma^\mu\nu_L\\ &- g^P\left(\frac{2m_B}{m_b + m_q}\varepsilon_V^*\cdot q\ A_0(q^2)\right)\bar{\ell}\nu_L\Bigg\}.\end{aligned} \tag{1.17}$$

1.2.2.2 The $\bar{B} \to P\ell\bar{\nu}_\ell$ case

The QCD terms in this case are [16]:

$$\langle P|\bar{q}\gamma_\mu b|B\rangle_V = f_+(q^2)\left((p_B+p_P)_\mu - \frac{(p_B+p_P)\cdot q}{q^2}q_\mu\right) + f_0(q^2)\frac{(p_B+p_P)\cdot q}{q^2}q_\mu \tag{1.18a}$$

$$\langle P|\bar{q}\gamma_\mu\gamma_5 b|B\rangle_A = 0 \tag{1.18b}$$

$$\langle P|\bar{q}\gamma_5 b|B\rangle_P = 0 \tag{1.18c}$$

$$\langle P|\bar{q}b|B\rangle_S \approx f_0(q^2)\frac{m_B^2 - m_P^2}{m_b + m_q}, \tag{1.18d}$$

so that the matrix element (again, neglecting q_μ terms for the light leptons) is:

$$\mathcal{M}_P = \frac{2G_F V_{bq}}{\sqrt{2}}\left\{g_V f_+(q^2)(p_B+p_P)_\mu \bar{\ell}\gamma^\mu\nu_L + g_S f_0(q^2)\frac{m_B^2 - m_P^2}{m_b+m_q}\bar{\ell}\nu_L\right\} \tag{1.19}$$

1.2.3 Differential rate for $\bar{B} \to X\ell\bar{\nu}_L$

Following Hagiwara [12, 13], the differential rate is

$$d\Gamma = \frac{1}{2m_B}\sum_{\text{final spins}}|\mathcal{M}|^2 d\Phi_3, \tag{1.20}$$

where the incoherent sum is over the spins of all final-state particles and three-body $X\ell\bar{\nu}$ phase-space factor is

$$d\Phi_3 = \frac{\mathbf{k}}{2m_B}\frac{dq^2 d\cos\theta_\ell}{(4\pi)^3}. \tag{1.21}$$

where $\mathbf{k}$ is the usual X 3-momentum magnitude in the B RF. The invariant amplitude (see Eqs. 1.19 and 1.17) is of the form

$$\mathcal{M} = \frac{G_F V_{bq}}{\sqrt{2}}\left\{\sum_{\lambda\in\{0,\pm1\}} L_\lambda \mathcal{H}_\lambda + (\mathcal{H}_P + \mathcal{H}_S)L_S\right\}. \tag{1.22}$$

where λ is the helicity of the hadronic system X. Since parent B meson is has spin-0, the helcities of the hadronic and the leptonic systems have to be the same. The hadronic helicity amplitudes are defined as [17]

$$\mathcal{H}_\lambda = \left(\varepsilon^*_{W^*}(\lambda)\right)_\mu \langle X(\lambda)|J^\mu|\bar{B}\rangle, \tag{1.23}$$

with the spin-quantization axis is along the X direction in the B RF, while the leptonic helicity amplitudes are

$$L_\lambda = 2\left(\varepsilon_{W^*}(-\lambda)\right)_\mu \bar{u}_\ell\gamma^\mu\nu_L = 2\sqrt{2q^2}d^1_{\lambda,(-\eta)}(\theta_\ell) \tag{1.24}$$

where the spin-quantization axis is along the W^* direction in the B RF, opposite to the X direction (conforming to GS, but not Hagiwara!). Note that $\eta = +1$ for $(\ell^-\bar{\nu})$ in the final state, and $\eta = -1$ for $(\ell^+\nu)$ as explained in Eq. 2.13' of Ref. [8]. This arises because of the outgoing neutrino(anti-neutrino) is left(right)-handed, so that the $\ell^-(\ell^+)$ can have only a negative(positive) helicity, in the limit of massless leptons.

On the other hand, for the scalar term L_S, the helicities of the $\ell^-/\bar{\nu}$ or ℓ^+/ν must be the same, since the total spin of the $\ell\nu$ system is 0. This means, that although [12, 13] $\bar{\ell}\nu_L = \sqrt{q^2}$, so that

$$L_S = 2\bar{\ell}\nu_L = 2\sqrt{q^2}, \tag{1.25}$$

the final spins of the ℓ for the L_λ and L_S cases are different and the two terms must add incoherently in total rate expression. The scalar terms for the massless lepton case are therefore second order corrections, relative to the SM, and will be neglected henceforth.

1.2.3.1 The $\bar{B} \to V\ell\bar{\nu}_\ell$ case

For the case where X is a vector-meson

$$\begin{aligned}\langle V(\lambda)|J^\mu|\bar{B}\rangle = (1+\epsilon_R)&\left(\frac{2iV(q^2)}{m_V+m_B}\epsilon_{\mu\nu\alpha\beta}\varepsilon_V^{*\nu}p_V^\alpha p_B^\beta\right)\\ -\ (1-\epsilon_R)&\left((m_B+m_V)A_1(q^2)\varepsilon^*_{V\mu} - A_2(q^2)\frac{\varepsilon_V^*\cdot q}{m_B+M_V}(p_B+p_V)_\mu\right)\end{aligned} \tag{1.26}$$

The expressions for the three hadronic helicity amplitudes $\mathcal{H}_\lambda$ have been calculated elsewhere [11]:

$$\mathcal{H}_0 = \frac{1-\epsilon_R}{2m_V\sqrt{q^2}}\left((m_B^2-m_V^2-q^2)(m_B+m_V)A_1(q^2) - \frac{4m_B^2\mathbf{k}^2}{m_B+m_V}A_2(q^2)\right) \tag{1.27a}$$

$$\mathcal{H}_\pm = (m_V+m_B)(1-\epsilon_R)A_1(q^2) \mp \frac{2m_B(1+\epsilon_R)\mathbf{k}}{(m_B+m_V)}V(q^2). \tag{1.27b}$$

For the case where the vector-meson decays into two spin-0 pseudoscalars, the amplitude $\mathcal{M}$ becomes

$$\mathcal{M} = \frac{G_F V_{bq}}{\sqrt{2}}\left\{\sum_{\lambda\in\{0,\pm1\}}\mathcal{H}_\lambda L_\lambda Y_\lambda\right\} \tag{1.28}$$

where the Y_λ's are the spherical harmonics describing the spin-1 vector meson decay into two spin-0 particles

$$Y_\lambda = Y_\lambda^1(\theta_V,\chi) = \sqrt{\frac{3}{4\pi}}e^{i\lambda\chi}d^1_{\lambda,0}(\theta_V). \tag{1.29}$$

and the differential phase-space element is now $d\Phi = d\Phi_3 d\cos\theta_V d\chi$

Putting everything together, the full expression for the 4-D differential rate for V decaying to two pseudoscalars is then

$$\begin{aligned}\frac{d\Gamma}{d\Phi} &= \frac{3G_F|V_{qb}|^2\mathbf{k}q^2\mathcal{B}^{V\to P_1P_2}}{m_B^2(4\pi)^4}\left|\sum_{\lambda\in\{0,\pm1\}}\mathcal{H}_\lambda d^1_{\lambda,0}(\theta_V)d^1_{\lambda,(-\eta)}(\theta_\ell)e^{i\lambda\chi}\right|^2 \\ &= \frac{3G_F|V_{qb}|^2\mathbf{k}q^2\mathcal{B}^{V\to P_1P_2}}{8m_B^2(4\pi)^4} \\ &\quad\times\left|2\cos\theta_V(-\eta\mathcal{H}_0\sin\theta_\ell)-\sin\theta_V\mathcal{H}_{+1}(1-\eta\cos\theta_\ell)e^{i\chi}+\sin\theta_V\mathcal{H}_{-1}(1+\eta\cos\theta_\ell)e^{-i\chi}\right|^2\end{aligned} \tag{1.30}$$

where $\eta = +1(-1)$ corresponds to $\bar{B}\to V\ell^-\bar{\nu}\,(B\to V\ell^+\nu)$. For the $\bar{B}\to V\ell^-\bar{\nu}$ SM part, this is the same as Eq. 113 in Ref. [9].

For $V\to P_1\gamma$, we need to incoherently sum over the outgoing photon helicity ±1 cases separately:

$$\begin{aligned}\frac{d\Gamma}{d\Phi} &= \frac{3G_F|V_{qb}|^2\mathbf{k}q^2\mathcal{B}^{V\to P_1\gamma}}{m_B^2(4\pi)^4}\sum_{\lambda_\gamma=\pm1}\frac{1}{2}\left|\sum_{\lambda\in\{0,\pm1\}}\mathcal{H}_\lambda d^1_{\lambda,\lambda_\gamma}(\theta_V)d^1_{\lambda,(-\eta)}(\theta_\ell)e^{i\lambda\chi}\right|^2 \\ &= \frac{3G_F|V_{qb}|^2\mathbf{k}q^2\mathcal{B}^{V\to P_1\gamma}}{32m_B^2(4\pi)^4} \\ &\quad\times\sum_{\lambda_\gamma=\pm1}\Big|2\lambda_\gamma\sin\theta_V(-\eta\mathcal{H}_0\sin\theta_\ell)+\mathcal{H}_{+1}(1+\lambda_\gamma\cos\theta_V)(1-\eta\cos\theta_\ell)e^{i\chi} \\ &\qquad\qquad+\mathcal{H}_{-1}(1-\lambda_\gamma\cos\theta_V)(1+\eta\cos\theta_\ell)e^{-i\chi}\Big|^2\end{aligned} \tag{1.31}$$

where the extra factor of $\frac{1}{2}$ ensures normalization to the appropriate branching fractions (BF).

In the case of complex $\mathcal{H}_i$'s, we incorporate the complex phases as

$$\mathcal{H}_i \to H_i e^{i\delta_i'} \tag{1.32}$$

where the H_i remain real and only relative phases $\delta_\pm = (\delta_\pm' - \delta_0')$ matter.

1.2.3.2 The $\bar{B}\to P\ell\bar{\nu}_\ell$ case

Following the calculations in Ref. [13] one can show that the amplitude in Eq. 1.18 boils down to

$$\mathcal{M}_P = \frac{G_F V_{qb}}{\sqrt{2}}g_V(-4m_B\mathbf{k}\sin\theta_\ell f_+(q^2)), \tag{1.33}$$

where we have neglected the g_S term because, as explained above, it is a small second order correction to the SM. Plugging this into Eqs. 1.20 and 1.21, we get

$$\frac{d\Gamma}{d\Phi} = \frac{G_F^2 |V_{qb}|^2}{32\pi^3} \mathbf{k}^3 \sin^2\theta_\ell |g_V f_+(q^2)|^2, \tag{1.34}$$

where $d\Phi = dq^2 d\cos\theta_\ell$.

1.2.3.3 Numerical factors

To convert the above equations into a differential rate of the number of events, we multiply by the factor

$$\frac{N_{B\bar{B}}}{\Gamma_{B\bar{B}}} = \frac{\mathcal{L}\sigma_{B\bar{B}}}{\hbar/\tau_B} \tag{1.35}$$

where the on-peak luminosity is $\mathcal{L} = 424.25\times10^6/\text{nb}$, the cross-sections are $\sigma_{B^+B^-} = 0.568$ nb and $\sigma_{B^0\bar{B}^0} = 0.532$ nb, the B lifetimes are $\tau_{B^+} = 1.641 \pm 0.008$ ps and $\tau_{B^0} = 1.519 \pm 0.007$ ps, and $\hbar = 6.58211\times10^{-10}$ GeV-ps. We also note that the numerical value of the Fermi constant is $G_F/(\hbar c)^3 = 1.166 \times 10^{-5}$ GeV^{-2}.

1.2.3.4 Isospin Relations

For $b \to u$ transitions, keeping in mind that π^0, ρ^0 and ω have the u-quark flavor content $u\bar{u}/\sqrt{2}$, we get the relations:

$$\begin{aligned}
d\Gamma(B^0 \to \pi^-\ell^+\nu) &= 2d\Gamma(B^+ \to \pi^0\ell^+\nu) && \text{(1.36a)}\\
d\Gamma(B^0 \to \rho^-\ell^+\nu) &= 2d\Gamma(B^+ \to \rho^0\ell^+\nu) && \text{(1.36b)}\\
d\Gamma(B^+ \to \omega\ell^+\nu) &= d\Gamma(B^+ \to \rho^0\ell^+\nu). && \text{(1.36c)}
\end{aligned}$$

In other words, the form-factors for the neutral π and ρ are $1/\sqrt{2}$ times that of the charged versions.

1.2.4 CP conjugate processes

It can shown [18, 19, 20, 21] that (assuming no direct CP violation) for the CP conjugate processes, $V(q^2)$ (in Eq. 1.16a) and $f_+(q^2)$ (Eq. 1.18) get sign flips while the axial form-factors stay the same. Also, the weak-phases should be negated. For $B \to P\ell\nu$ ignoring charged-scalar exchange NP terms for the $\ell = e/\mu$ case, Eq. 1.34 remains CP-invariant. For the $B \to V\ell\nu$ case, we can connect the CP-conjugate amplitudes as:

$$\begin{aligned}
\overline{\mathcal{H}_0} &= \mathcal{H}_0^* && \text{(1.37a)}\\
\overline{\mathcal{H}_\pm} &= \mathcal{H}_\mp^* && \text{(1.37b)}\\
\overline{\mathcal{M}}(\theta_\ell, \theta_V, \chi) &= -\mathcal{M}^*(\theta_\ell, \theta_V, -\chi) && \text{(1.37c)}
\end{aligned}$$

The expressions in Eqs. 1.30 and 1.31 can then be summarized as:

$$\frac{d\Gamma}{d\Phi} = \left[\frac{\mathcal{C}'}{1+(1-\alpha)/2}\right] \times \left\{ \left[H_+^2(1-\cos\theta_\ell)^2 + H_-^2(1+\cos\theta_\ell)^2\right](1-\alpha\cos^2\theta_V) + 4H_0^2\sin^2\theta_\ell\left(\frac{1-\alpha}{2} + \alpha\cos^2\theta_V\right) - 2\alpha H_0\sin\theta_\ell\sin 2\theta_V\left[H_+(1-\cos\theta_\ell)\cos(\eta\chi+\delta_+) - H_-(1+\cos\theta_\ell)\cos(\eta\chi-\delta_-)\right] - 2\alpha H_+H_-\sin^2\theta_\ell\sin^2\theta_V\cos(2\eta\chi+(\delta_+-\delta_-))\right\}, \quad (1.38)$$

where α is -1 for $V \to P\gamma$ (such as $D^* \to D\gamma$ or $\omega \to \pi\gamma$) and +1 for $V \to P_1P_2$ (such as $\rho \to \pi\pi$ or $D^* \to D\pi$) type decays. The prefactor term is

$$\mathcal{C}' = \frac{3}{8(4\pi)^4}G_F^2|V_{bq}|^2\frac{\mathbf{k}q^2}{m_B^2}\mathcal{B} \quad (1.39)$$

where the term $\mathcal{B}$ accomodates any BF's from the vector meson decay chain onwards. As earlier, $\eta = +1$ involves the $\bar{B}$ decay and $\eta = -1$ involves the B. Note that *physically*, in Eq. 1.38 the $H_\pm$ corresponds to that in $\overline{B} \to \rho\ell^-\overline{\nu}_\ell$, since it was written out for $\eta = +1$.

1.2.4.1 Expansion in an orthonormal basis

Eq. 1.38 can be conveniently expanded in an orthonormal basis of angular functions $f_i(\theta_\ell, \theta_V, \chi)$ as follows

$$\frac{d\Gamma}{dq^2 d\cos\theta_\ell d\cos\theta_V d\chi} = \mathcal{C}' \times \left\{ \sum_{i=1}^{12} f_i(\theta_\ell, \theta_V, \chi)\Gamma_i(q^2) \right\}, \quad (1.40)$$

where orthonormality implies

$$\int_{-1}^{1}\int_{-1}^{1}\int_{0}^{2\pi} f_i(\theta_\ell, \theta_V, \chi) f_j(\theta_\ell, \theta_V, \chi)\, d\cos\theta_\ell d\cos\theta_V d\chi = \delta_{ij}. \quad (1.41)$$

The 12 set of functions are tabulated in Table 1.2. Here $Y_m^l \equiv Y_m^l(\theta_\ell, \chi)$ are the spherical harmonics and $P_m^l \equiv \sqrt{2\pi}Y_m^l(\cos\theta_V, 0)$. The SM and BSM terms are borne out separately in a clear fashion. The set of first nine functions are T-odd, there being at the most a $\cos\delta$ dependence on the phase. The last three functions depend on $\sin\delta$ and are T-odd.

The orthonormality of the f_i functions imply that in a given q^2 bin, after acceptance correction, the individual Γ_i functions can be projected out as

$$\int_{-1}^{1}\int_{-1}^{1}\int_{0}^{2\pi} \frac{f_i(\theta_\ell, \theta_V, \chi)}{\mathcal{C}'}\left[\frac{d\Gamma}{d\cos\theta_\ell d\cos\theta_V d\chi}\right]_{\text{acc. corr.}} d\cos\theta_\ell d\cos\theta_V d\chi = \Gamma_i. \quad (1.42)$$

This is therefore a completely model-independent method for extraction the form-factors.

	i	f_i	Γ_i	
			$V \to P_1 P_2$	$V \to P\gamma$
T-even	1	$P_0^0 Y_0^0$	$H_0^2 + H_+^2 + H_-^2$	$H_0^2 + H_+^2 + H_-^2$
	2	$P_0^0 Y_1^0$	$-\frac{\sqrt{3}}{2}\left(H_+^2 - H_-^2\right)$	$-\frac{\sqrt{3}}{2}\left(H_+^2 - H_-^2\right)$
	3	$P_2^0 Y_1^0$	$\frac{1}{2}\sqrt{\frac{3}{5}}\left(H_+^2 - H_-^2\right)$	$-\frac{1}{4}\sqrt{\frac{3}{5}}\left(H_+^2 - H_-^2\right)$
	4	$P_2^0 Y_0^0$	$-\frac{2}{\sqrt{5}}\left\{(H_+^2 + H_-^2)/2 - H_0^2\right\}$	$\frac{1}{\sqrt{5}}\left\{(H_+^2 + H_-^2)/2 - H_0^2\right\}$
	5	$P_0^0 Y_2^0$	$\frac{1}{\sqrt{5}}\left\{(H_+^2 + H_-^2)/2 - H_0^2\right\}$	$\frac{1}{\sqrt{5}}\left\{(H_+^2 + H_-^2)/2 - H_0^2\right\}$
	6	$P_2^0 Y_2^0$	$-\frac{2}{5}\left\{(H_+^2 + H_-^2)/4 + H_0^2\right\}$	$\frac{1}{5}\left\{(H_+^2 + H_-^2)/4 + H_0^2\right\}$
	7	$\sqrt{2}P_2^1 Re\{Y_1^1\}$	$\frac{3}{\sqrt{10}} H_0 \left(H_+ \cos\delta_+ - H_- \cos\delta_-\right)$	$-\frac{3}{2\sqrt{10}} H_0 \left(H_+ \cos\delta_+ - H_- \cos\delta_-\right)$
	8	$\sqrt{2}P_2^1 Re\{Y_2^1\}$	$-\frac{3}{5\sqrt{2}} H_0 \left(H_+ \cos\delta_+ + H_- \cos\delta_-\right)$	$\frac{3}{10\sqrt{2}} H_0 \left(H_+ \cos\delta_+ + H_- \cos\delta_-\right)$
	9	$\sqrt{2}P_2^2 Re\{Y_2^2\}$	$-\frac{3\sqrt{2}}{5} H_+ H_- \cos(\delta_+ - \delta_-)$	$\frac{3}{5\sqrt{2}} H_+ H_- \cos(\delta_+ - \delta_-)$
T-odd	10	$\sqrt{2}P_2^1 Im\{Y_1^1\}$	$-\eta\frac{3}{\sqrt{10}} H_0 \left(H_+ \sin\delta_+ + H_- \sin\delta_-\right)$	$\eta\frac{3}{2\sqrt{10}} H_0 \left(H_+ \sin\delta_+ + H_- \sin\delta_-\right)$
	11	$\sqrt{2}P_2^1 Im\{Y_2^1\}$	$\eta\frac{3}{5\sqrt{2}} H_0 \left(H_+ \sin\delta_+ - H_- \sin\delta_-\right)$	$-\eta\frac{3}{10\sqrt{2}} H_0 \left(H_+ \sin\delta_+ - H_- \sin\delta_-\right)$
	12	$\sqrt{2}P_2^2 Im\{Y_2^2\}$	$\eta\frac{3\sqrt{2}}{5} H_+ H_- \sin(\delta_+ - \delta_-)$	$-\eta\frac{3}{5\sqrt{2}} H_+ H_- \sin(\delta_+ - \delta_-)$

Table 1.2: The 12 orthonormal angular functions f_i and the corresponding form-factor coefficients Γ_i, as described in Eq. 1.40 for $B \to V\ell\nu_\ell$. Here $Y_m^l \equiv Y_m^l(\theta_\ell, \chi)$ are the spherical harmonics and $P_m^l \equiv \sqrt{2\pi} Y_m^l(\theta_V, 0)$ are related to the Legendre polynomials. $\eta = +1(-1)$ corresponds to a $\bar{B}(B)$ decay. The first nine terms are T-even. The last 3 terms are T-odd contributions from a complex ϵ_R and lead to additional CPV.

1.2.5 T-odd polarization observables (TOPO's)

It is clear from Eq. 1.38 that in the SM, with $\delta_\pm = 0$, the CP-conjugate ($\eta = \pm 1$) expressions are the same and there is no CP-violation. BSM physics can, however, lead to observable CP-violation effects, if $\delta_\pm$ are appreciable. For the light leptons $\ell = e/\mu$, to the first order, the $g_{\{V,A\}}$ terms in the effective Hamiltonian of Eq. 1.15 are the only new sources of CP-violation. This effectively boils down to allowing for a complex phase in ϵ_R, instead of a purely real number. The $\sin\chi$ terms in Eq. 1.38 that flips sign under CP is related to a T-odd triple product, as explained below.

1.2.5.1 Lepton transverse polarization

A long studied observable for new CP-violation terms in semileptonic decays has been the lepton transverse polarization asymmetry [22, 23, 24, 25, 14]. For $P \to X\ell\nu$, where P is a pseudoscalar (B or K meson) and X can be either a vector or pseudoscalar, one defines the scalar triple product

$$P_\ell^\perp = \hat{e}_\ell \cdot (\hat{p}_X \times \hat{p}_\ell) \tag{1.43}$$

which is the lepton polarization transverse to the decay plane containing ℓ and X. Under T-reveral, both spins and momenta get flipped, so that $P_\ell^\perp$ is a T-odd quantity. To measure $P_\ell^\perp$, however, one needs to know the lepton polarization. This is potentially measureable within *BABAR* for hadronic $\tau \to \pi\nu_\tau$ decays [22], for example. For the light leptons, accessing $\hat{e}_\ell$ is difficult and $P_\ell^\perp$ can not be measured directly within *BABAR*.

1.2.5.2 V triple product TOPO's

In a similar vein, consider the following triple product in the ℓ RF:

$$P_V^\perp = \hat{p}_\ell \cdot (\hat{p}_V \times \hat{A}) \sim \sin\theta_\ell \sin\chi, \tag{1.44}$$

where $\hat{A}$ is the analysing direction for the vector meson decay, as tabulated in Table 1.1. The pseudoscalar triple-product is the projection of the lepton momentum on to the V decay plane as defined by $\hat{p}_V \times \hat{A}$, and is T-odd as well (see discussion in Ref. [17], for example). From the structure of Eq. 1.38 there are three CP-odd terms:

$$\sin\theta_\ell \sin\chi \propto P_V^\perp \tag{1.45a}$$

$$\sin\theta_\ell \cos\theta_\ell \sin\chi \propto \hat{p}_\ell \cdot p_V P_V^\perp \tag{1.45b}$$

$$\sin^2\theta_\ell \sin 2\chi \propto \hat{p}_\ell \cdot \hat{p}_{V^\perp} P_V^\perp, \tag{1.45c}$$

where $\hat{p}_{V^\perp}$ is the $\hat{x}$-axis in Figs. 1.6. Therefore, this bears out the fact that the source of the CP-odd terms in Eq. 1.38 is the T-odd triple product $P_V^\perp$.

1.3 BSM scenarios

1.3.1 Left right symmetric models

Two commonly studied BSM scenarios are shown in Figs. 1.7b and c. In the left-right symmetric models (LRSM's) [15, 22, 24, 25, 26], the SM gauge electroweak group $SU(2)_L \times U(1)_Y$ is extended to a $SU(2)_L \times SU(2)_R \times U(1)_{B-L}$, as a result of which there additional heavier gauge bosons Z' and $W_R^{\pm}$. The gauge couplings $g_{L,R}$ belonging to the two SU(2) groups are expected to get a small splitting [27] as well. To get to the SM, the symmetry is broken in two steps. The first breaking occurs at a high scale ($\sim \mathcal{O}(\text{TeV})$), $SU(2)_R \times U(1)_{B-L} \rightarrow U(1)_Y$. The standard electroweak breaking then occurs at a lower scale. After complete symmetry breaking, the $W^{\pm}$ mass eigenstates are related to the gauge eigenstates as

$$W_1 = \cos\zeta\, W_L + e^{i\alpha} \sin\zeta\, W_R \tag{1.46a}$$

$$W_2 = -\sin\zeta\, W_L + e^{i\alpha} \cos\zeta\, W_R \tag{1.46b}$$

where ζ is a real mixing angle and ω is an additional phase that can give rise to CP violation. Note that the RH admixture is given by $\epsilon_R = \tan\zeta\, e^{i\alpha} \dfrac{g_R V_{bq}^R}{g_L V_{bq}^L}$ and in general both the LH/RH couplings and the mixing matrices can be unrelated to each other. Assuming $g_L = g_R$ for the gauge couplings and $V_L = V_R$ for the quark mixing matrices (manifest L-R symmetry), one can obtain limits on W_L-W_R mixing, although, as noted in Ref. [28] (add latest numbers) the .

1.3.2 SUSY models

Fig. 1.7b shows a SUSY scenario with generational mixing for the squarks. The mass matrices of the quarks and squarks are generally expected to be diagonalized by different unitary transformations. The relative rotations in generation space between the up-type and down-type squarks and their corresponding quark partners are denoted by $V^{U_{\{L,R\}}}$ and $V^{D_{\{L,R\}}}$. V^{SKM} is the super CKM matrix associated with the W-squark-squark coupling $W^+ \tilde{u}_{iL}^* \tilde{d}_{jL}$ between the i^{th} and j^{th} generations. The A terms are the soft SUSY breaking terms for the squarks, μ is the two Higgs superfields mixing parameter, $\tan\beta$ is the ratio of the two Higgs vevs, $\alpha_S \approx 0.1$ is the QCD coupling evaluated at the mass scale of the sparticles in the loop. The RH admixture is then given by [29]

$$\epsilon_R = -\frac{\alpha_S}{36\pi} \frac{m_t(A_t - \mu\cot\beta)}{m_{\tilde{g}}^2} \frac{m_b(A_b - \mu\tan\beta)}{m_{\tilde{g}}^2} \frac{V_{33}^{\text{SKM}} V_{3i}^{U_R *} V_{33}^{D_R}}{V_{bq}} I_0\left(\frac{m_{\tilde{t}}^2}{m_{\tilde{g}}^2}, \frac{m_{\tilde{b}}^2}{m_{\tilde{g}}^2}\right) \tag{1.47}$$

where $i = 1(2)$ for the final quark being $q = u(c)$ and the integral function I_0 is

$$I_0(a,b) = \int_0^1 dz_1 \int_0^{1-z_1} dz_2 \frac{24 z_1 z_2}{(a z_1 + b z_2 + (1 - z_1 - z_2))^2} \tag{1.48}$$

(add latest numbers)

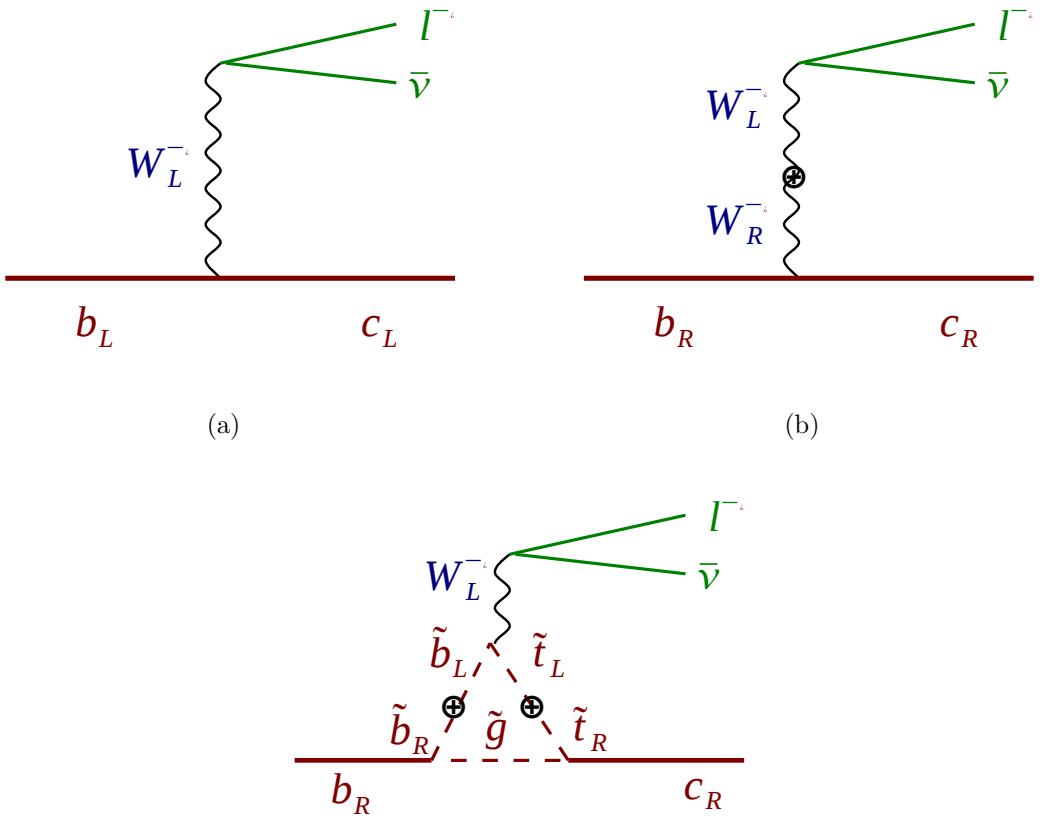

Figure 1.7: The process $b \to c\ell^-\bar{\nu}$ in (a) for the SM, the W boson coupling is strictly LH. In the (b) LRSM model with an W_R and (c) gluino penguin in SUSY, an effective RH coupling can occur.

1.4 Summary

In this chapter we desribed the motivation and underlying theoretical formulation of exclusive B semi-leptonic decays. In particular we provided a detailed description of the expressions of the angular distributions incorporating NP terms in the form of a RH admixture in the quark-sector weak charged current.

Chapter 2

Data Analysis

2.1 Hadronic B tagging

In the process $e^+e^- \to \Upsilon(4S) \to B_{\rm sig}B_{\rm tag}$, to extract a clean sample of $B_{\rm sig}$, we employ an exclusive, fully-reconstructed tagging of the "other" B, denoted as $B_{\rm tag}$ or $B_{\rm reco}$. The $B_{\rm tag}$ reconstruction relies on two variables that are almost uncorrelated:

$$\Delta E = E_{\rm tag} - \sqrt{s}/2, \tag{2.1}$$

$$m_{\rm ES} = \sqrt{s/4 - |\vec{p}_{\rm tag}|^2}, \tag{2.2}$$

where $\sqrt{s}$ is the center-of-mass (c.m.) energy and $E_{\rm tag}$ is the energy of the tagged B. In the ideal case, $\Delta E = 0$ and the energy-substituted mass $m_{\rm ES} = m_B$.

The $B_{\rm tag}$ decays to a charm-meson "seed" $S \in \{D^{(*)0}, D^{(*)+}, D_s^{(*)+}, J/\psi\}$ plus a system, Y, of charmless light hadrons, with at most five charged and two neutral particles. That is, $Y = n_1\pi^\pm + n_2K^\pm + n_3K_S^0 + n_4\pi^0$, with $n_1{+}n_2 \leq 5$, $n_2 < 2$, $n_4 \leq 2$, $n_1{+}n_2{+}n_3{+}n_4 \leq 5$ and the total charge of Y is ± 1. This is shown in Fig. 2.1 for the $B \to \rho\ell\nu$ channel. The original `BSemiExcl` skim [30] included only the $D^{(*)}$ seeds in around 650 decay modes. It included some loose cuts on ΔE and $m_{\rm ES}$. After this a purity (fraction of correctly reconstructed B's for $m_{\rm ES} > 5.27$ GeV for the given mode) cut as placed to remove the "dirty" modes. This purity cut resulted in around 300 final $B_{\rm tag}$ modes.

In this analysis we use the latest `BSemiExclAdd` skim [31, 32], which added new seeds for $D_s^{(*)+}$ and J/ψ over those in `BSemiExcl` and removed the purity cut to increase the skim signal reconstruction efficiency. The total number of modes in the `BSemiExclAdd` skim is 2968. At this point, the only cuts in the skim are $|\Delta E| < 0.2$ GeV and 5.18 GeV $\leq m_{\rm ES} \leq$ 5.30 GeV on the tagged side.

We note that the method of full hadronic reconstruction has been used to study semileptonic D decays [33, 34] in e^+e^- charm machines as well. In a completely analogous fashion, CLEO-c and BESIII look at threshold production of the $\psi(3770)$ that almost exclusively decays to

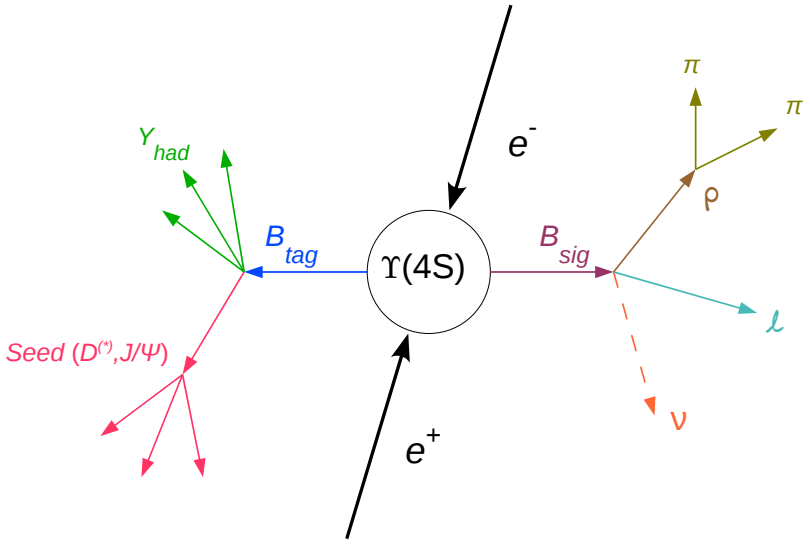

Figure 2.1: The hadronic B-reconstruction method – the $B_{\rm tag}$ is fully reconstructed and all particles in the event are detected, excepting the outgoing ν which is reconstructed as the total missing 4-momenta.

a $D\bar{D}$ pair. The tag-side D is fully hadronically reconstructed, giving access to $D \to X\ell\nu$ SL decays.

2.2 Data and Monte Carlo Samples

We use release 24.3.6 (analysis-51) and analyse the full *BABAR* dataset (Runs 1-6) with 426.1 fb^{-1} of integrated luminosity at the 10.58 GeV on-peak $\Upsilon(4S)$ production corresponding to about 471 million $\Upsilon(4S) \to B\bar{B}$ decays. We use R24a samples for the data. In addition to the on-peak data, off-peak e^+e^- data collected 40 MeV below the $\Upsilon(4S)$ mass are sometimes used study the continuum ($e^+e^- \to q\bar{q}$) background. In this analysis we do not use the off-peak data sample, as will be explained in Sec. 2.2.2.

For Monte Carlo (MC), in addition to R24c ($\times$3 the data luminosity), for $B\bar{B}$ and $c\bar{c}$, we use R26a ($\times$7 data luminosity) samples. In all we have MC simulation of generic $B\bar{B}$ decays equivalent to about ten times the recorded data, and continuum simulation of about twice the data luminosity. The generic $B\bar{B}$ MC is thrown with the HQET FF parameterizations for the $D^{(*)}$'s and ISWG2 FF's for the charmless channels. We also use signal MC where $B_{\rm sig}$ is thrown with the `FLATQ2` generator (flat in all four kinematic variables $\phi \in \{q^2, \chi, \cos\theta_\ell, \cos\theta_V\}$) and $B_{\rm tag}$ is allowed to decay in a generic fashion.

Sample Type	Skim Version	$\mathcal{L}$ (/fb)	$N(\times 10^6)$
Data	BSemiExclAdd-RunX-OnPeak-R24c-v07	424.25	-
Generic B^+B^- MC	SP-1235-BSemiExclAdd-RunX-R24c-v08	-	707.282
Generic B^+B^- MC	SP-1235-BSemiExclAdd-RunX-R26a-v04	-	1624.666
Generic $B^0\bar{B}^0$ MC	SP-1237-BSemiExclAdd-RunX-R24c-v08	-	716.219
Generic $B^0\bar{B}^0$ MC	SP-1237-BSemiExclAdd-RunX-R26a-v04	-	1649.784
Continuum $c\bar{c}$ MC	SP-1005-BSemiExclAdd-RunX-R26a-v04	-	1127.36
Continuum $c\bar{c}$ MC	SP-1005-BSemiExclAdd-RunX-R24c-v08	-	4330.141
Continuum uds MC	SP-998-BSemiExclAdd-RunX-R24c-v08	-	2190.254
`FLATQ2` ρ^0 MC	SP-4763-AllEventsSkim-R24f	-	8.285

Table 2.1: The data and Monte Carlo samples used in this analysis. RunX denotes Runs 1-6 and all samples are on-peak.

2.2.1 Reconstruction of the $\Upsilon(4S)$ using `SimpleComposition`

The $\Upsilon(4S)$ is reconstructed out of $B_{\rm sig}$ and $B_{\rm tag}$ using the package `SimpleComposition`. $B_{\rm sig}$ is reconstructed as $B_{\rm sig} \to X\ell(\nu)$, where the neutrino is the only undetected particle in the event. Therefore,

$$\mathrm{mm}^2 \equiv p^2_{\rm miss} \equiv p^2_\nu = (p_{e^+e^-} - p_{B_{\rm tag}} - p_X - p_\ell)^2. \tag{2.3}$$

For correctly reconstructed signal events, the missing mass squared $\mathrm{mm}^2 \equiv p^2_\nu = 0$, corresponding to a massless missing neutrino. Thus, we use the discriminating variable for signal selection as

$$U = E_{\rm miss} - |\vec{p}_{\rm miss}| = E_\nu - |\vec{p}_\nu| \tag{2.4}$$

The resolution in the U variable is less dependent on the value of the neutrino energy than mm^2, and was also employed in previous CLEO $D \to \rho\ell\nu$ analysis [33], and other *BABAR* analyses as well. Fig. 2.2 we plot the signal resolutions in mm^2, U and $U/2E^*_\nu$ against the reconstructed E^*_ν (starred quantities are computed in the B RF), where the dependence on the lepton energy is clearly borne out.

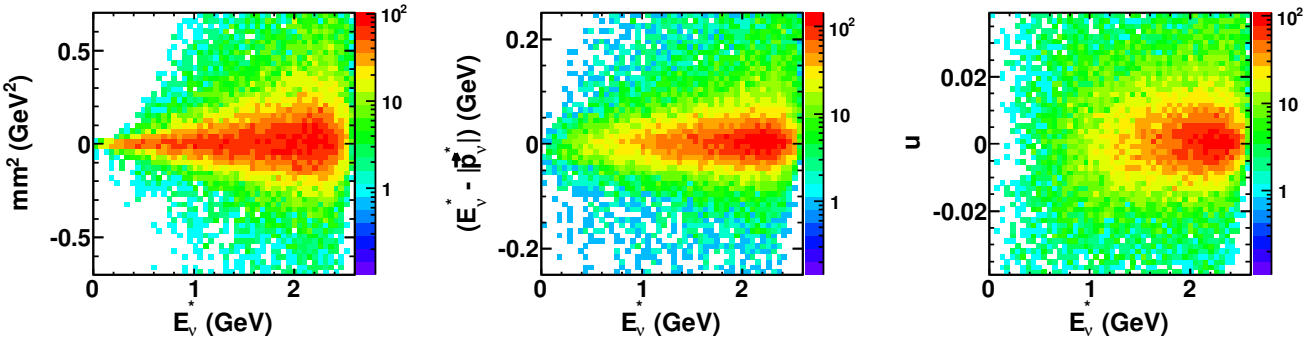

Figure 2.2: Plots showing the dependence of the resolutions in the variables mm^2, U and $U/2E^*_\nu$ on E^*_ν from the signal MC.

The $X \equiv \rho^0$ candidates are reconstructed via $\rho^0 \to \pi^+\pi^-$.

2.2.2 Additional cuts during re-skim

The `BSemiExclAdd` skim was designed to be very loose and therfore tends to be bulky. To reduce background, after the $\Upsilon(4S)$ candidate has been reconstructed, the `BSemiExclAdd` skim is re-skimmed with the following cuts:

1. $|\Delta E| < 75$ MeV
2. $m_{\rm ES} > 5.265$ GeV
3. $|U| < 0.5$ GeV

None of these cuts are supposed to have any effect on correct signal events, but merely serve to reduce the disk-space requirement. Note that becuase of the tight $m_{\rm ES}$ signal window, we trim out most of the off-peak continuum events which have $m_{\rm ES} \leq 5.29$ GeV. Conventionally, other *BABAR* analyses shift the off-peak data $m_{\rm ES}$ by 20 MeV prior to event selection cuts. While 20 MeV is small compared to m_B itself, it is comparable to our final $m_{\rm ES}$ signal-window width ($m_{\rm ES} \in [5.27, 5.29)$ GeV). Additionally, we do not attempt to fix the normalizations of the continuum component during our final fits. Hence, we do not make use of the off-peak data sample. The other cut applied during reskim was that events more than 18 charged tracks or 25 neutral clusters on the tag-side were rejected.

2.3 PID selection

For the most part, we follow the setup in the $B \to D^{(*)}\tau\nu$ analysis [31] and simply added the charmless modes in `SimpleComposition`. The PID selectors are also mostly common. The individual γ, $\pi^\pm$, $K^\pm$, K^0_S and π^0 candidates are taken, with some modications, from standard *BABAR* PID selectors, namely, `CalorNeutral`, `piKM`, `KKM`, `KsDefault`, and `pi0AllDefault` lists, respectively. Charged tracks ($\pi^\pm$, $K^\pm$ candidates) must have momentum less than 4 GeV, while reconstructed π^0 and K^0_S trajectories must have momentum less than 3 and 4 GeV, respectively. Photon candidates are required to have a minimum raw energy deposition of 50 MeV in the EMC. The lepton candidates are also taken from standard *BABAR* PID selectors: electrons from `eKM` and muons from `muBDT`. The tightness level for all charged particle PID selectors are chosen to be at least "`Tight`".The polar angle of the lepton candidates are required to lie in the range $\theta \in (0.4, 2.6)$. This avoids the poor momentum resolution of tracks measured close to the edges of the barrel due to excess material and the drift chamber acceptance. Electrons with momentum less than 300 MeV are rejected to ensure a good measurement of their energy in the EMC and reject low momentum background, such as from photon conversions. We apply a standard *BABAR* bremsstrahlung algorithm [35] to correct for energy loss in $e^\pm \to e^\pm\gamma$ with relative angle between the brem photon and the electron to satisfy $\theta < 50$ mrad and $\phi < 200$ mrad. The leptons are also required to pass the `GoodTracksLoose` selector.

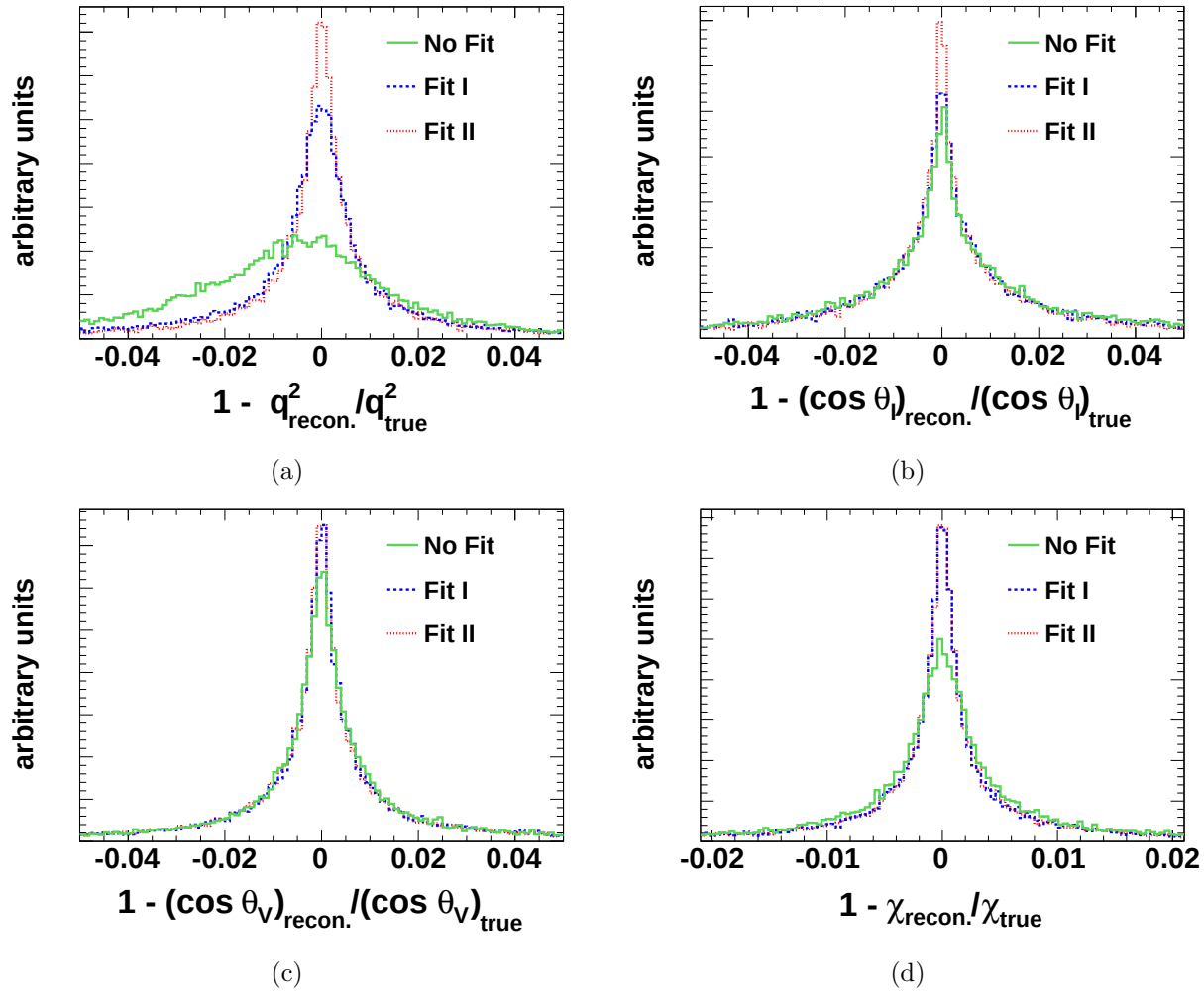

Figure 2.3: The effect of the vertex-fitting on the reconstruction of the variable (a) q^2 (b) $\cos\theta_\ell$ (c) $\cos\theta_V$ and (d) χ for $B \to \rho^0 \ell\nu$ signal MC. The histograms are scaled to unit area to emphasize the change in the shape.

2.4 Vertex and Kinematic Fitting

After a $B_{\rm tag}X\rho\ell$ combination has been selected, events with additional tracks not used in the event reconstruction are rejected. The resulting $\Upsilon(4S)$ candidate is refitted to improve the resolutions using the `TreeFitter` algorithm [36]. The almost-full reconstruction of the entire event allow for several constraints during this fitting procedure:

1. since the ρ has a large width, we do not mass-constrain $M(\pi\pi)$
2. the ρ meson vertex is constrained to the beam-spot, while allowing for the B flight
3. both $B_{\rm sig}$ and $B_{\rm tag}$ are mass-constrained
4. the $\Upsilon(4S)$ candidate vertex is constrained to the beam-spot

5. an optional additional mass constraint on the missing ν.

Constraints 1-4 were applied nominally and we refer this to as Fit I. Candidate events where Fit I either failed or did not converge were rejected at this stage.

Each $\Upsilon(4S)$ candidate was separately fitted once with and once without the last constraint and both fitted decay trees were saved in the data stream. The fit incorporating constraint 5 will be referred to as Fit II. The resolution of the reconstructed kinematic variables are improved by the vertex fits. Fig. 2.3 shows the relative difference between the reconstructed and generated (true) kinematic variables. For the most part, the relative difference (smear factor) is at the percent level, thanks to the tagging.

2.5 Study of $B \to \rho^0 \ell\nu$ using Monte Carlo

In the following sections we describe our analysis cuts. Unless otherwise mentioned, each MC component comprising continuum, signal and non-signal $B\overline{B}$ MC is weighted to the corresponding expected contribution in the data, based on the individual cross-section and/or BF. For a charmless channel like $B \to \rho^0 \ell\nu$, it is essential to treat the electron and muon modes separately, because of significant pion contamination and mis-identified as a muon. The muon-misID is most prominent in the charmless continuum. To trim out the continuum, we look at the shape-variable $\Delta\theta_T$, the angle between the thrust axis of the reconstructed $B_{\rm tag}$ and that of the rest-of-the-event (ROE). Typically the electron channels have lower continuum background.

The other important variable that helps in background removal is $E_{\rm ex}$, the sum of the energies of the extra good photons that were not used in the event reconstruction. A "good" photon is defined to have deposited at least 50 MeV as a cluster in the EMC.

After the application of all analysis cuts, for each event, we choose a single $\Upsilon(4S)$ candidate out of all possible combinations. We consider two options for making this `BestUpsilon` choice – the candidate with the highest vertex fit probability, or the candidate with the least $E_{\rm ex}$. As it turns out, given the already clean sample of events from the $B_{\rm tag}$ reconstruction, the difference between the two choices is minimal. After all our final cuts, and under the ρ signal peak, we find the average number of `BestUpsilon` candidates to be ~ 2, with a peak at 1 – this reduced multiplicity is due to the tight constraints placed both on the signal and tag side, that help reduce the ambiguities in the choice of `BestUpsilon`.

We also note here that while treating the MC samples, we specifically exclude contributions from the inclusive $B \to X_u \ell\nu$ component in the generic $B\bar{B}$ MC samples. The inclusive component consists of non-resonant X_u hadrons with invariant mass greater than $2m_\pi$.

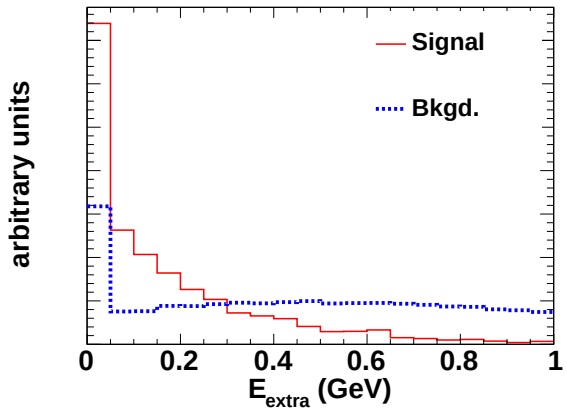

Figure 2.4: $E_{\rm ex}$ distributions for the signal and background components for $B \to \rho^0 \ell\nu$. Note that the selection contains the full U and $M(\pi\pi)$ range.

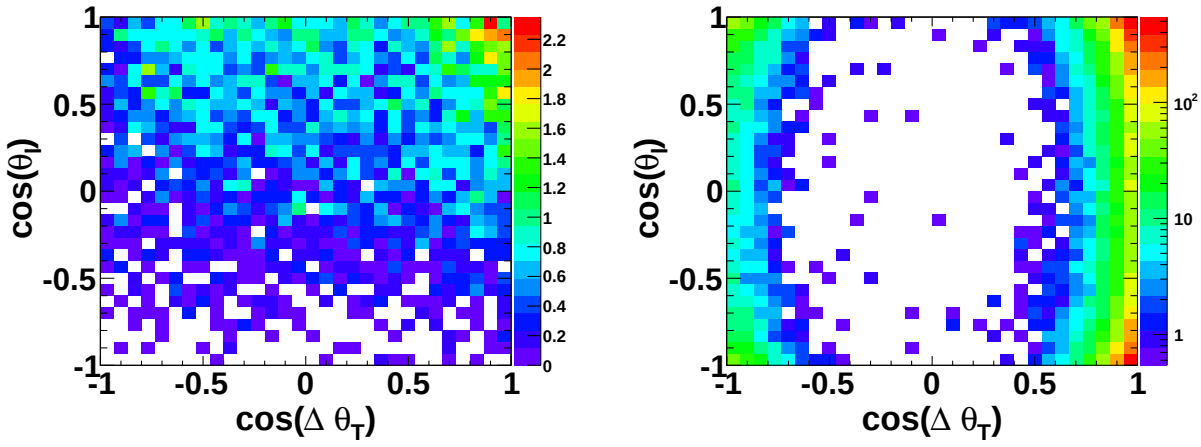

(a) (b)

Figure 2.5: $\cos\theta_\ell$ vs $\cos(\Delta\theta_T)$ plots for (a) signal MC (b) continuum.

2.6 The $E_{\rm ex}$ cut

Fig. 2.4 shows the $E_{\rm ex}$ distributions for the signal and background components. The histograms have been normalized to unit area to emphasize the shape and include the following nominal cuts: $|\cos(\Delta\theta_T)| < 0.85$ and probability from Fit I $\geq 10^{-6}$, while retaining the side-band regions in both U and $M(\pi\pi)$. We choose a very loose $E_{\rm ex} < 0.6$ GeV cut for further analysis. This results in a signal loss of $\sim 5\%$, but suppresses background by $\sim 39\%$ in the signal peak region.

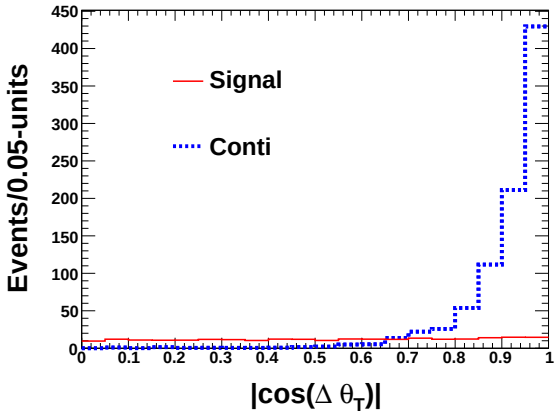

Figure 2.6: $|\cos(\Delta\theta_T)|$ distributions for the continuum and signal components.

2.7 The $|\cos(\Delta\theta_T)|$ cut

After the tag side signal window (in $m_{\rm ES}$ and ΔE) has been chosen, most of the kinematic variables (that is, not, for example $E_{\rm ex}$) have some degree of correlation between them, given that the kinematics is so tightly constrained. Fig. 2.5a shows the scatter distribution of $\cos\theta_\ell$ against $\cos(\Delta\theta_T)$ for the signal MC (incorporating the full 4-d differential rate). The $(V-A)$ nature of the left-handed weak current in the SM results in the $\theta_\ell \to +1$ behavior. However, this also lead to an enhanced jettiness of the event, resulting in the correlation with the thrust angle. Fig. 2.5b shows the same for the continuum where the jettiness ($|\cos(\Delta\theta_T)| \to 1$ is again seen to be correlated with $\cos\theta_\ell$. A cut on $|\cos(\Delta\theta_T)|$ is therefore best avoidable, so that the $\cos\theta_\ell$ distribution for the signal is not affected. For the electron channel, we place a $|\cos(\Delta\theta_T)| < 0.85$ cut, while for the muon channel, that has a larger continuum leakage, we require $|\cos(\Delta\theta_T)| < 0.8$. At $q^2 < 2$ GeV^2, we require tighter cuts at 0.75 and 0.6, for e and μ, respectively. Fig. 2.6 shows the $|\cos(\Delta\theta_T)|$ distributions of the signal and continuum components. The signal is flat, while the continuum is jetty and forward-peaked.

2.8 The $|\vec{p}^{\,*}_{\rm miss}|$ cut

Fig. 2.7 shows the $|\vec{p}^{\,*}_{\rm miss}|$ for the signal and background, in the signal region: $|U| < 0.1$ GeV, $|\cos(\Delta\theta_T)| < 0.85$, $E_{\rm ex} < 0.6$, $M(\pi\pi) \in [0.6, 0.95]$ GeV and probability from Fit II $> 10^{-6}$. The background population near $|\vec{p}^{\,*}_{\rm miss}|$ corresponds to no missing particles (from combinatorial $B\overline{B}$ and continuum). We place a loose cut at $|\vec{p}^{\,*}_{\rm miss}| > 0.3$ GeV.

2.9 Final $B \to \rho^0\ell\nu$ selection cuts

We require the reconstructed ρ mass to be in the range $M(\pi\pi) \in [0.5, 1.1]$ GeV and $|U| < 0.4$ GeV. If one incorporates the effect of a $\pi \leftrightarrow \mu$ mis-ID, three light pions are being

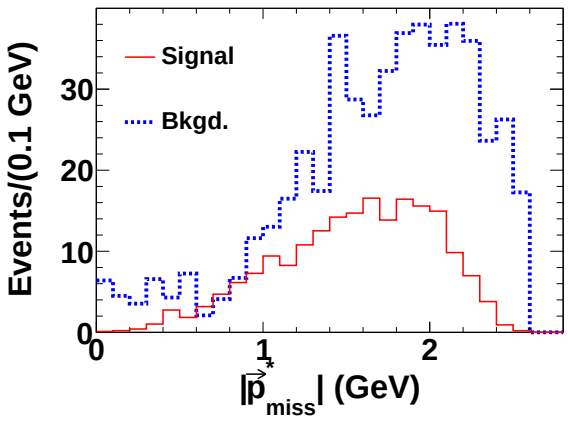

Figure 2.7: $|\vec{p}^{\,*}_{\rm miss}|$ distributions for the signal and background components for $B \to \rho^0 \ell \nu$.

produced on the signal side with little kinematic constraints (since both X and ν are not mass-constrained here). This causes a rather large leakage from the non-$c\bar{c}$ continuum that hadronizes into light hadrons to produce, for example a $\rho\pi$ pair on the signal side, that is reconstructed as $\rho\mu(\nu)$. We also include a loose purity cut of > 0.05. Our final cuts for the two leptons are:

- electron: $E_{\rm ex} < 0.6$ GeV, $|\cos(\Delta\theta_T)| \leq 0.85$, probability from Fit I $\geq 10^{-6}$, $B_{\rm tag}$ mode purity > 0.05, $|\vec{p}^{\,*}_{\rm miss}| > 0.3$ GeV
- muon: $E_{\rm ex} < 0.6$ GeV, $|\cos(\Delta\theta_T)| \leq 0.8$, probability from Fit I $\geq 10^{-6}$, $B_{\rm tag}$ mode purity > 0.05, $|\vec{p}^{\,*}_{\rm miss}| > 0.3$ GeV
- electron/muon: $m_{\rm ES} \in [5.27, 5.29]$ GeV, $|\Delta E| < 72$ MeV

Since there are no γ's involved in the final state and the X mass-window is so wide, we choose the candidate with the highest χ^2 probability from Fit I as the `BestUpsilon`. Note that due to the stringent BReco signal window cuts on $m_{\rm ES}$ and ΔE, these cease to be variables that can be utilized for signal-background separation, in this analysis. In particular, we do not look at $m_{\rm ES}$ side-bands for a control sample, or for our background subtraction.

2.10 U distributions after all cuts

The U distributions after all cuts have been placed and $M(\pi\pi) \in [0.6, 0.95]$ GeV are shown in Fig. 2.8a and Fig. 2.8b for the e and μ channels, respectively. The hashed histograms represent the signal, the solid blue histograms represent the continuum background, and the dashed red histogram represents the $B\overline{B}$ combinatoric background. There are several features of note here. First, the signal distribution for the e mode shows a significantly longer tail than that for the μ mode, due to higher bremsstrahlung. Second, the background distributions are smooth under the signal, which is a very important factor to facilitate

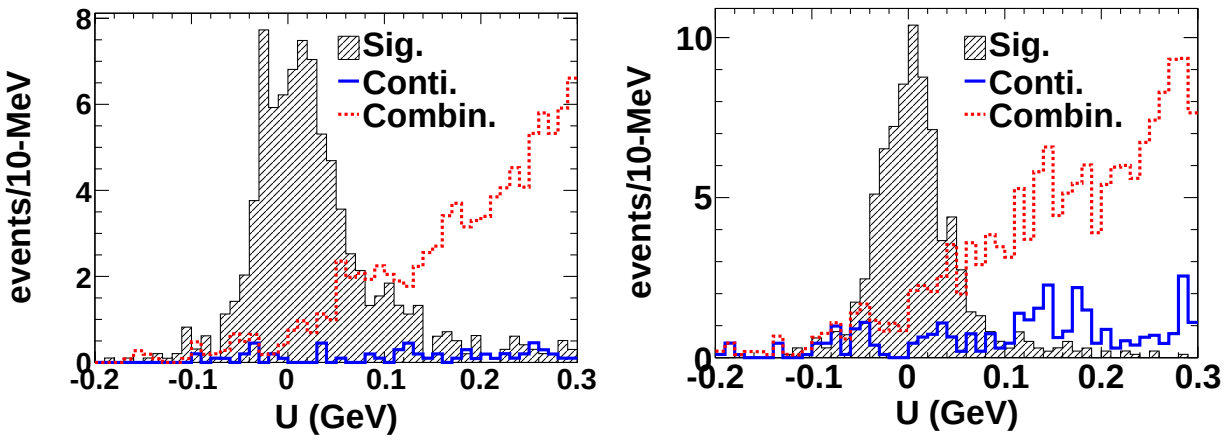

(a) (b)

Figure 2.8: $B \to \rho^0 \ell\nu$ signal and background lineshapes obtained from the MC for the (a) electron and (b) muon channel and $M(\pi\pi) \in [0.6, 0.95]$ GeV.

a data-driven signal-background-separation scheme. The thrust cut in Fig. 2.8b is tighter than in Fig. 2.8b, yet the continuum levels are comparable, pointing to the higher continuum leakage for the μ mode. From Fig. 2.5b, to completely remove the continuum, a thrust cut of the order of $|\cos(\Delta\theta_T)| < 0.55$ is needed. However, from Fig. 2.5a, such a tight cut would severely distort the $\cos\theta_\ell$ distribution in the signal. We choose to retain as loose a $\cos(\Delta\theta_T)$ cut as possible without leaking in too much background.

The predicted signal yields at this stage, based on the MC are $\mathcal{O}(84)$ and $\mathcal{O}(80)$ for the electron and muon channels, respectively.

2.11 True $\rho^0 \to \pi^+\pi^-$ from background events

In Fig. 2.9 we plot the variable U against the reconstructed ρ mass for signal and background in the MC separately for e/μ samples. Clearly, there are background events where the reconstructed ρ comes from a true $\rho^0 \to \pi^+\pi^-$ decay. Since both the signal and the background have structures in the $M(\pi\pi)$ variable, we employ 2-D fits in U and $M(\pi\pi)$ for our signal-background separation procedure. We note here that initial trial 1-D signal-background fits (in U) gave poor results when projected in $M(\pi\pi)$. The ρ peak and the sidebands have different S/B, and they can not be lumped together. The correct approach here would have been to sub-divide the dataset in $M(\pi\pi)$ bins and then perform 1-D fits in U. However, we do not have enough statistics to allow for that. Therefore, we were forced to account for the $M(\pi\pi)$ dependence by directly including it as one of the fitted variables.

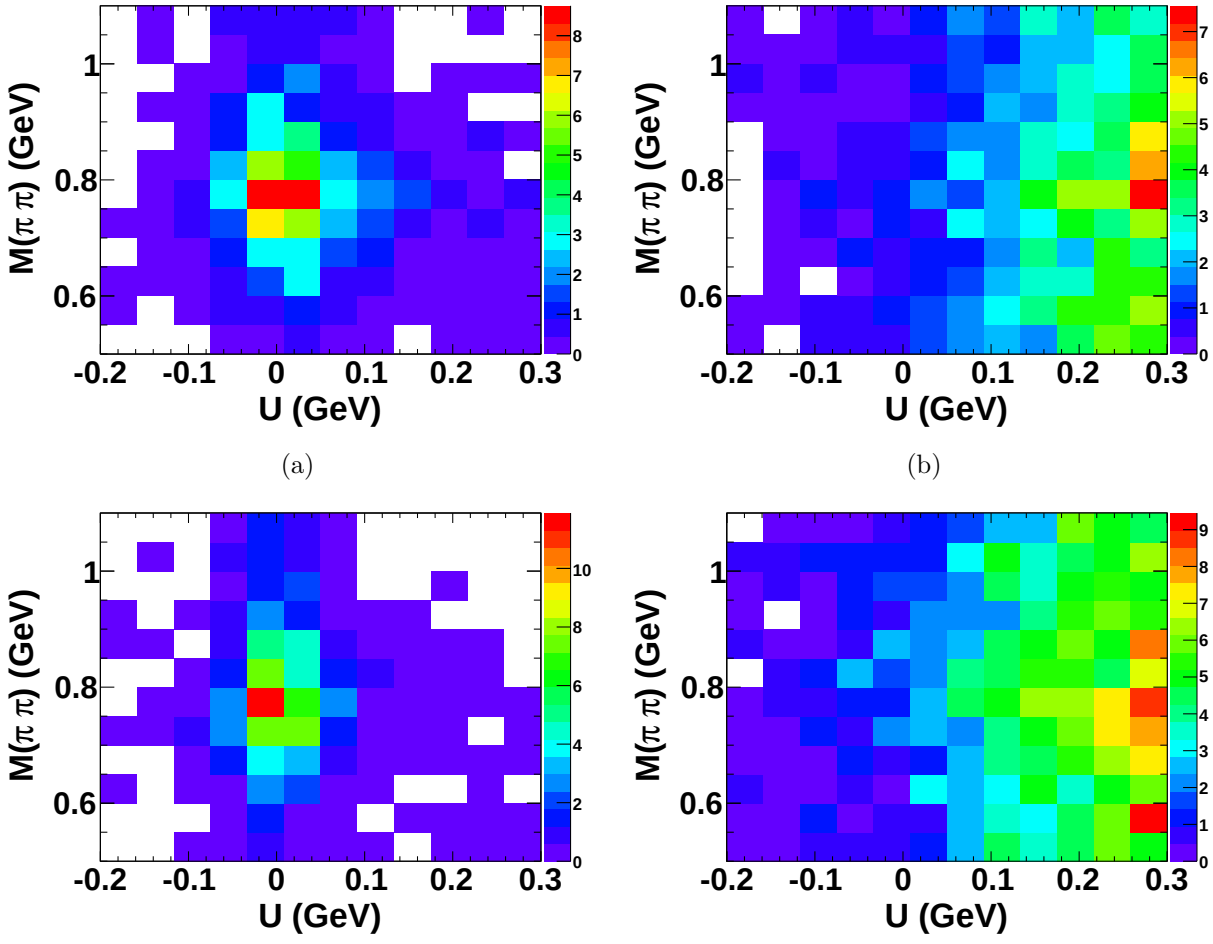

(a) (b) (c) (d)

Figure 2.9: $M(\pi\pi)$ vs. U plotted for (a) e signal (b) e background (c) μ signal and (d) μ background.

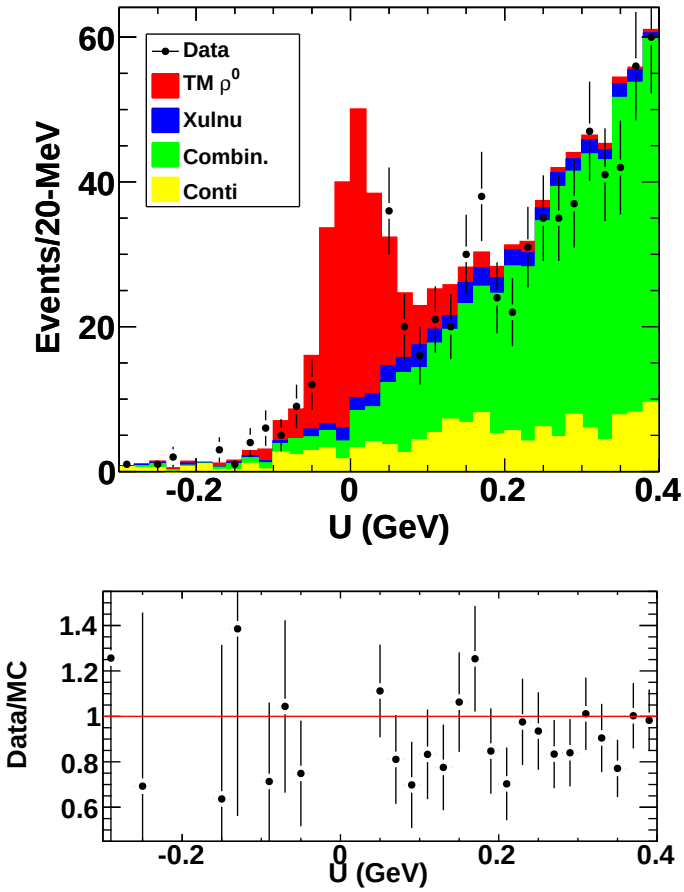

Figure 2.10: Data/MC comparison after all cuts and $M(\pi\pi) \in [0.6, 0.95]$ GeV. Electron and muon samples combined.

2.12 Data/MC comparisons

The present analysis is relatively less dependent on the MC than other comparable analyses. We rely on the MC primarily to understand any non-uniform peaking structures in the U variable from background events, as was shown if any. We parameterize the smooth background primarily as the tail of a Gaussian (with some phase-space dependent caveats). The initial values for both the signal and background lineshapes are obtained from the MC as "reasonable start guesses", but are allowed to vary during the signal-background-separation fit. Fig. 2.10 shows the stacked histograms for the MC and and a comparison with the Data in the upper pad; the lower pad shows the Data/MC ratio. The continuum includes both uds and $c\bar{c}$. The $X_u\ell\nu$ comprises cross-feed from other exclusive charmless decays, excluding $\pi^+\pi^-$ states. The combinatoric component comprises mostly $X_c\ell\nu$, but also hadronic $B\overline{B}$ decays. We emphasize that the MC has *not* been fitted to the Data – the MC components have been taken "as is" in the analysis-51 `DECAY.DEC` file with some updates as was used in the Ref. [31]. So the plots in this section should be seen only as "in the correct ballpark" sense. Each component in the MC has been normalized to the Data luminosity.

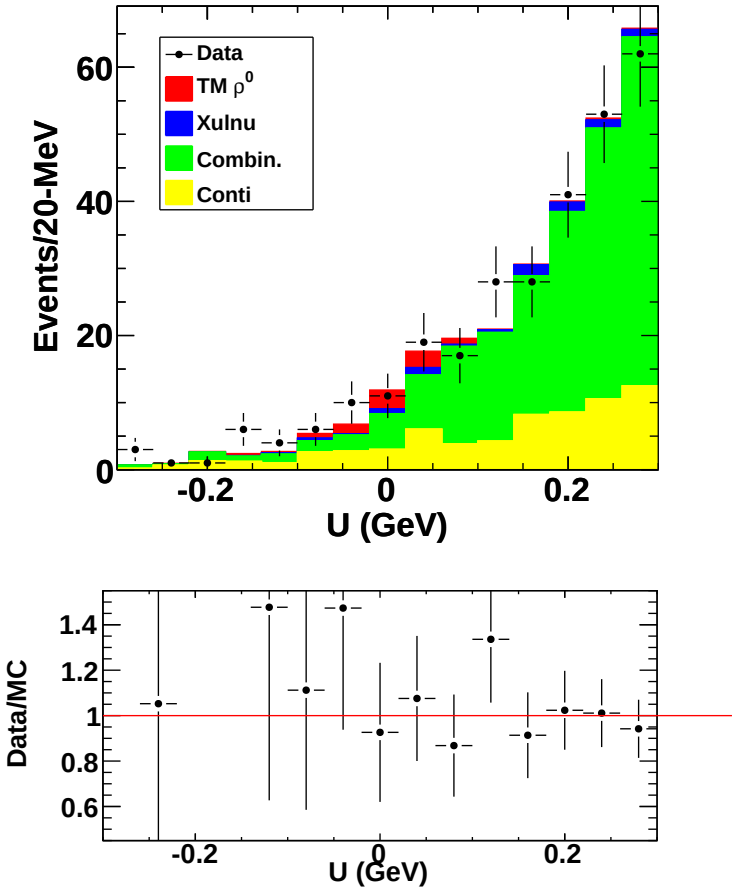

Figure 2.11: Data/MC comparison after all cuts and $|M(\pi\pi) - 0.77| < 0.15$ GeV in the control region $E_{\rm ex} > 0.6$ GeV. Electron and muon samples combined.

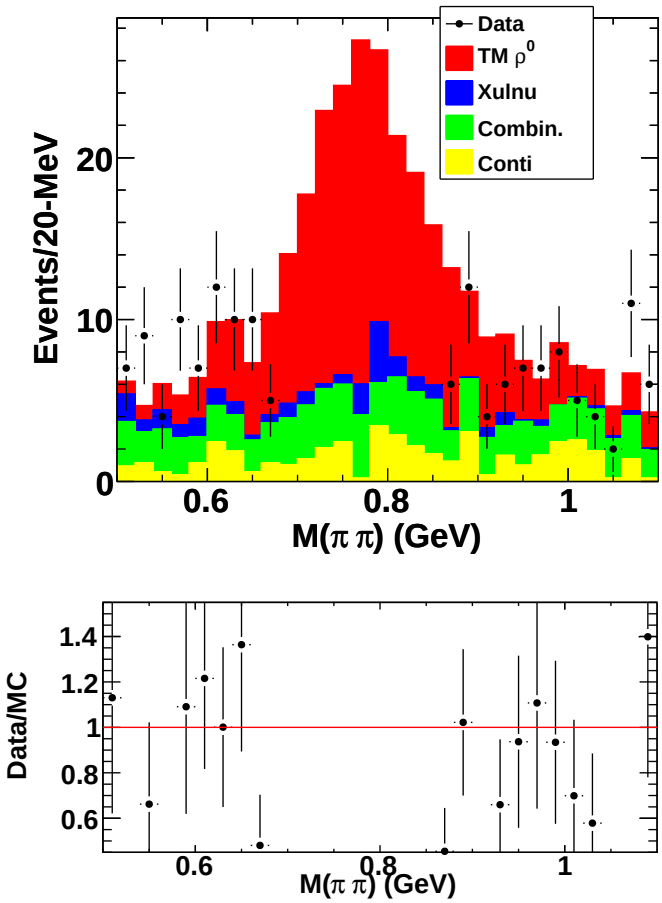

Figure 2.12: Data/MC comparison after all cuts and $|U| < 0.1$ GeV. Electron and muon samples combined.

Fig. 2.11 shows the U Data/MC comparison in a $E_{\rm ex} > 0.6$ GeV control region (our final cut is $E_{\rm ex} < 0.6$ GeV), with a $|M(\pi\pi) - 0.77| < 0.15$ GeV cut (plus other nominal cuts).

Fig. 2.12 shows the Data/MC comparisons in $M(\pi\pi)$ with a $|U| < 0.1$ GeV cut. Note that the continuum peaks in $M(\pi\pi)$ (but not in U from Fig. 2.10), from true $\rho \to \pi\pi$ events. Fig. 2.12 shows the Data/MC comparison in $\vec{p}^{\,*}_{\rm miss}$ off-peak in U but on-peak in $M(\pi\pi)$. Figs. 2.14 and 2.15 shows the same in p^*_ℓ and $E_{\rm ex}$, respectively. Note that in the very first bin in Fig. 2.15, there is a prominent mismatch between Data/MC. This is a well known problem in both *BABAR* and Belle – the variable $E_{\rm ex}$ represents the amount of leftover neutral clusters background and simulating this perfectly is challenging. Note that this problem is independent of the physics under study – for instance, Fig. 2.15 is off-peak for this analysis. However, our analysis is very weakly dependent on the $E_{\rm ex}$ simulation.

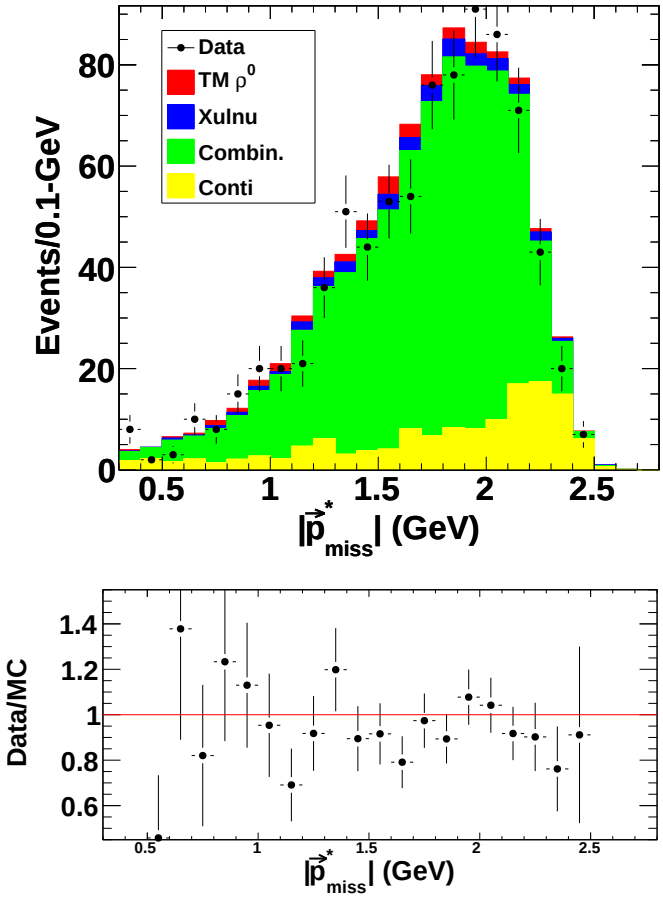

Figure 2.13: Data/MC comparison in the variable $\vec{p}_{\rm miss}$ after all cuts and $|U| > 0.1$ GeV and $|M(\pi\pi) - 0.77| < 0.15$ GeV . Electron and muon samples combined.

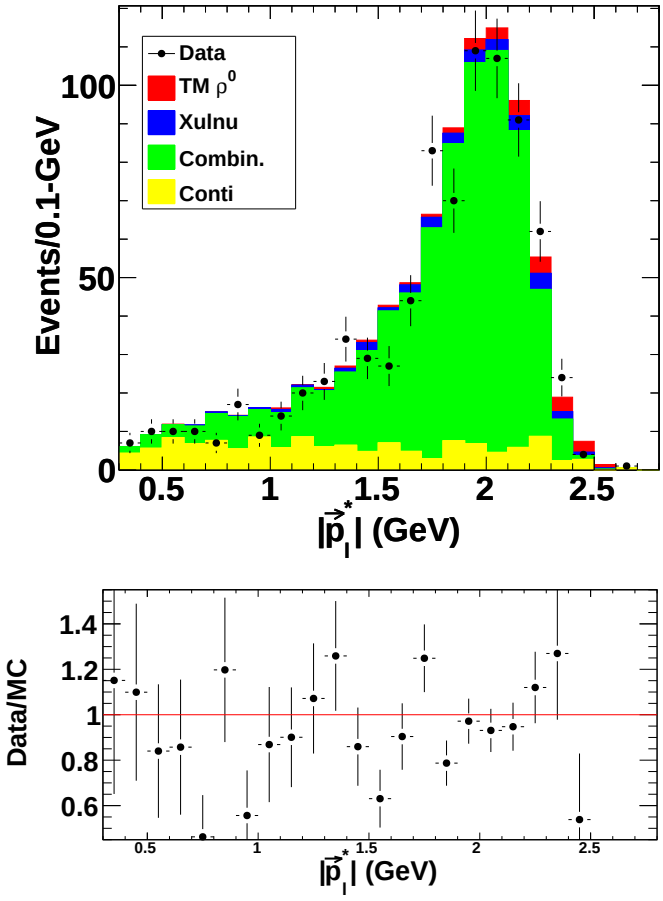

Figure 2.14: Data/MC comparison in the variable p_ℓ^* after all cuts and $|U| > 0.1$ GeV and $|M(\pi\pi) - 0.77| < 0.15$ GeV . Electron and muon samples combined.

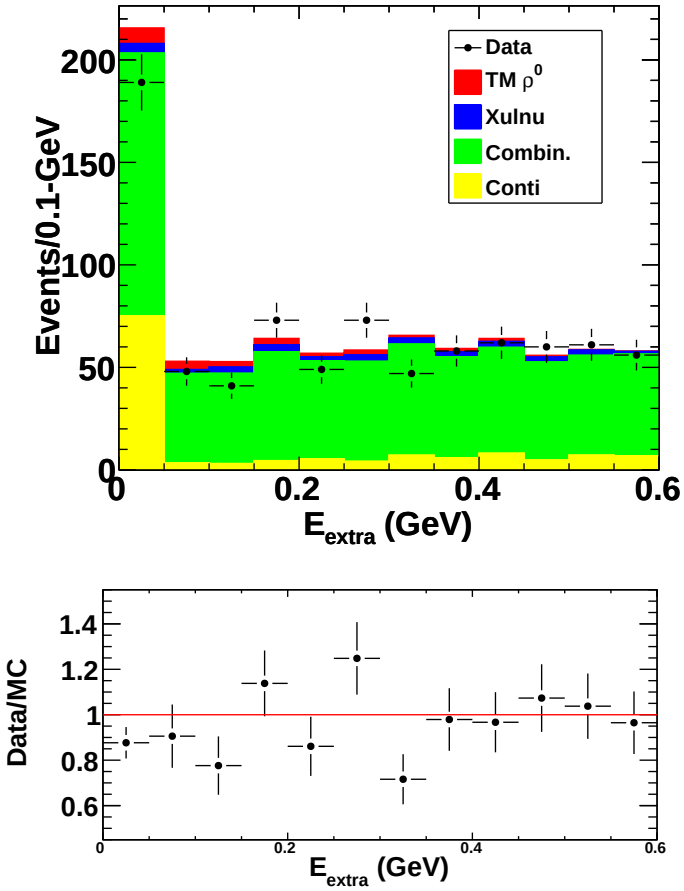

Figure 2.15: Data/MC comparison in the variable $E_{\rm ex}$ after all cuts and $|U| > 0.1$ GeV and $|M(\pi\pi) - 0.77| < 0.15$ GeV . Electron and muon samples combined.

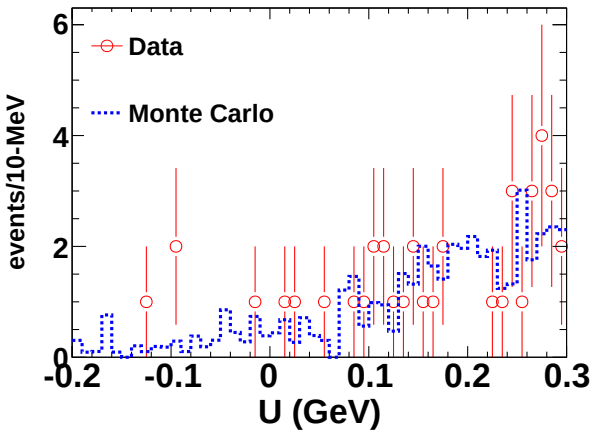

Figure 2.16: $B \to \pi^0\pi^0\ell\nu$ channel comparison between Data and MC.

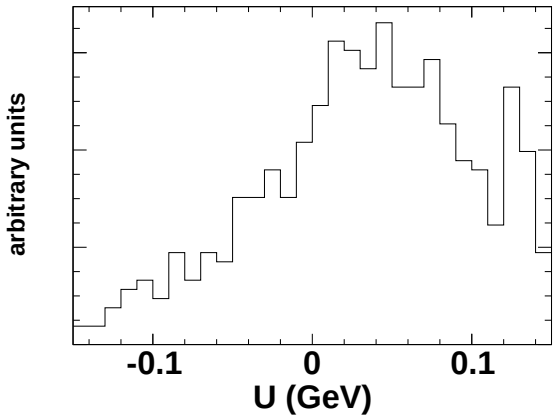

Figure 2.17: The signal lineshape in U plotted for phase-space $B \to \pi^0\pi^0\ell\nu$ MC. Substantial FSR results in the poor resolution.

2.13 $B \to \pi^0\pi^0\ell\nu$

The motivation for analyzing this channel is to look for potential a non-P-wave $\pi\pi$ under the ρ mass peak. Since C-parity conservation forbids a $\rho^0 \to \pi^0\pi^0$ transition, any non-negligible $\pi^0\pi^0$ would therefore point toward an S-wave component under the ρ. We require $M(\pi^0\pi^0) \in [0.65, 0.9]$ GeV, $E_{\rm ex} < 0.6$ GeV, $|\cos(\Delta\theta_T)| \leq 0.85$ and probability from Fit I $\geq 10^{-4}$ and compare the Data with the MC (without any $\pi^0\pi^0$ component) in Fig. 2.16. In Fig. 2.17, we plot the reconstructed signal lineshape in the variable U, obtained from signal MC where $B \to \pi^0\pi^0\ell\nu$ events were generated in phase-space.

Since the reconstruction of two π^0's requires four γ's to be detected, final state radiation (FSR) is sufficiently non-negligible to shift the signal peak away from $U = 0$, as evident in Fig. 2.17. The signal reconstruction resolution here is also poor, due to the large FSR. It is not clear from Fig. 2.16 whether there is a robust peak from the signal or not. Further, even if we quote an upper limit on the signal component, it is non-trivial deciding how to utilize

that in an angular analysis on the $B \to \rho\ell\nu$ channels. Therefore, with the current *BABAR* dataset, we neglect any S-wave component under the P-wave.

2.14 Summary

In this chapter we provided details of the signal selection methods and analysis cuts to obtain a clean sample of $B \to \rho^0\ell\nu$ events. The remnant background will be removed by the signal-background separaton method, as described in the subsequent chapter.

Chapter 3

Signal Background Separation

We describe our yield extraction procedure in this chapter. Our main fit variable for signal extraction is U, but we also consider the reconstructed ρ mass variable $M(\pi\pi)$. We perform our signal/background separation fits either 1-D in U with a $M(\pi\pi) \in [0.67, 0.87]$ GeV cut, or 2-D fits in U-$M(\pi\pi)$ with a wide window in $M(\pi\pi)$.

3.1 Lineshape issues for $M(\pi\pi)$

3.1.1 The phase-space factor $\Phi_{\mathbf{PS}}(m, \mathbf{mm}^2, q^2)$

Consider the decay chain $B \to \rho(\to \pi\pi)W^*(\to \ell\nu)$, where $m = M(\pi\pi)$, $\sqrt{q^2} = M(\ell\nu)$ and m_B is the mass of the parent B. The $B \to \rho W^*$ break-up momentum (as a two-body decay) is $\mathbf{k}$ as in Eq. 1.6a, while that for $\rho \to \pi\pi$ is $p_\rho = m\sqrt{1 - 4m_\pi^2/m^2}/2$. For $W^* \to \ell\nu$, ignoring the lepton mass, if $\mathrm{mm}^2 \equiv p^2_{miss}$ is the mass-squared of the reconstructed missing neutrino, the $W^*(\to \ell\nu)$ break-up momentum is

$$p_{W^*} = \frac{q^2 - \mathrm{mm}^2}{2\sqrt{q^2}}. \tag{3.1}$$

Since $p_{W^*} > 0$, this factor suppresses events in the large mm^2 "tail" where $\mathrm{mm}^2 \geq q^2$. At large $q^2 > |\mathrm{mm}^2|_{\max}$, this phase-space suppression does not play any significant role. However, at low $q^2 \approx \mathcal{O}(|\mathrm{mm}^2|_{\max})$ this factor results in a phase-space suppression of the large mm^2 region.

The full phase-space factor is then

$$\begin{aligned}\frac{dN}{dm^2dq^2} &\equiv \Phi_{\rm PS}(m, {\rm mm}^2, q^2) \\ &\propto \left(\frac{\mathbf{k}}{m_B}\right)\left(\frac{p_\rho}{m}\right)\left(\frac{p_{W^*}}{\sqrt{q^2}}\right) \\ &\propto \sqrt{\left(1-\frac{(m+\sqrt{q^2})^2}{m_B^2}\right)\left(1-\frac{(m-\sqrt{q^2})^2}{m_B^2}\right)\left(1-\frac{4m_\pi^2}{m^2}\right)\left(1-\frac{{\rm mm}^2}{q^2}\right)}\end{aligned} \tag{3.2}$$

Note that $\Phi_{\rm PS}$ applies for both the signal and background pdf's, since it is a kinematic factor.

3.1.2 Relations among U, mm^2, q^2 and $\cos\theta_\ell$ at low q^2

Eq. 3.2 refers to mm^2, while we choose to use U as the fit parameter. The variable mm^2 is a product of two "semi"-independent quantities U and $|\vec{p}_{\rm miss}|$

$${\rm mm}^2 = (E_\nu - p_\nu) \times (E_\nu + p_\nu) \approx 2\, U\, |\vec{p}_{\rm miss}|. \tag{3.3}$$

We say that U and $|\vec{p}_{\rm miss}|$ are "semi"-independent, because U represents the resolution in the reconstruction of $|\vec{p}_{\rm miss}|$ and as $|\vec{p}_{\rm miss}| \to 0$, the magnitude of U tends to 0 as well. While $\cos\theta_\ell = -\cos\theta_\nu$ does not appear in Eq. 3.2, when switching from mm$^2 \to U$ as the fit variable, $\cos\theta_\ell$ does enter the fray because $|\vec{p}_{\rm miss}| \approx E_\nu^*$ depends on both q^2 and $\cos\theta_\ell$ as (see Eq. 1.6)

$$|\vec{p}_{\rm miss}| \approx E_\nu^* = \frac{1}{4m_B}\left[(m_B^2 + q^2 - m_X^2) - 2m_B\mathbf{k}\cos\theta_\ell\right], \tag{3.4}$$

where $m_X \equiv M(\pi\pi)$. At large q^2, the first term in the rhs of Eq. 3.4 dominates. At low q^2, the second term starts to dominates and suppresses $|\vec{p}_{\rm miss}|$, and thereby, U. The relationship can not be disentangled to give a simple dependence on *just* U, but overall, we note that at low q^2, for a given value of mm^2, large $|U|$ values are suppressed more at $\cos\theta_\ell \to -1$ than at $\cos\theta_\ell \to +1$ because $U \sim {\rm mm}^2/|\vec{p}_{\rm miss}|$ and $1/|\vec{p}_{\rm miss}|$ is suppressed more at $\cos\theta_\ell \to -1$.

The above discussion pertains to the reconstructed q^2 and $\cos\theta_\ell$ with the ν not mass-constrained during the vertex fitting. For the values of q^2 and $\cos\theta_\ell$ that were reconstructed out of the 4-vectors corresponding to the event being fit with the ν mass-constrained, there is no appreciable dependance of the U pdf shapes on the (reconstructed) phase-space regions. However, if one considers the (reconstructed) phase-space kinematic variables without the ν mass-constrained, there is some expected phase-space dependance of the fit pdf's in U.

3.1.3 The ρ signal lineshape

To get the ρ signal lineshape, we note that

$$\frac{dN}{dm^2dq^2} \propto \Phi_{\rm PS}(m, {\rm mm}^2, q^2)|\mathcal{A}|^2 \tag{3.5}$$

where the $\rho \to \pi\pi$ amplitude is given by

$$\mathcal{A} \sim \left(\frac{p_\rho}{p_0}\right)^L \frac{B^L(p_\rho, R)}{B^L(p_0, R)} \frac{1}{m^2 - m_0^2 + im_0\Gamma_{\rm tot}(m)}. \tag{3.6}$$

Here $L = 1$ for the P-wave decay and the corresponding phenomenological angular momentum barrier factor is

$$B^{L=1}(p, R) = \frac{1}{\sqrt{1 + p^2R^2}}, \tag{3.7}$$

with $R = 3$ GeV^{-1} corresponding to a meson radius of about 0.6 fm, and $\Gamma_{\rm tot}$ is the mass-dependent total width. Since $\rho \to \pi\pi$ has $\sim 100\%$ bf, this is the only decay channel, and the width is given by

$$\Gamma_{\rm tot}(m) = \Gamma_0 \left(\frac{p_\rho^2}{1 + p_\rho^2R^2} \frac{1 + p_0^2R^2}{p_0^2}\right) \frac{p_\rho}{m} \frac{m_0}{p_0}, \tag{3.8}$$

where $\Gamma_0 = 0.149$ GeV, $m_0 = 0.775$ GeV and $p_0 \equiv p_\rho(m_0)$.

Putting everything together, we take the signal lineshape as a mass-dependent relativistic Breit-Wigner:

$$\tilde{\mathcal{B}}(m, q^2) \equiv \frac{dN}{dmdq^2} \propto m\Phi_{\rm PS}(m, 0, q^2) \frac{p^2}{1 + p^2R^2} \frac{1 + p_0^2R^2}{p_0^2} \frac{1}{(m^2 - m_0^2)^2 + (m_0\Gamma_{\rm tot}(m))^2}, \tag{3.9}$$

where $m = M(\pi\pi)$, $p \equiv p_\rho(m) = \sqrt{m^2 - 4m_\pi^2}/2$ is the break-up momentum of the $(\pi\pi)$ system. It is clear from Eq. 3.9 the lineshape is modulated by the q^2 dependance in the phase-space factor. This effect is most pronounced at the edges of the phase space at $q^2 \to q^2_{max}$, as shown in Fig. 3.1.

In principle, one can fold the above lineshape with a Gaussian detector resolution function of width σ, so that the final signal-lineshape function is

$$\mathcal{B}(m, q^2) = \int_{m-5\sigma}^{m+5\sigma} \tilde{\mathcal{B}}(m', q^2) \frac{e^{-\frac{(m-m')^2}{2\sigma^2}}}{\sqrt{2\pi}\sigma} dm'. \tag{3.10}$$

However, since the ρ width is much larger than any other resolution effects, this effect is negligible and under the assumption that there is no S-wave under the ρ, we take the signal lineshape in $M(\pi\pi)$ to be fixed as in Eq. 3.9.

3.2 The Q-value method

To confront the issue of signal-background separation, we note several facets of the problem at hand. If one tried to considering a full 4-dimensional analysis for the vector mesons, with reasonable bin-widths in all four variables (q^2, $\cos\theta_\ell$, $\cos\theta_V$ and χ), we do not have adequate statistics. Typically, for the charmless modes, at the most, past analyses [37] have tried to

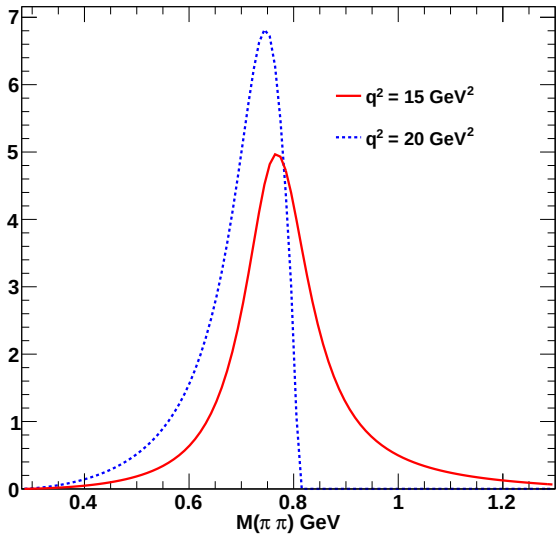

Figure 3.1: The $M(\pi\pi)$ lineshape as given by Eq. 3.9, for two different values of q^2 and $\mathrm{mm}^2 = 0$.

extract differential rates in a few q^2 bins, integrating over the other variables. However, this clearly leads to loss of information contained in the other angular distributions. For example, for $B \to \pi\ell\nu$, we know that irrespective of any other physics, we expect an overall $\sin^2\theta_\ell$ distribution. Therefore, within a given q^2 bin, if the background distribution peaks at $\theta_\ell \to 0$ (for example, from the continuum), this will give an incorrect assesment of the background at $\theta_\ell \to \pi/2$, where the signal peaks. In other words, both the shape and strength of the signal and background components can vary (sometimes strongly) in phase-space. A fit to the cumulative distribution can therefore be unsuitable. Employing Monte Carlo "template shapes" that are expected to already have these distributions help a bit, but if one is trying to extract the angular distributions themselves, it does not work again.

In the present analysis, we have tried to address this problem in the following way. For a given event, we consider only events that are "close" enough in the full multi-dimensional phase-space. A possible metric d_{ij} for "closeness" between the i^{th} and j^{th} events is the following:

$$d_{ij}^2 = \sum_a \left(\frac{\phi_i^a - \phi_j^a}{r_a} \right)^2 , \tag{3.11}$$

where r_a is the range of the kinematic variable $\phi^a \in \{q^2, \cos\theta_\ell, \cos\theta_V, \chi, \cos\theta_B\}$ in 5-D space, where we note that the full production rate also depends on the B polar angle θ_B as $\sin^2\theta_B$. For example, the range can be q^2_{max} for q^2 and 2π for χ, etc. The motivation for this distance metric is that the signal/background shape and level is expected to not vary much within small regions of phase-space, since the physics remains the same.

For $B \to \rho^0\ell\nu$ channel, given the sparse statistics, instead of the full 5-D phase-space, we have chosen to consider only the variables $\{q^2, \cos\theta_\ell\}$ for our background subtraction, since the signal dynamics is most strongly dependent on these two variables. Note that if the

signal to background ratio, or the signal and background pdf's do not vary too strongly in a particular kinematic variable, then one can average over that particular variable. The chief goal of binning finely in phase-space is to track any phase-space dependence of the S/B ratio and the pdf shapes. We additionally require that $\frac{\phi_i^a - \phi_j^a}{r_a} < \alpha$ for the two variables q^2 and $\cos\theta_\ell$, where $\alpha = 0.1$ towards the edge bins ($|\cos\theta_\ell| \to 1$, $q^2 \to q^2_{\{\text{min, max}\}}$) to 0.3 towards the central bins ($|\cos\theta_\ell \to 0$, $q^2 \to 10$). This is because the S/B varies most strongly at the phase-space edge regions. Especially, at $q^2 \to 0$, where the signal dies off, there is a large continuum background.

Having defined the closeness metric, one can then choose the closest N_c number of events around the i^{th} event, perform the background subtraction procedure on these $N_c + 1$ events and extract the signal ($\mathcal{S}$) and background ($\mathcal{B}$) PDF's. The i^{th} event is then assigned a Q-value:

$$Q_i = \frac{\mathcal{S}(\vec{x}_i)}{\mathcal{S}(\vec{x}_i) + \mathcal{B}(\vec{x}_i)} \tag{3.12}$$

where $\vec{x} = \{U, M(\pi\pi)\}$ represents the variables in which the fit is performed. The Q-value represents the probability that the event is a good signal event and is used as a weight for the event.

3.3 2-D fits in U-$M(\pi\pi)$

3.3.1 Signal PDF

At low q^2, there is a phase-space suppression on the high U side, because here, the magnitude of E_ν^* is itself small (recall that U represents the resolution in E_ν^* measurement). There is also a slight dependance of the lineshape on $\cos\theta_\ell$, at low q^2. Other than this, the U signal PDF resolutions are not expected to vary too much in phase-space. However, the e/μ samples need to be processed separately, since the e channel has more FSR. The full signal PDF is constructed as a sum of four bifurcated Gaussians ($g_{\text{bif}}(x, \mu, \sigma^L, \sigma^R)$):

$$\mathcal{S}(U) = s_1(g_{\text{bif}}(U, \mu_1, \sigma_1^L, \sigma_1^R) + s_2 g_{\text{bif}}(U, \mu_2, \sigma_2^L, \sigma_2^R) + s_3 g_{\text{bif}}(U, \mu_3, \sigma_3^L, \sigma_3^R) + s_4 g_{\text{bif}}(U, \mu_4, \sigma_4^L, \sigma_4^R)) \tag{3.13}$$

The first two components are centered around $U = 0$, representing the signal peak, and the third and fourth on the low and high end of the U spectrum, repectively, representing the tails. Figs. 3.3a, 3.4a and 3.5a show sample fits for three particular events, where Gaussians 1 and 2 are the central ones and 3 and 4 are the tails. We impose limits on the ranges of the parameters in Eq. 3.13 as tabulated in Table 3.1. These ranges were placed such that the tails did not peak at $U \sim 0$ and had appropriate high and low U asymmetric shapes.

After the initial values of the sixteen free parameters in $\mathcal{S}(U)$, is set by the aforementioned fit, we fix the parameters corresponding to the tail shapes, viz., μ_3, σ_3^L, σ_3^R, μ_4, σ_4^L, and

Parameter	Range
μ_1	$[-0.005, 0.01]$ GeV
σ_1^L	$[0.022, 0.045]$ GeV
σ_1^R	$[0.02, 0.045]$ GeV
s_2	$[0.05, 50]$
μ_2	$[-0.005, 0.01]$ GeV
σ_2^L	$[0.022, 0.045]$ GeV
σ_2^R	$[0.02, 0.045]$ GeV
s_3	$[0, 0.1]$
μ_3	$[0.04, 0.1]$ GeV
σ_3^L	$[0.01, 0.05]$ GeV
σ_3^R	$[0.03, 0.2]$ GeV
s_4	$[0, 0.1]$
μ_4	$[-0.055, -0.025]$ GeV
σ_4^L	$[0.03, 0.1]$ GeV
σ_4^R	$[0.01, 0.03]$ GeV

Table 3.1: The allowed ranges of the fit parameters in the signal function as in Eq. 3.13.

σ_4^R. The central bifurcated Gaussians and the relative strengths of the tails (s_3 and s_4) are allowed to float.

The $M(\pi\pi)$ signal PDF is the (fixed) mass-dependent relativistic BW as given in Eq. 3.9. The q^2 dependent phase-space term is averaged over the range of Δq^2 spanned by the $N_c + 1$ events. The full 2-D signal PDF is the product of the U and the $M(\pi\pi)$ PDF's.

3.3.2 Background PDF

As noted earlier, an important emphasis of this analysis is to ensure that the background shape in the signal fit variable U is smooth under the signal peak. Fig. 3.2 shows this, employing the MC. We parameterize the background shape in U shape as a sum of the tails of two Gaussians. At low q^2, there is again a phase-space suppression on the high U side. The phase-space suppression is difficult to be analytically parameterized in terms of U, since it is really dependent on E_ν^*. The generic functional form that is able to accomodate the entire q^2 range is a sum of two bifurcated Gaussians:

$$\mathcal{B}(U) = b_1(g_{\text{bif}}(U, \tilde{\mu}_1, \tilde{\sigma}_1^L, \tilde{\sigma}_1^R) + b_2 g_{\text{bif}}(U, \tilde{\mu}_2, \tilde{\sigma}_2^L, \tilde{\sigma}_2^R)) \tag{3.14}$$

Table 3.2 shows the allowed ranges of the fit parameters. The second bifurcated Gaussian is relatively suppressed since it is meant to parameterize any non-uniformity close to the signal region, especially at low q^2. Above $q^2 \sim 2$ GeV^2, the shape boils down to a generic slowly rising function in U. Again, the e/μ samples are processed separately, since the backgrounds are different. Figs. 3.3b, 3.4b and 3.5b show sample fits for three particular events.

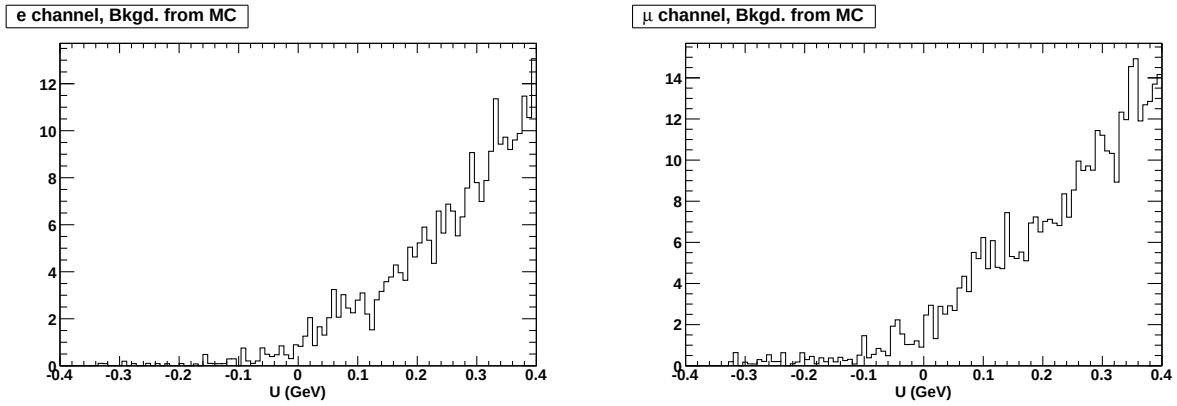

(a) (b)

Figure 3.2: The cumulative background shapes taken from the MC for (a) electron and (b) muon. There is no peaking component across $U = 0$ GeV.

Parameter	Range
$\tilde{\mu}_1$	$[0.05, 5]$ GeV
$\tilde{\sigma}_1^L$	$[0.05, 2]$ GeV
$\tilde{\sigma}_1^R$	$[0.05, 5]$ GeV
b_2	$[0, 0.05]$
$\tilde{\mu}_2$	$[0, 0.04]$ GeV
$\tilde{\sigma}_2^L$	$[0.04, 0.1]$ GeV
$\tilde{\sigma}_2^R$	$[0.1, 1]$ GeV

Table 3.2: The allowed ranges of the fit parameters in the bkgd. function as in Eq. 3.14.

Parameter	Range
$\bar{\mu}_1$	$[-2, 0.48]$ GeV
$\bar{\sigma}_1$	$[0.08, 10]$ GeV
c_2	$[0, 1000]$
$\bar{\mu}_2$	$[0.75, 0.82]$ GeV
$\bar{\sigma}_2$	$[0.12, 0.2]$ GeV
β_2	$[0, 1]$/GeV
c_3	$[0, 1000]$
$\bar{\mu}_3$	$[1.2, 10]$ GeV
$\bar{\sigma}_3$	$[0.08, 10]$ GeV
β_3	$[0, 1]$/GeV

Table 3.3: The allowed ranges of the fit parameters in the bkgd. function as in Eq. 3.15.

For $M(\pi\pi)$, we model the background lineshape as the sum of three Gaussians – one centered around $M(\pi\pi) \sim 0.77$, and two others on the low and high sides. Note that the central Gaussian corresponds to true $\rho^0 \to \pi^+\pi^-$ combinations that did not come from a signal $B \to \rho^0\ell\nu$ event. Since ρ's are produced generically in a multitude of processes, such ρ events are ubiquitous, but lie away from the signal $U \sim 0$ region. The low- and high-side pieces are modeled as long Gaussian tails, that is, their means are specified to be away from the signal region in $M(\pi\pi)$. To accomodate a slight U dependence in the relative scales between the three Gaussians, we incorporate an exponential factor. Thus the background function in $m \equiv M(\pi\pi)$ is

$$\mathcal{B}(m) = g(m, \bar{\mu}_1, \bar{\sigma}_1) + c_2 g(m, \bar{\mu}_2, \bar{\sigma}_2) e^{U\beta_2} + c_3 g(m, \bar{\mu}_3, \bar{\sigma}_3) e^{U\beta_3} \tag{3.15}$$

where the first, second and third gaussian functions are for the low-side, middle and high-side background shapes, respectively. The ranges of the parameters are listed in Table 3.3.

The q^2 dependent phase-space suppression term is included just as for the signal $M(\pi\pi)$ relativistic BW. Figs. 3.3c, 3.4c and 3.5c show samples fits for three particular events.

3.3.3 Total fit function

For each of the signal and background components, we take the total function as a direct product between the U- and m-dependent parts. Therefore the total fit function is

$$\mathcal{F}(U, m) = \mathcal{S}(U) \times rBW(m) + \mathcal{B}(U) \times \mathcal{B}(m). \tag{3.16}$$

In all, we have 28 fit parameters.

3.3.4 Fit validation using "mock Data" samples

To validate our fitting method, we create a "mock Data" sample from the generic $B\overline{B}$ and continuum MC samples. The composition of each individual component is weighted to the

data luminosity according to the corresponding cross-sections. We then pseudo-randomly accept or reject any event in this sample using the corresponding lumi-weight as a trigger level. That is, the "mock Data" sample is completely representative of the expected Data sample in both composition and statistics. The only difference is that, being composed out of the MC, the "mock Data" also includes the truth information. We extract the Q-values for each "mock Data" event and compare the Q-value weighted distribution in any relevant kinematic variable, with the corresponding truth-matched distribution. The procedure is validated if these two distributions match, within statistical error bars.

In what follows in the rest of this section, we will refer to the "mock Data" sample as "Data" and treat it as we would treat the Data.

3.3.5 Fit set-up and synopsis of steps

We define "signal MC" as truth-matched $B \to \rho\ell\nu$ events from all available MC samples. This comprises the truth-matched signal content in the generic $B\overline{B}$ MC ($\times 10$ Data luminosity and $B \to \rho\ell\nu$ events generated according to the ISGW2 model), as well as ~ 8.85 M signal $B \to \rho\ell\nu$ events generated flat in all kinematic variables using the `FLATQ2` generator. The signal pdf shape is not expected to have much dependence on the generator model, so, to bolster statistics, we merge both samples and denote this entire available truth-matched $B \to \rho\ell\nu$ sample as "signal MC". Our definition of "generic MC" is the entire available $B\overline{B}$ and continuum MC sample. The steps to extract the Q-factor for *one particular event*, are as follows:

1. For the given i^{th} event, we select the closest N_c Data sample events in the 2-D phase-space of $\{q^2, \cos\theta_\ell\}$ using the metric defined by Eq. 3.11.

2. We note the values q_i^2 and $(\cos\theta_\ell)_i$ for this event and select signal MC and generic MC events that lie within the phase-space "box" $q_i^2 \pm \delta_1$ and $(\cos\theta_\ell)_i \pm \delta_2$. The widths $\delta_{1,2}$ are kept narrower at the phase-space edges:

$$\delta_1 = 0.08 + 0.22(1 - |q_i^2/(q_{max}^2/2) - 1|) \tag{3.17}$$
$$\delta_2 = 0.08 + 0.22(1 - |(\cos\theta_\ell)_i|) \tag{3.18}$$

   The phase-space "box" for the signal/generic MC is intentionally kept wider than that for the Data to bolster statistics, since we use fits to the former only to extract the start values of the different fit parameters. We denote the signal/generic MC samples thus chosen as the "reduced" MC samples. The exact number of events in these reduced samples varies event-to-event, but, by construction, they have high statistics.

3. We perform a fit to the reduced signal MC using the pdf shapes defined in Eq. 3.13. Examples of these fits are Figs. 3.3a, 3.4a etc. The parameters $\mu_{3,4}$, $\sigma_{3,4}^L$ and $\sigma_{3,4}^R$ in Eq. 3.13 are fixed, hereonwards. That is, the shapes of the tails in the signal U distribution are fixed from fits to the signal MC shape.

4. We perform fits to the 1-D distributions in U and $M(\pi\pi)$ to the truth-matched background (ie, non-signal) components in the reduced generic MC, employing the pdf's Eq. 3.14 and 3.15, respectively. Sample fits are in Figs. 3.3b and 3.3c, respectively. The fit parameters extracted in this step are taken as *start values* for the corresponding parameters in Eq. 3.16.

5. Once the corresponding start values for the shape parameters in Eq. 3.16 have been obtained, we perform a full unbinned ML fit to the $N_c + 1$ events in the Data sample. The normalizations are always unrestricted and kept floating.

In the final fit to the Data, the signal and background normalizations are kept completely floating. For the shape parameters, we take the start values of the shape parameters from fits to the signal/generic MC. We define two parameters $\lambda_{\{s,b\}} \in [0, 1]$ corresponding to signal and background, respectively. For each fit parameter x, if x_0 is the start value, the allowed range in the final data fits is $x \in [\lambda x_0, x_0/\lambda]$. That is, $\lambda \to 1$ indicates that the parameter is completely fixed to the start value extracted from the MC, while $\lambda \to 0$ would indicate a very loose restriction.

3.3.6 Sample fit flow for particular events

Figs. 3.3, 3.4 and 3.5 show the sequence of fits for particular events with a choice of $N_c = 50$, $\lambda_s = \lambda_b = 0.7$. The corresponding set of fit results for the shape parameters are provided in Tables 3.4, 3.5 and 3.6, respectively. We note that our fit-qualities are limited by the following feautures – we are highly statistics limited, the ρ has a substantial amount of background and finally, in the ideal case, these fits should be performed as 1-D fits in U in small $M(\pi\pi)$ bins. We are forced to resort to a complicated 2-D fit in U-$M(\pi\pi)$ because of our limited data sample.

3.3.6.1 Event 1

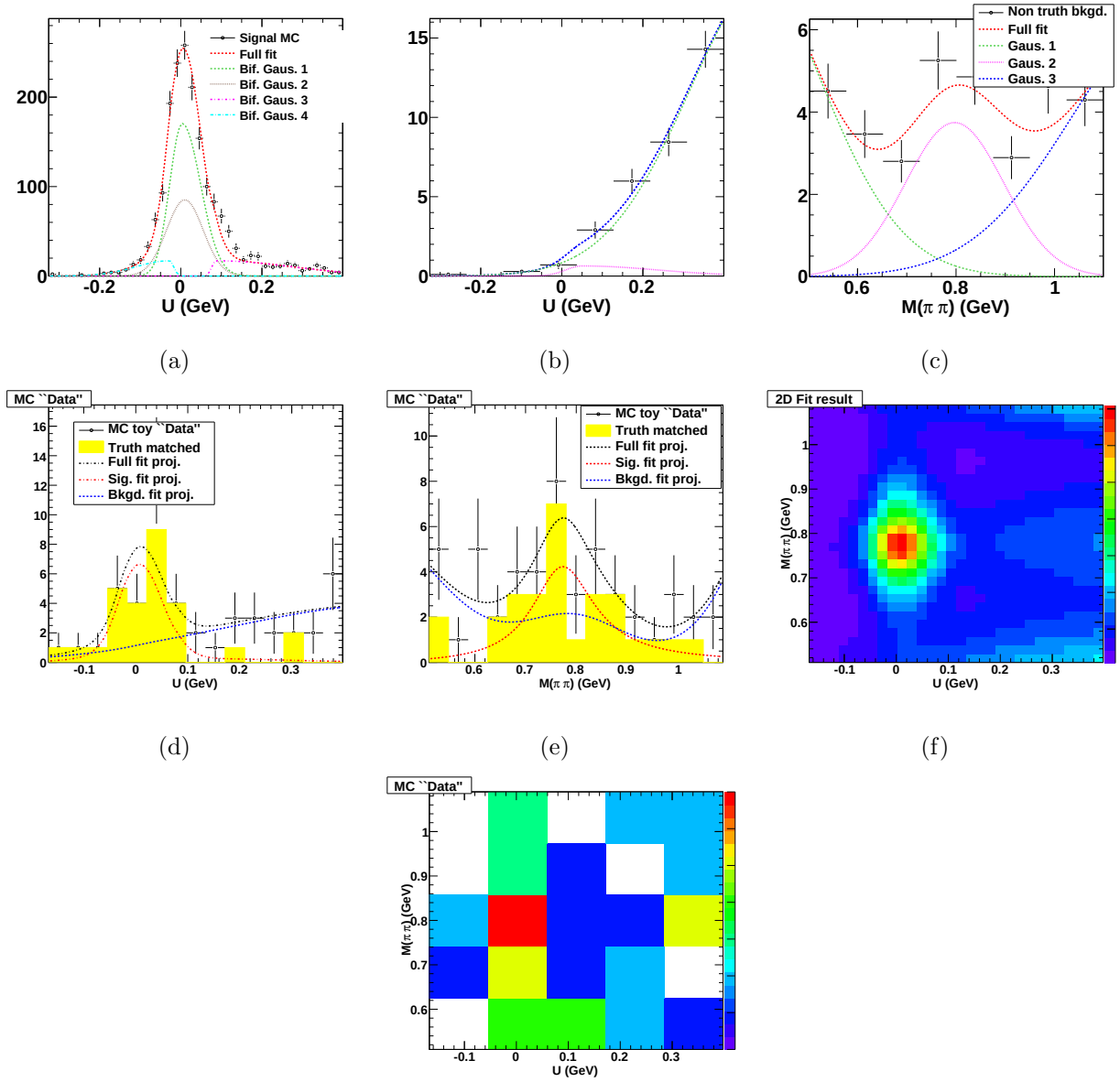

Figure 3.3: Results from a randomly chosen event fit with $N_c = 50$, $\lambda_s = 0.7$ and $\lambda_b = 0.7$: (a) initial fit to the signal MC in U (b) initial fit to the background MC in U (c) initial fit to the background MC in $M(\pi\pi)$ (d) 2-D fit results projected in U (e) 2-D fit results projected in $M(\pi\pi)$ (f) functional form of the 2-D fit result (g) 2-D distribution as in the Data. See Table 3.4 for the numerical values of the fit parameters.

Parameter	Fit result	Error
$\tilde{\mu}_1$	0.428625	0.0770
$\tilde{\sigma}_1^L$	0.299607	0.12598
$\tilde{\sigma}_1^R$	1.53203	0.300624
b_2	0.0468847	0.0151265
$\tilde{\mu}_2$	0.046576	0.0102836
$\tilde{\sigma}_2^L$	0.05	0.00548737
$\tilde{\sigma}_2^R$	0.129633	0.11125
$\bar{\mu}_1$	0.25147	0.03006
$\bar{\sigma}_1$	0.171028	0.016009
c_2	0.0783438	0.0281
$\bar{\mu}_2$	0.784166	0.03851
$\bar{\sigma}_2$	0.1	0.0408
β_2	1.06963	1.040
c_3	1.43472	0.03228
$\bar{\mu}_3$	0.163414	0.013103
$\bar{\sigma}_3$	0.999705	0.9298
β_3	0.99987	0.960113

Parameter	Fit result	Error
μ_1	0.00501227	0.00201
σ_1^L	0.0326541	0.016740
σ_1^R	0.045	0.012867
s_2	0.01	0.0017092
μ_2	0.045	0.00310296
σ_2^L	0.045	0.0130095
σ_2^R	0.714005	0.303502
s_3	0.0700039	0.028065
s_4	0.1	0.015009

Table 3.4: The numerical values of the shape parameters in the fit result corresponding to Fig. 3.3. The LHS table correspondings to the background and the RHS, to the signal parameters.

3.3.6.2 Event 2

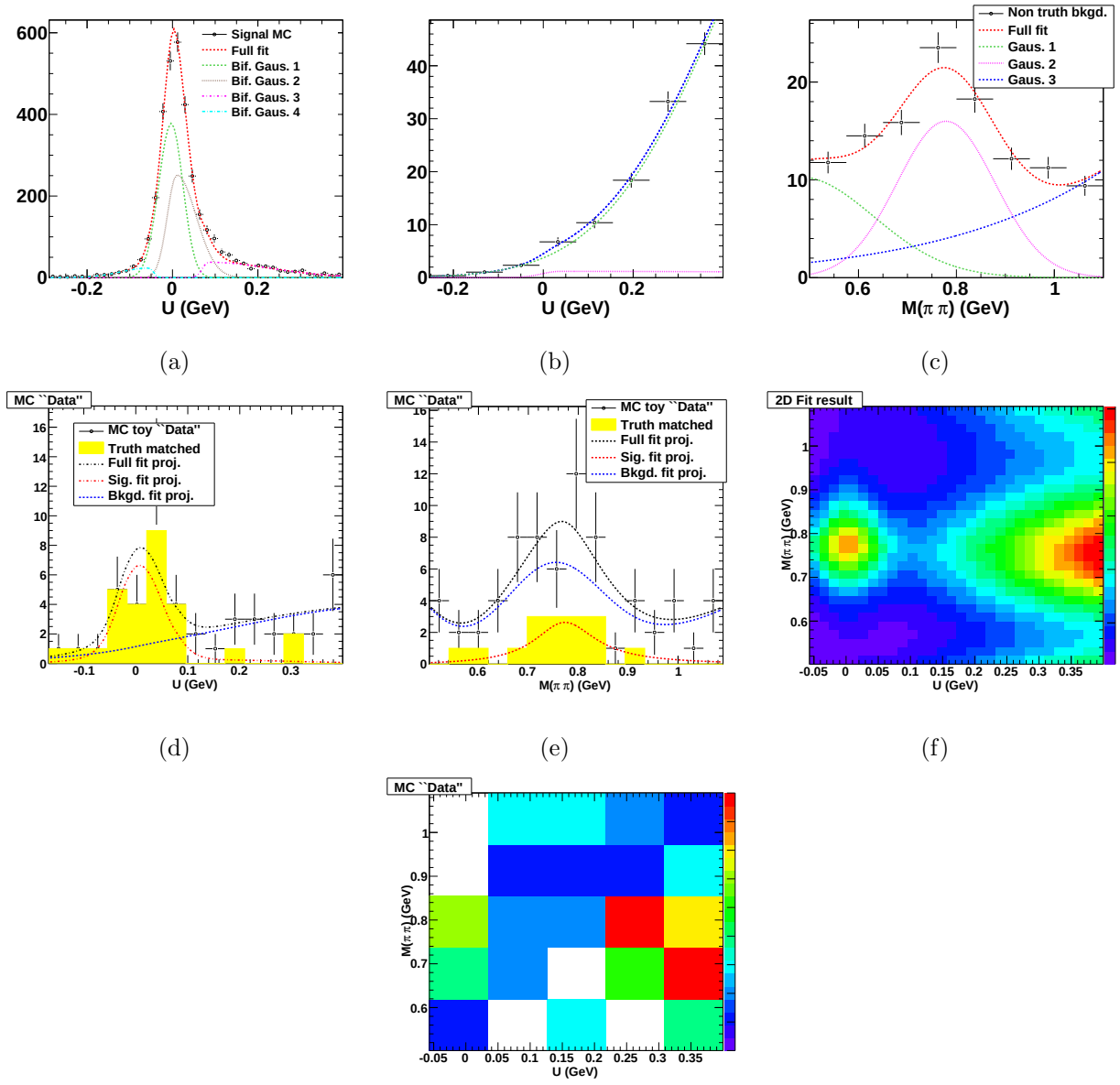

Figure 3.4: Results from a randomly chosen event fit with $N_c = 50$, $\lambda_s = 0.7$ and $\lambda_b = 0.7$: (a) initial fit to the signal MC in U (b) initial fit to the background MC in U (c) initial fit to the background MC in $M(\pi\pi)$ (d) 2-D fit results projected in U (e) 2-D fit results projected in $M(\pi\pi)$ (f) functional form of the 2-D fit result (g) 2-D distribution as in the Data. See Table 3.5 for the numerical values of the fit parameters.

Parameter	Fit result	Error
$\tilde{\mu}_1$	0.459768	0.109978
$\tilde{\sigma}_1^L$	0.214032	0.0235766
$\tilde{\sigma}_1^R$	1.38078	0.270
b_2	0.0202717	0.0069775
$\tilde{\mu}_2$	0.0285006	0.0067133
$\tilde{\sigma}_2^L$	0.0564502	0.001778
$\tilde{\sigma}_2^R$	1.42325	0.16501
$\bar{\mu}_1$	0.336574	0.1108
$\bar{\sigma}_1$	0.106038	0.071669
c_2	0.270581	0.051807
$\bar{\mu}_2$	0.739219	0.021558
$\bar{\sigma}_2$	0.1	0.028785
β_2	254.162	199.10
c_3	4.26106	0.065166
$\bar{\mu}_3$	0.834532	0.016620
$\bar{\sigma}_3$	0.995851	0.9552
β_3	1.00022e-05	0.8883

Parameter	Fit result	Error
μ_1	-0.00389242	0.001673
σ_1^L	0.0421228	0.02147
σ_1^R	0.0387542	0.0187579
s_2	0.00703897	0.00201766
μ_2	0.0314275	0.0063869
σ_2^L	0.0439134	0.012884
σ_2^R	0.476069	0.28547
s_3	0.0700036	0.021493
s_4	0.0887516	0.041921

Table 3.5: The numerical values of the shape parameters in the fit result corresponding to Fig. 3.4. The LHS table correspondings to the background and the RHS, to the signal parameters.

3.3.6.3 Event 3

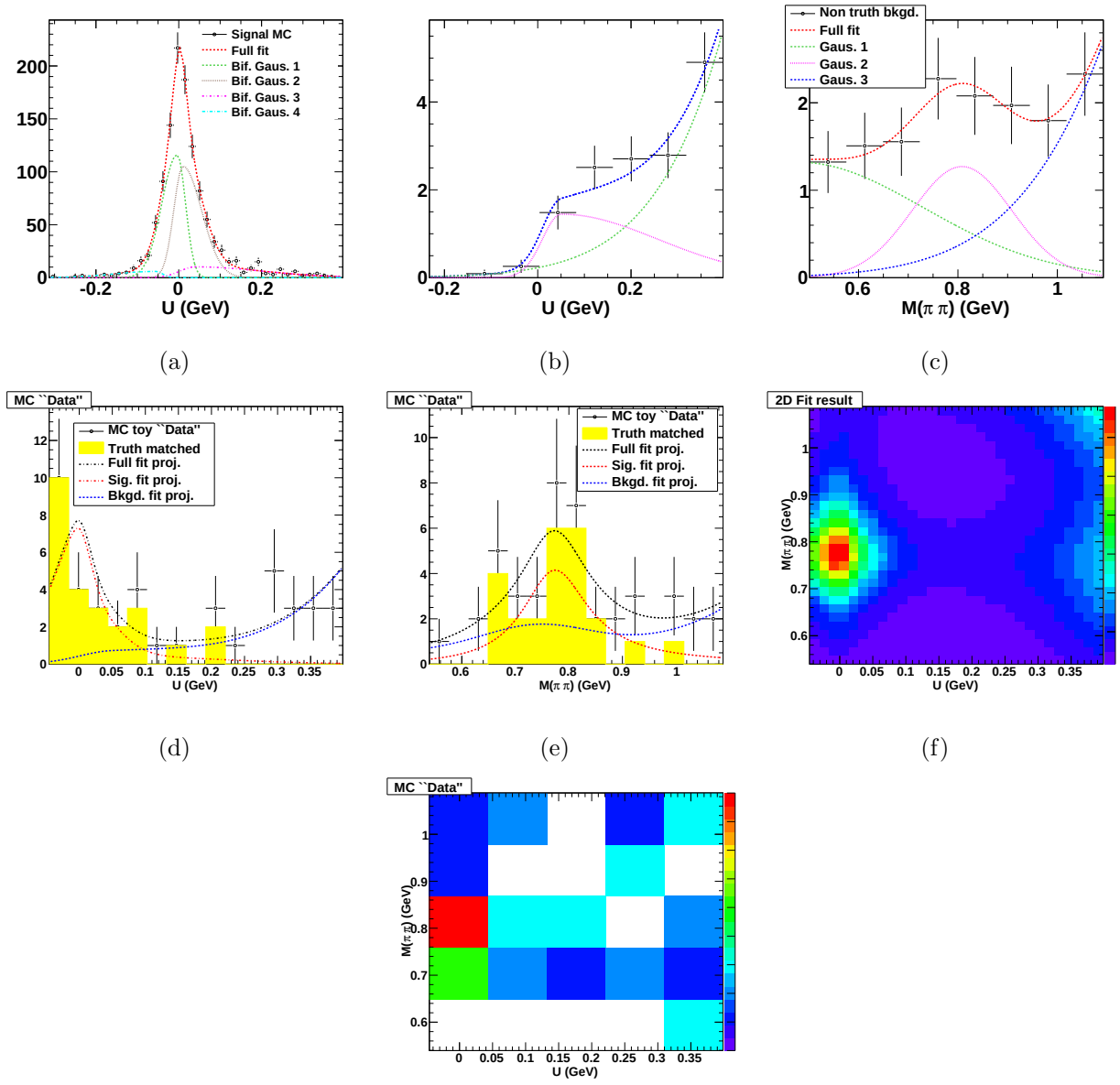

Figure 3.5: Results from a randomly chosen event fit with $N_c = 50$, $\lambda_s = 0.7$ and $\lambda_b = 0.7$: (a) initial fit to the signal MC in U (b) initial fit to the background MC in U (c) initial fit to the background MC in $M(\pi\pi)$ (d) 2-D fit results projected in U (e) 2-D fit results projected in $M(\pi\pi)$ (f) functional form of the 2-D fit result (g) 2-D distribution as in the Data. See Table 3.6 for the numerical values of the fit parameters.

Parameter	Fit result	Error
$\tilde{\mu}_1$	1.11931	0.0273837
$\tilde{\sigma}_1^L$	0.287482	0.221925
$\tilde{\sigma}_1^R$	3.5568	0.69793
b_2	0.00511652	0.001794
$\tilde{\mu}_2$	0.0499528	0.0034260
$\tilde{\sigma}_2^L$	0.0500228	0.0016312
$\tilde{\sigma}_2^R$	0.145103	0.1478
$\bar{\mu}_1$	0.478152	0.07271
$\bar{\sigma}_1$	0.35628	0.17563
c_2	1.14131	1.14666
$\bar{\mu}_2$	0.72764	0.091705
$\bar{\sigma}_2$	0.1	0.021938
β_2	20.5526	9.057
c_3	1.89986	0.07390
$\bar{\mu}_3$	0.363594	0.029767
$\bar{\sigma}_3$	0.00440145	0.5020
β_3	0.0154902	0.524842

Parameter	Fit result	Error
μ_1	-0.00499998	0.002448
σ_1^L	0.0449872	0.01881
σ_1^R	0.02	0.00691
s_2	0.00700068	0.0023761
μ_2	0.031427	0.00899
σ_2^L	0.045	0.01294
σ_2^R	0.634132	0.4838
s_3	0.0999475	0.0338
s_4	0.0721452	0.03640

Table 3.6: The numerical values of the shape parameters in the fit result corresponding to Fig. 3.5. The LHS table correspondings to the background and the RHS, to the signal parameters.

3.3.6.4 Event 4

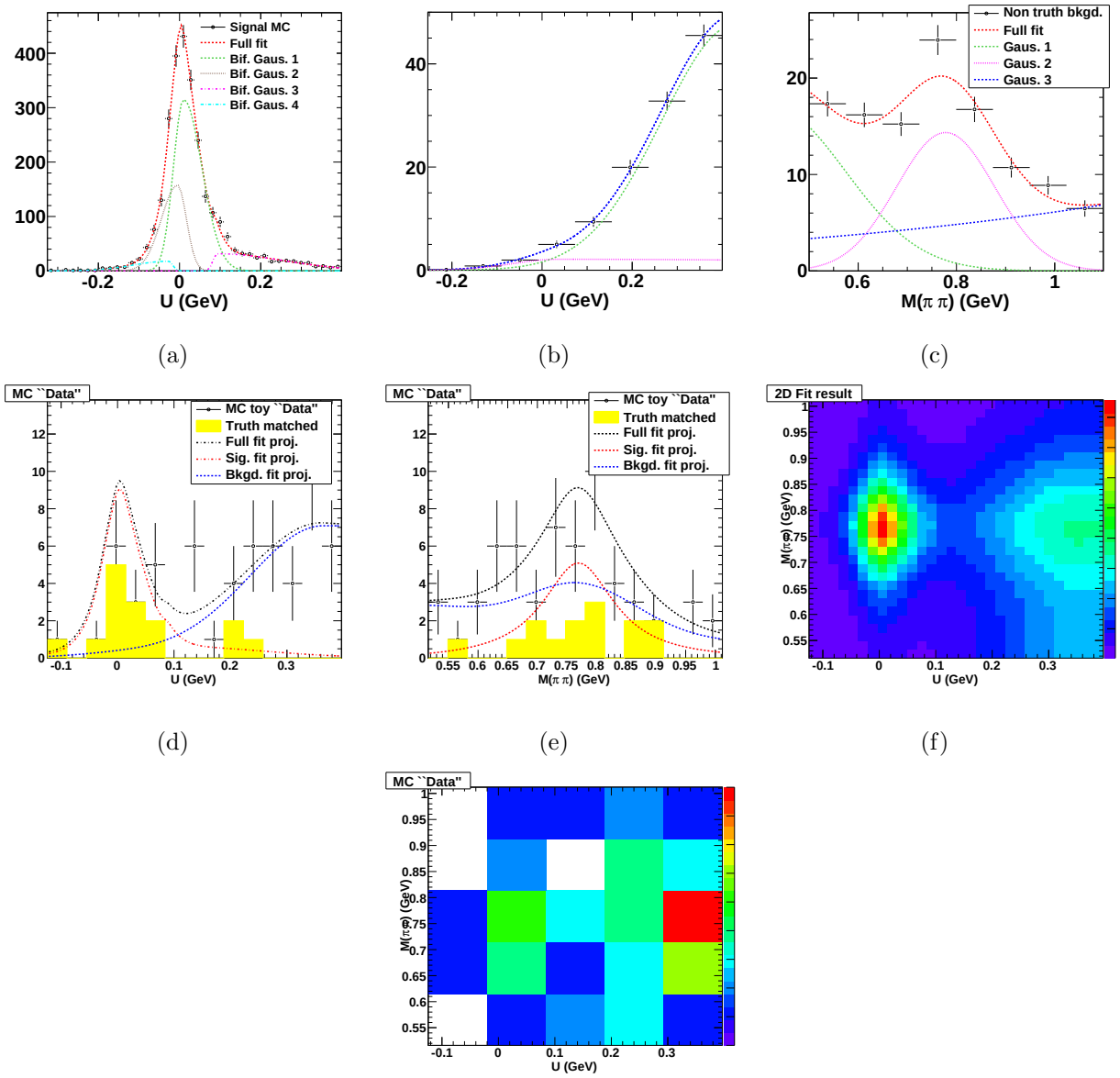

Figure 3.6: Results from a randomly chosen event fit with $N_c = 50$, $\lambda_s = 0.7$ and $\lambda_b = 0.7$: (a) initial fit to the signal MC in U (b) initial fit to the background MC in U (c) initial fit to the background MC in $M(\pi\pi)$ (d) 2-D fit results projected in U (e) 2-D fit results projected in $M(\pi\pi)$ (f) functional form of the 2-D fit result (g) 2-D distribution as in the Data. See Table 3.7 for the numerical values of the fit parameters.

Parameter	Fit result	Error
$\tilde{\mu}_1$	0.364297	0.046579
$\tilde{\sigma}_1^L$	0.129402	0.022872
$\tilde{\sigma}_1^R$	1.1703	0.30875
b_2	0.0446076	0.00627
$\tilde{\mu}_2$	0.0355424	0.0091489
$\tilde{\sigma}_2^L$	0.1	0.026389
$\tilde{\sigma}_2^R$	1	0.263793
$\bar{\mu}_1$	0.421571	0.13643
$\bar{\sigma}_1$	0.152534	0.0441
c_2	0.841095	0.32133
$\bar{\mu}_2$	0.777992	0.030559
$\bar{\sigma}_2$	0.100011	0.0062700
β_2	63.6823	28.888
c_3	9.84443	1.9243
$\bar{\mu}_3$	2.74756	0.58901
$\bar{\sigma}_3$	9.99522e-05	0.19429
β_3	9.99518e-05	0.15978

Parameter	Fit result	Error
μ_1	0.00999999	0.0004701
σ_1^L	0.0251366	0.00468
σ_1^R	0.045	0.0026
s_2	-0.005	0.000244
μ_2	0.0397601	0.0127
σ_2^L	0.022	0.001268
σ_2^R	0.5	0.1314
s_3	0.1	0.004996
s_4	0.0562755	0.0146

Table 3.7: The numerical values of the shape parameters in the fit result corresponding to Fig. 3.6. The LHS table correspondings to the background and the RHS, to the signal parameters.

3.3.7 Extracted signal distributions

Fig. 3.7 and Fig. 3.8 shows the extracted signal components plotted in several different variables for the choice $\lambda_s = 0.95$, $\lambda_b = 0.7$ and $N_c = 50$. The bottom pads depicts the ratio between the extracted and truth-matched yields, which are expected to be ≈ 1. Overall, within statistical limitations, we find reasonable agreement between the two.

The signal (red) and background (blue) components are obtained by assigning the weights Q and $(1-Q)$, respectively, to each event. Since the signal and background components are extracted in an event-by-event way and are constrained to sum up to the total, the statistical fluctuations appear somewhat correlated between the total, the signal and the background components.

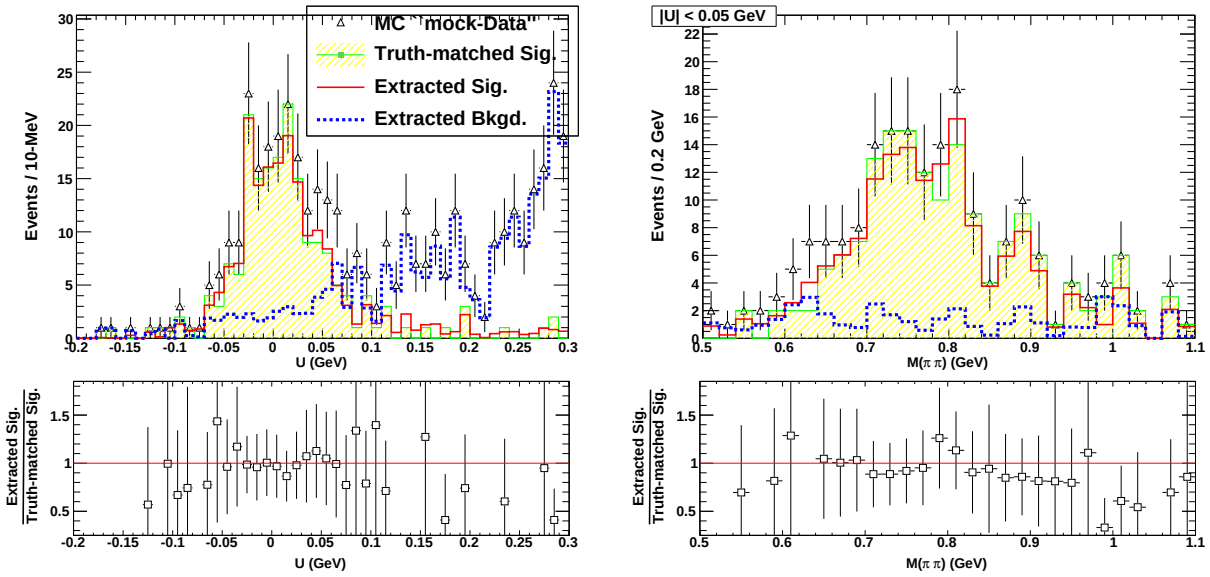

(a) (b)

Figure 3.7: $B \to \rho^0 \ell\nu$ signal-background fit results for (a) U and (b) $M(\pi\pi)$. Here $\lambda_s = 0.95$, $\lambda_b = 0.7$ and $N_c = 50$.

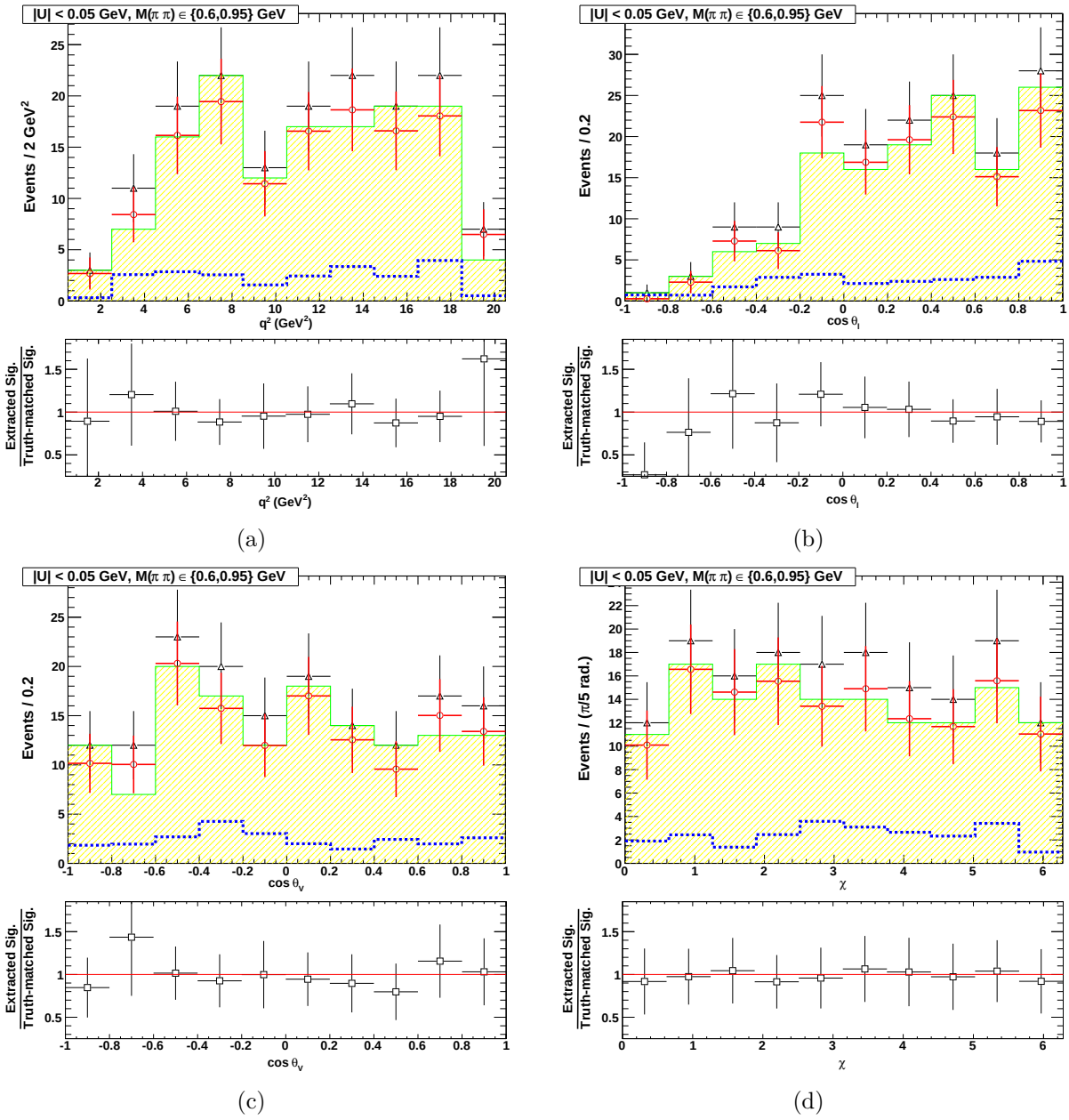

Figure 3.8: $B \to \rho^0 \ell \nu$ signal-background fit results for (a) q^2 and (b) $\cos\theta_\ell$ (c) $\cos\theta_V$ and (d) χ. Here $\lambda_s = 0.95$, $\lambda_b = 0.7$ and $N_c = 50$.

3.3.8 Effect of keeping the PDF shapes fixed to the MC

As noted earlier, in our event-by-event signal-background separation fits, we use a preliminary fit to the MC to extract our start values. The MC datatset for these fits are sampled in a larger phase-space region than the actual Data, and they should strictly be taken as start values for Minuit. The motivation here is that, from truth-information in the MC, we have access to the individual signal and background shapes, and fitting to the separate components (instead of the total, as in the Data) stabilizes the start PDF shapes. The ρ case is also different from the other channels because of the 2-D fits in U and $M(\pi\pi)$, instead of a 1-D fit in just U.

However, we note that the MC shapes are approximations of the final fit results and event-by-event, the two may or may not be an exact match. Fig. 3.9 demonstrates the fact that the start values could generically not be optimal for the final fit results. Figs. 3.9a-c show the fit results corresponding to the shape fixed to the preliminary fit to MC. Figs. 3.9d-f show the results with allowance for the shape parameters to float as $\lambda_s = \lambda_b = 0.7$. The true yield is 28, extracted yield for the 1st case is 40 ± 11 and 25.5 ± 8.4 for the latter.

Figs. 3.10 and 3.11 show the cumulative signal-background separation qualities for $\lambda_s = \lambda_b = 1$ and $N_c = 50$. Overall, we found that in the region $|U| < 0.05$ GeV and $M(\pi\pi) \in [0.6, 0.95]$ GeV, the yields for $\lambda_s = 0.95$, $\lambda_b = 0.7$ and $\lambda_s = \lambda_b = 1$ were ~ 134 and ~ 138 respectively, compared to the true yield of 137. While this points to consistency among different choices of the amoung of freedom we want to allow in the pdf shapes, we point out that the "mock Data" is a subset of the MC. Therefore, in our final fits to the Data, different choices of the λ variables must be studied to ensure that we are not introducing any bias towards the composition present in the MC.

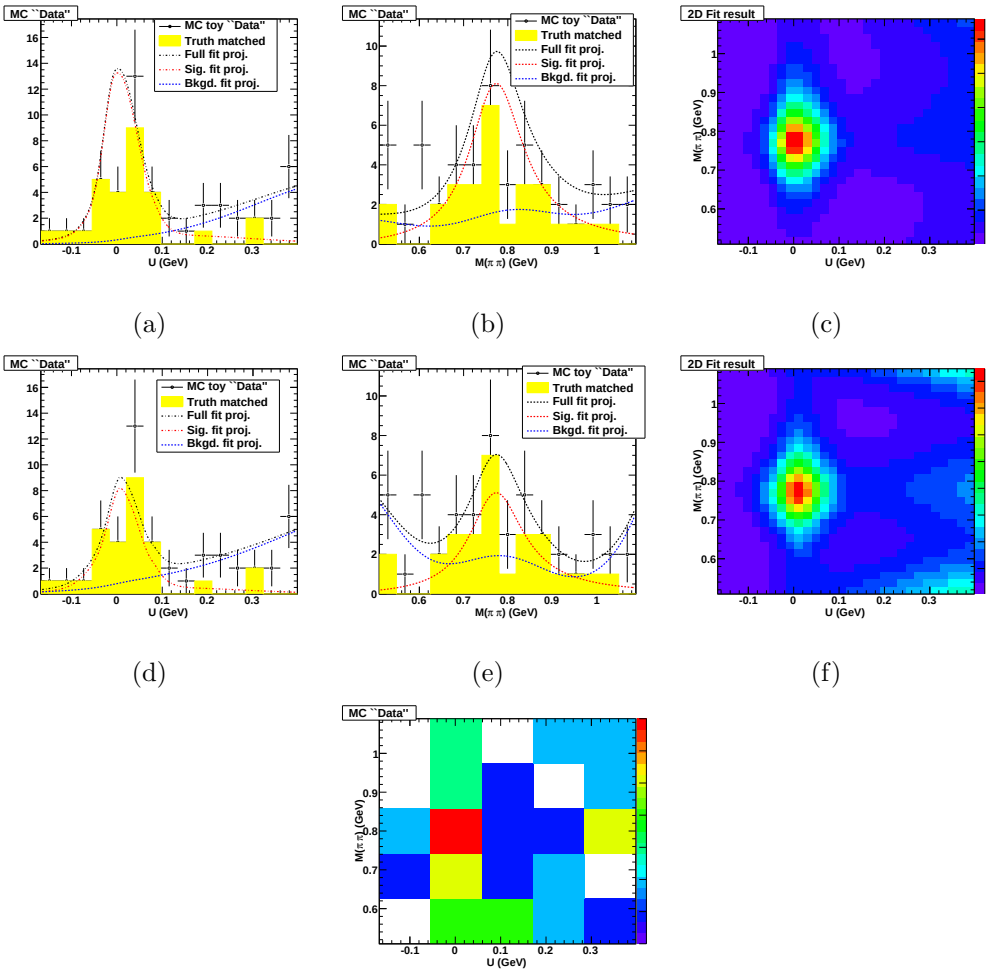

Figure 3.9: Effect of fixing signal shapes to MC vs. $\lambda_s = \lambda_b = 0.7$. The true yield is 28, extracted yield for the 1st case is 40 ± 11 and for the latter, 25.5 ± 8.4. Subfigures a, b, c pertain to the fixed shape to MC and d, e, f pertain to $\lambda_s = \lambda_b = 0.7$. a and d are the projections on U, while b and d are projections on $M(\pi\pi)$. c and f are the 2-dim fit results in U-$M(\pi\pi)$. g is the 2-d distribution in the Data.

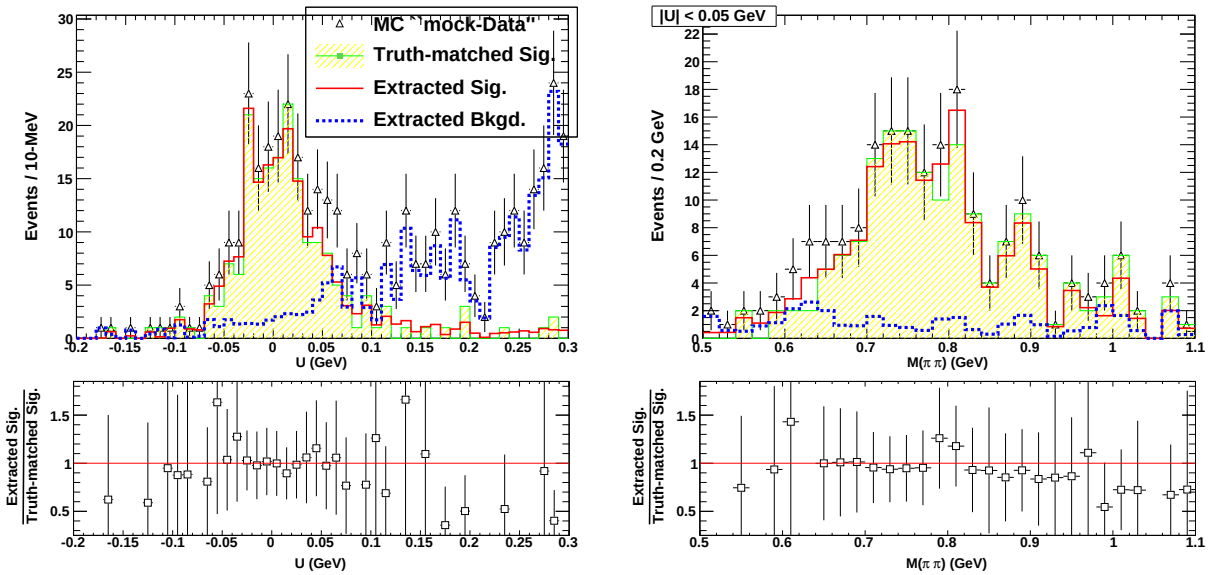

(a) (b)

Figure 3.10: $B \to \rho^0 \ell \nu$ signal-background fit results for (a) U and (b) $M(\pi\pi)$. Here $\lambda_s = \lambda_b = 1$ and $N_c = 50$.

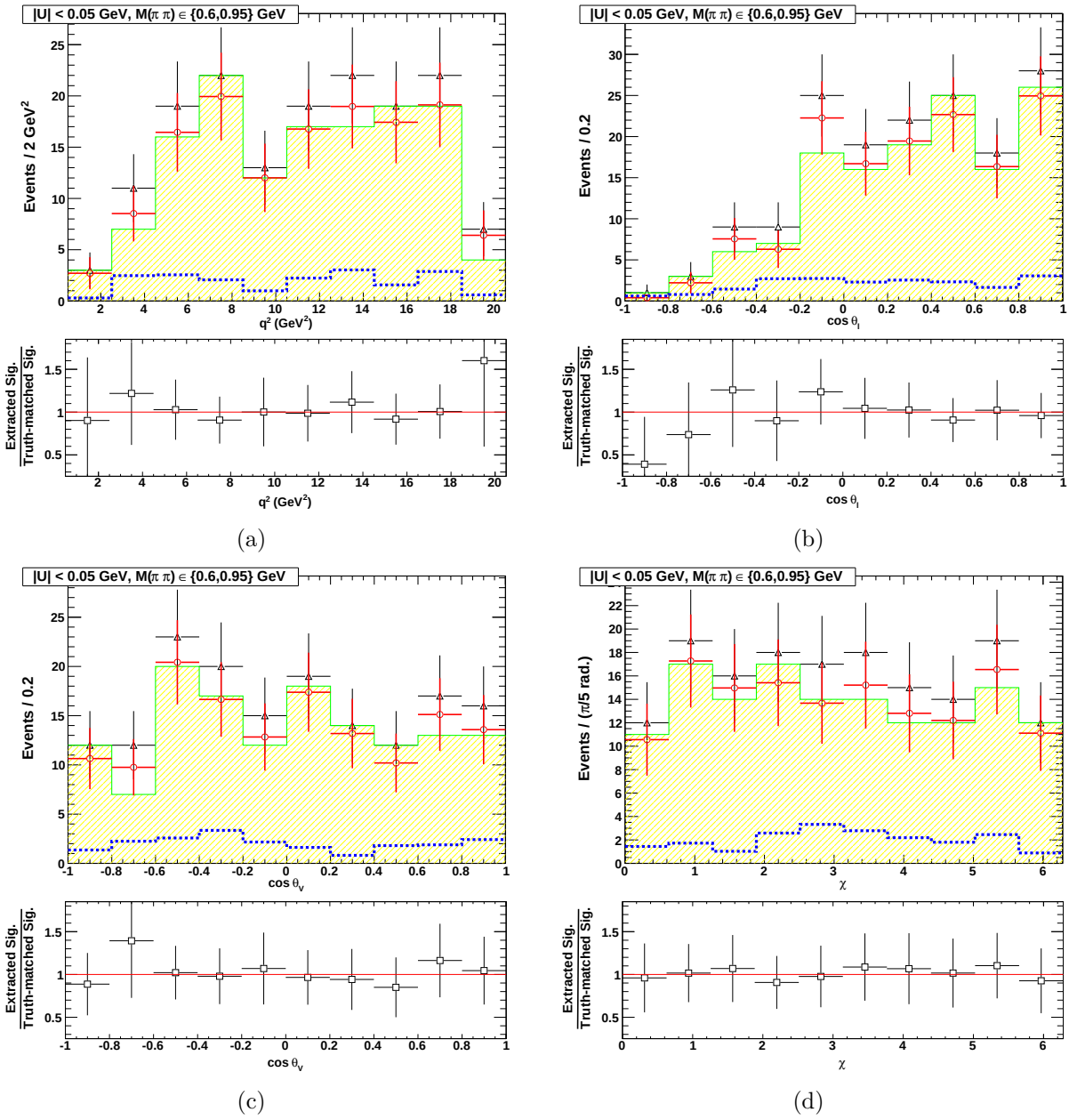

Figure 3.11: $B \to \rho^0 \ell\nu$ signal-background fit results for (a) q^2 and (b) $\cos\theta_\ell$ (c) $\cos\theta_V$ and (d) χ. Here $\lambda_s = \lambda_b = 1$ and $N_c = 50$.

3.3.9 Effect of fits to signal-depleted samples

To check the validity of our procedure in "pockets" of phase-space which are signal-depleted, we apply our method with $\lambda_s = \lambda_b = 0.7$, $N_c = 50$ to a "mock Data" sample with the signal component completely removed. Fig. 3.12a shows the quality of signal-background separation – in red is the extracted signal and in blue is the background. Clearly, in the tail

region, some amount of signal is being assigned, where there is none. In this region, away from the peaking regime, the signal and background pdf's do not have sufficient demarcation power. Especially for the e case, the signal pdf too has a long tail. That is, the fit can not tell what is signal and what is background – it just finds the best sum that describes the data. Along with the inherent systemtics associated with PHOTOS, we trim out the tail region after the signal-background separation is completed. Note that we have also placed a $M(\pi\pi) \in \{0.6, 0.95\}$ GeV cut here.

Focussing on the signal region, viz. $|U| < 0.05$ GeV, we find ~ 9 events being attributed to as signal, out of ~ 19 events. In fact, almost all of the assigned signal component is in the μ channel. Fig. 3.12b shows the projections on to $M(\pi\pi)$ in the signal region $|U| < 0.05$ GeV. The problem emanates from the fact that there is no signal peak in U, but there is one in $M(\pi\pi)$ (true ρ and $\pi \leftrightarrow \mu$ misid). Therefore, in the 2-d fit, there is less discrimination between the signal and background pdf's for the fitter. We make a general comment here that our method is reliant on the fact that the signal shape must be distinct from the background. Without a signal peak in U, the distinction is blurred. Therefore highly signal-depleted regions are not optimal for the method in hand and this problem specifically pertains to the $\rho\mu\nu$ sample. The only way to solve this problem is to bin finely enough in $M(\pi\pi)$ (or at least place a very tight cut around $M(\pi\pi) = 0.77$ GeV) and fit in just U. We note here that initial attempts at 1-d fits in U with a wide $M(\pi\pi)$ window resulted in poor expected/truth-matched comparisons in the variable $M(\pi\pi)$. This was in fact the primary motivation for switching to 2-d fits.

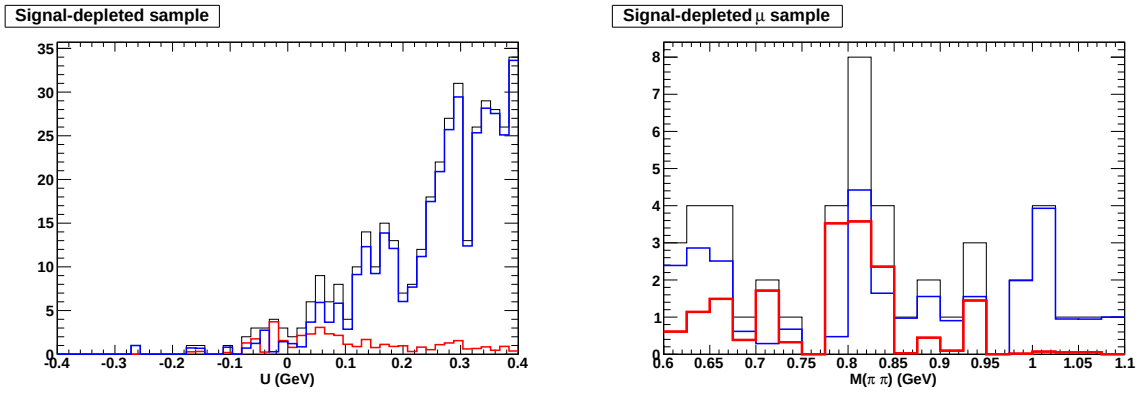

(a) (b)

Figure 3.12: $B \to \rho^0 \ell\nu$ signal-background fit results for a "mock Data" sample that contains no signal. In red is the extracted signal and in blue is the background. (a) is for both e/μ samples, while (b) shows the peaking $M(\pi\pi)$ component in the μ sample.

3.3.10 Systematic uncertainties on the yield extractions

For estimating systematic uncertainties, one typically performs toy studies with data samples generated from PDF's taken from the MC. However, in the case of the present analysis, the

corresponding PDF's would need to be in 7 dimensions, viz., U, $M(\pi,\pi)$, q^2, $\cos\theta_B$, $\cos\theta_\ell$, $\cos\theta_V$, and χ. Since we do not have enough MC statistics to form reliable PDF's in so many dimensions, we create bootstrap toys where we sample from the same set of MC events in a probabilistic manner. We use 100 toy samples in this study. Since we have only $10\times$ generic $B\overline{B}$ and $c\bar{c}$ MC, and $2\times$ uds MC, there is a large amount of overlap among the toy samples. In each sample, we pseudorandomly accept or reject a MC event according to whether its lumi-weight is higher or lower, respectively, than a generated random number between 0 and 1. The lumi-weights are the fractional weight-factors that normlize each component in the generic $B\overline{B}$ + continuum MC, to the full Data luminosity.

We then repeat the signal-background separation fits to each toy sample to extract the corresponding set of Q-values. The pull on the yields in the s^{th} toy set is

$$g_s = \frac{\mathcal{Y}_s^Q - \mathcal{Y}_s^{TM}}{\sigma_s^Q}, \tag{3.19}$$

where $\mathcal{Y}^{TM}$ is the true yield, $\mathcal{Y}^Q$ is the extracted yield:

$$\mathcal{Y}^Q = \sum Q_i, \tag{3.20}$$

and the estimated statistical error on the yield is

$$\sigma^Q = \sqrt{\sum Q_i + \left(\sum \sigma_i^Q\right)^2}. \tag{3.21}$$

Note that, in the last equation we have made a conservative coherent summation of the Q-value errors (σ_i^Q) in the entire sample. Fig. 3.13 shows the relative effect of the σ_i^Q's. Compared to the naive statistical errors $\sqrt{\mathcal{Y}^Q}$, the effect is small.

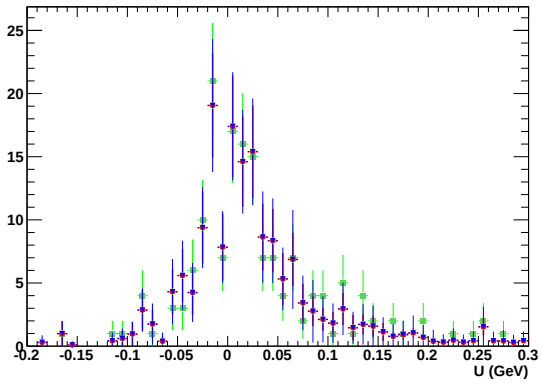

Figure 3.13: The green points are the true yields, the Q-value extracted yields are the red points (only the statistical errors) and blue (additional Q-value errors). The difference between the red and blue error bars are small.

As elsewhere, the e/μ samples show somewhat different characterestics and are studied independently. The present study is based on a choice of $N_c = 100$, $\lambda_s = \lambda_b = 0.7$.

Fig. 3.14a shows the pull distributions for the e samples, with the additional cuts $|U| < 0.1$ GeV and $M(\pi\pi) \in \{0.6, 0.95\}$ GeV to select out the signal region. The two prominent characterestics are bear out are that the extracted yields are systematically lower than the true yields. Since the σ is significantly smaller than unity, the errors also look to be over-estimated. The Q-value errors are correlated with the statistical uncertainties since a larger data sample gives a more stable fit. Still, it might be prudent to retain the Q-value errors in the overal statistical errors, as a conservative estimation. Fig. 3.14b shows the cumulative (summed over all kinematic variables) ratio between the extracted and truth-matched yields. The mean deviation is of the order of 8% – we quote as our systematic uncertainty for the e case. Fig. 3.14c shows the same ratio in bins of q^2, averaged over all 100 toys. We note that many of the bins have only a few events, since our overall yield is $\mathcal{O}(60)$. Even if we consider ~ 10 bins, the percentage errors scale like $1/\sqrt{6} \sim 40\%$.

Fig. 3.16 shows the aforementioned plots for the μ sample. From Fig. 3.16c, in regions of "reasonable" statistics, we find no significant deviation from unity in the ratio between teh extracted and true yields. Therefore, we do not include any additional uncertainty for the μ case. To quote a conservative estimate, we retain the coherently added Q-value errors in our final results. We also studied different cuts on $|U|$ for the μ, and the conclusions were not found to change.

Figs. 3.18, 3.19, 3.20 and 3.21 show the same for $\lambda_s = \lambda_b = 1$.

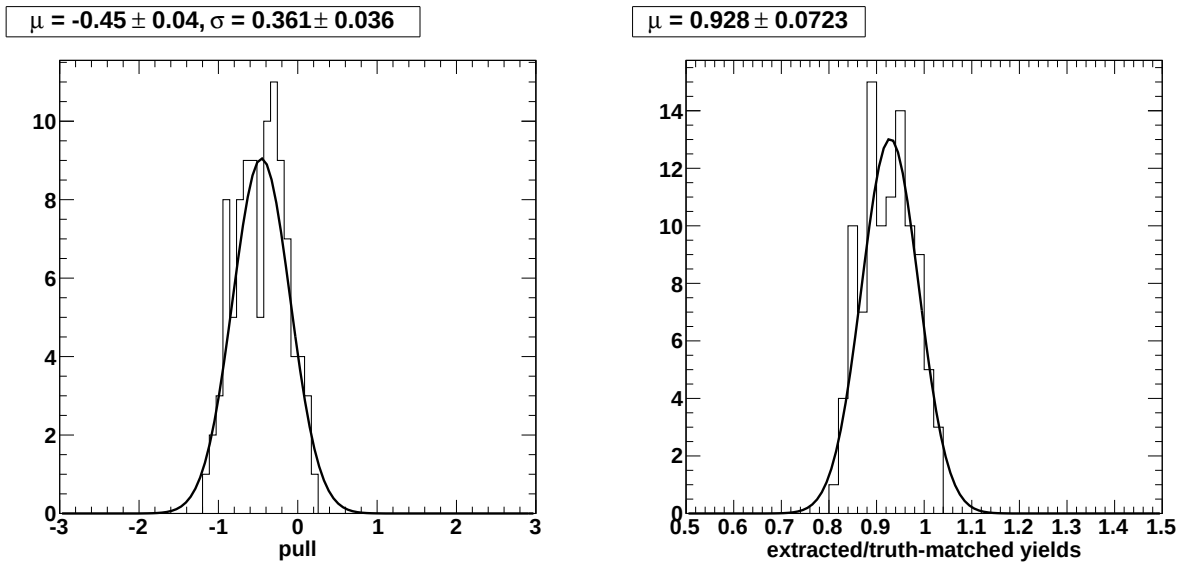

(a)

(b)

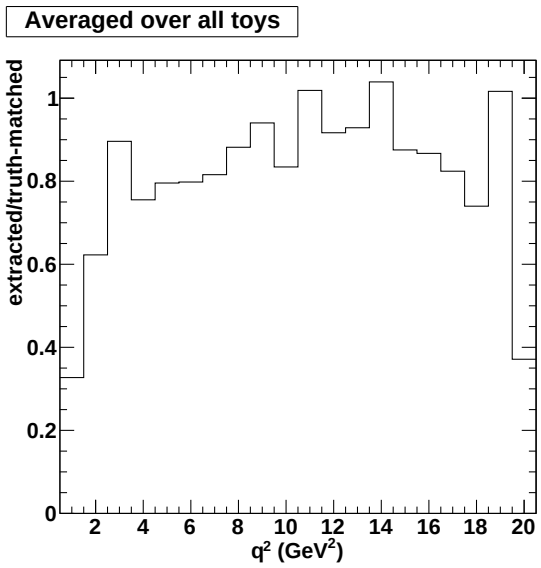

(c)

Figure 3.14: $B \to \rho^0 e\nu$ signal-background fit systematics from 100 toys. We compare the ratio between the extracted yields and the true yields: (a) pulls (b) overall ratio (c) ratio in q^2 bins, averaged over all toys.

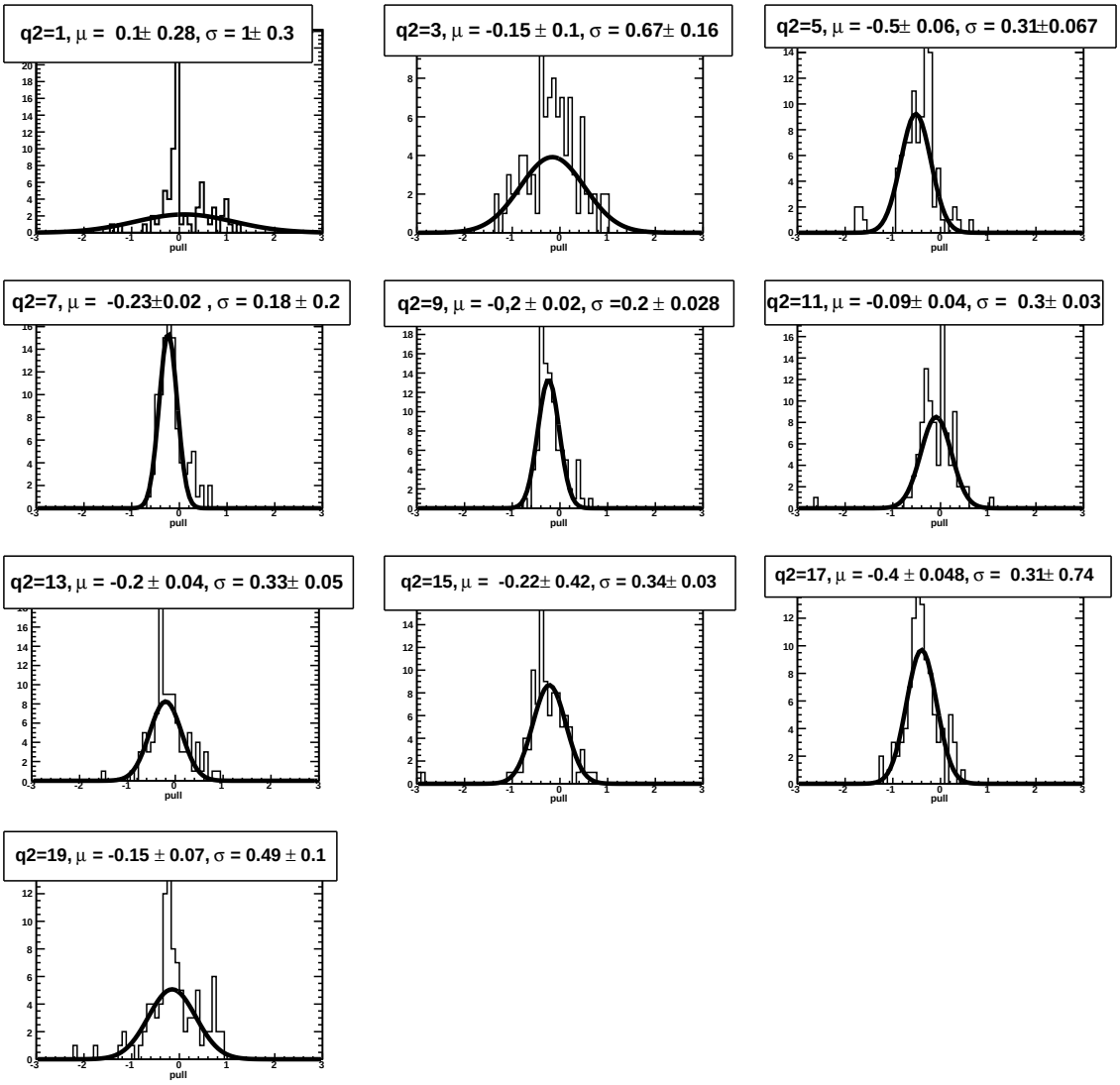

Figure 3.15: $B \to \rho^0 e\nu$ signal-background fit pulls from 100 toys in individual q^2 bins.

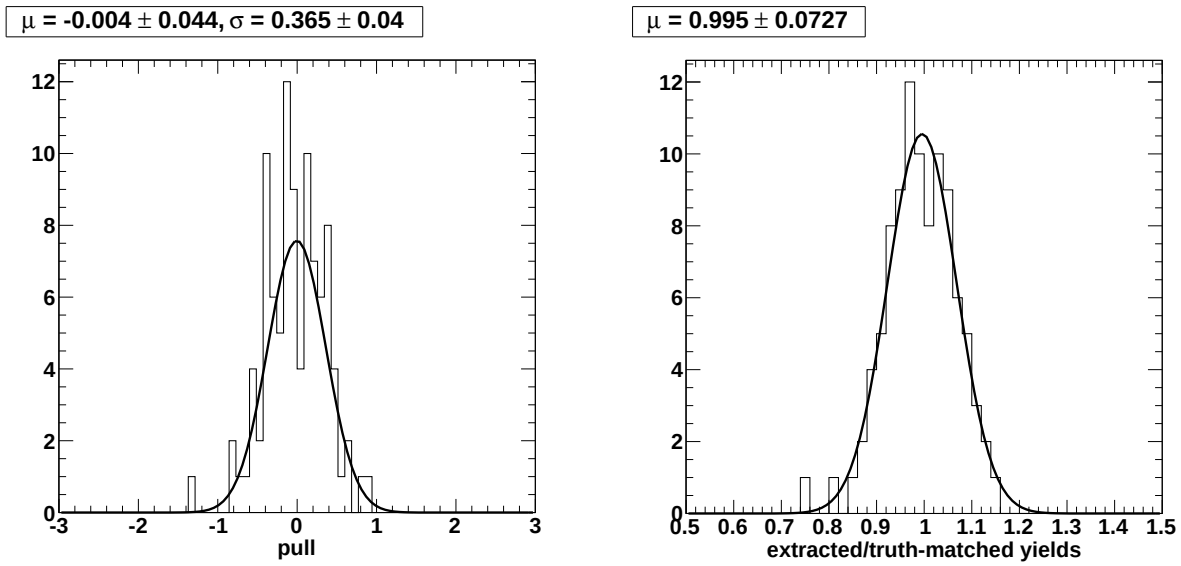

(a)

(b)

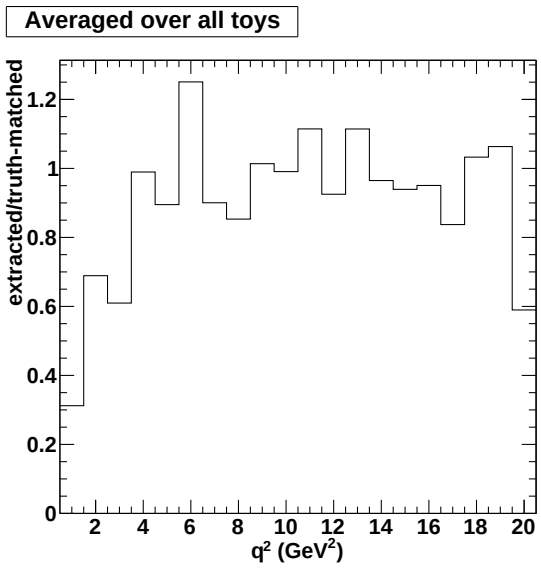

(c)

Figure 3.16: $B \to \rho^0 \mu\nu$ signal-background fit systematics from 100 toys. We compare the ratio between the extracted yields and the true yields: (a) pulls (b) overall ratio (c) ratio in q^2 bins, averaged over all toys.

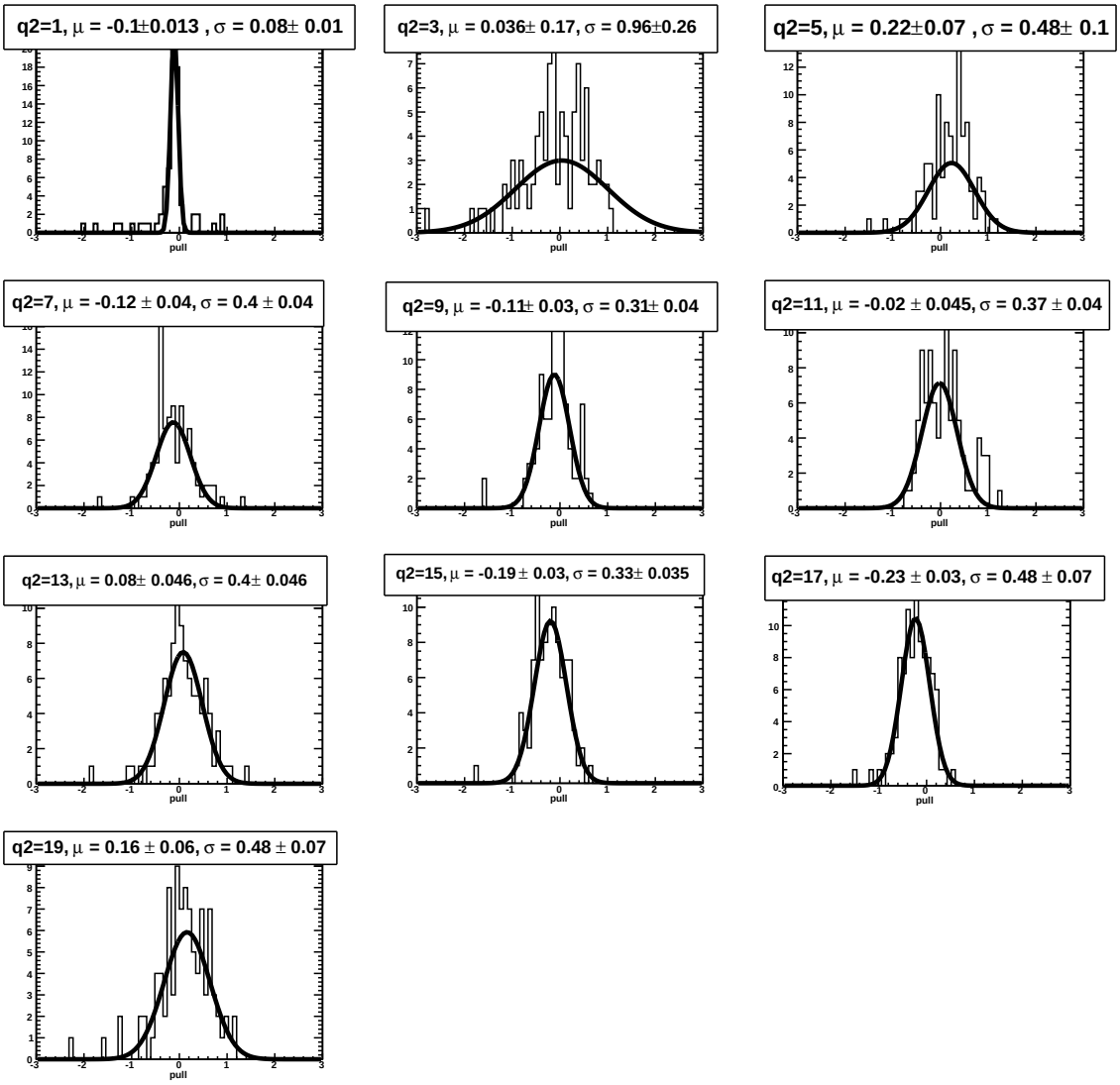

Figure 3.17: $B \to \rho^0 \mu\nu$ signal-background fit pulls from 100 toys in individual q^2 bins.

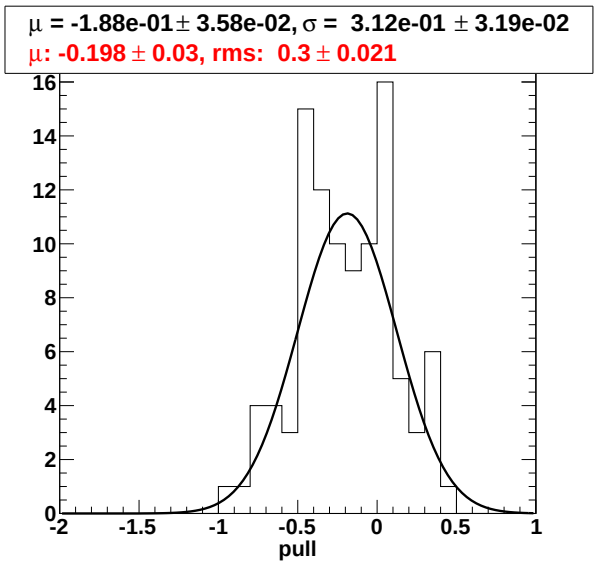

(a)

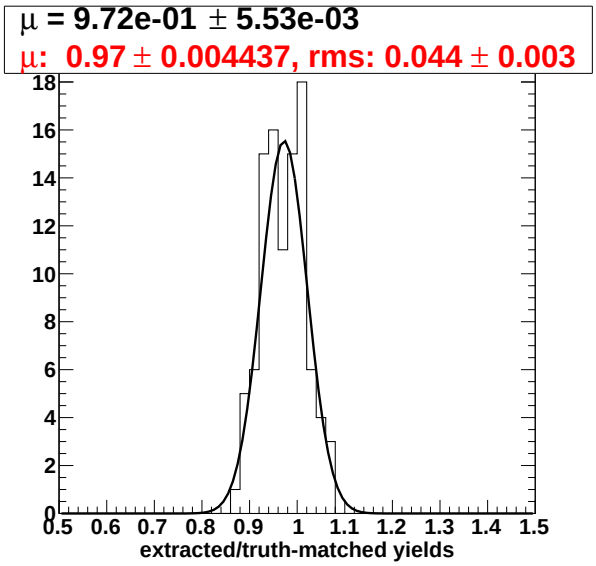

(b)

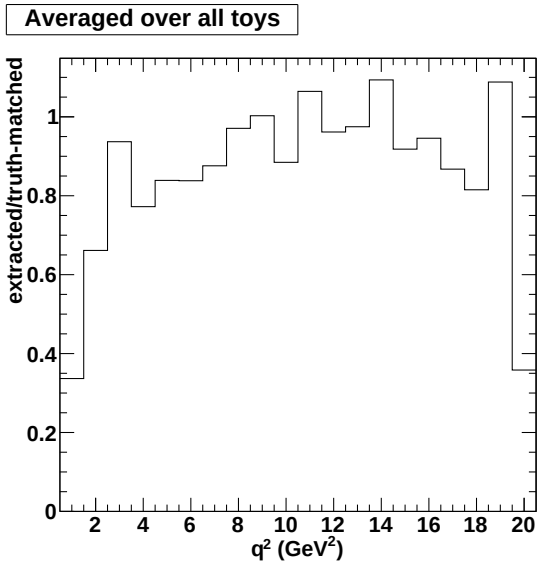

(c)

Figure 3.18: $B \to \rho^0 e\nu$ signal-background fit systematics from 100 toys. We compare the ratio between the extracted yields and the true yields: (a) pulls (b) overall ratio (c) ratio in q^2 bins, averaged over all toys. Here, $\lambda_b = \lambda_s = 1$.

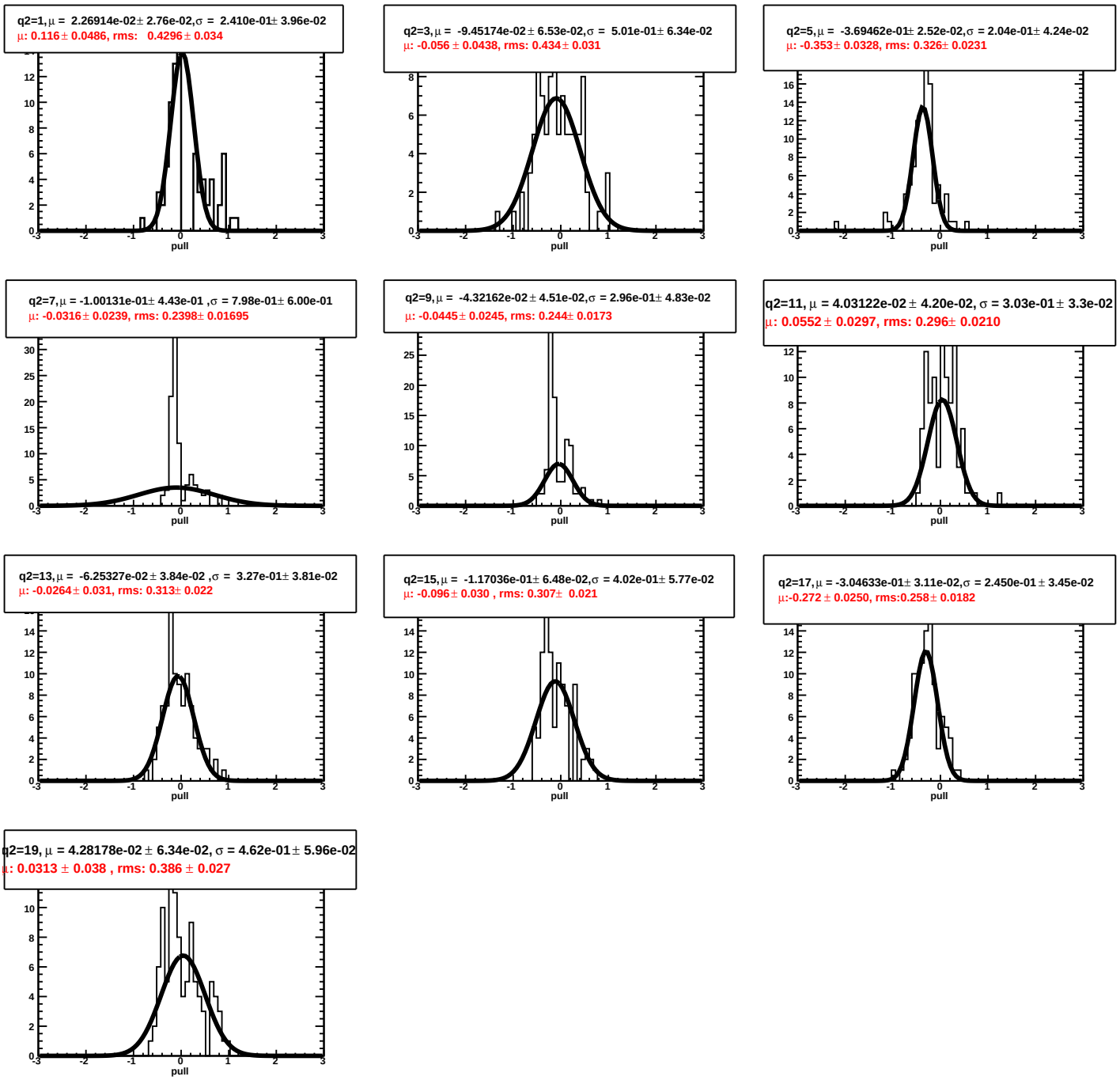

Figure 3.19: $B \to \rho^0 e\nu$ signal-background fit pulls from 100 toys in individual q^2 bins. Here, $\lambda_b = \lambda_s = 1$.

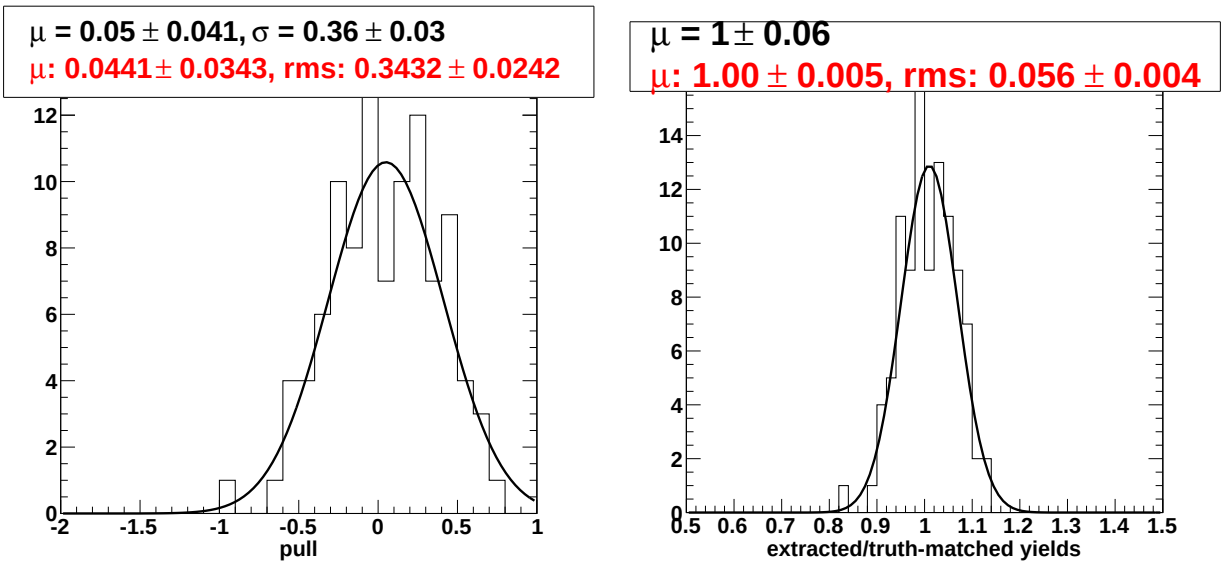

(a)

(b)

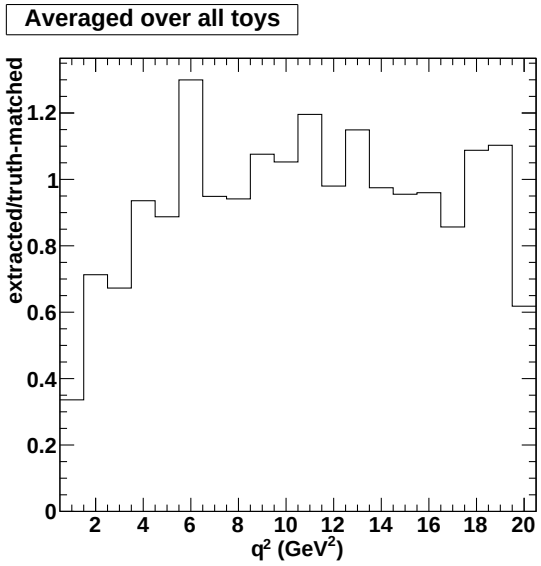

(c)

Figure 3.20: $B \to \rho^0 \mu\nu$ signal-background fit systematics from 100 toys. We compare the ratio between the extracted yields and the true yields: (a) pulls (b) overall ratio (c) ratio in q^2 bins, averaged over all toys. Here, $\lambda_b = \lambda_s = 1$

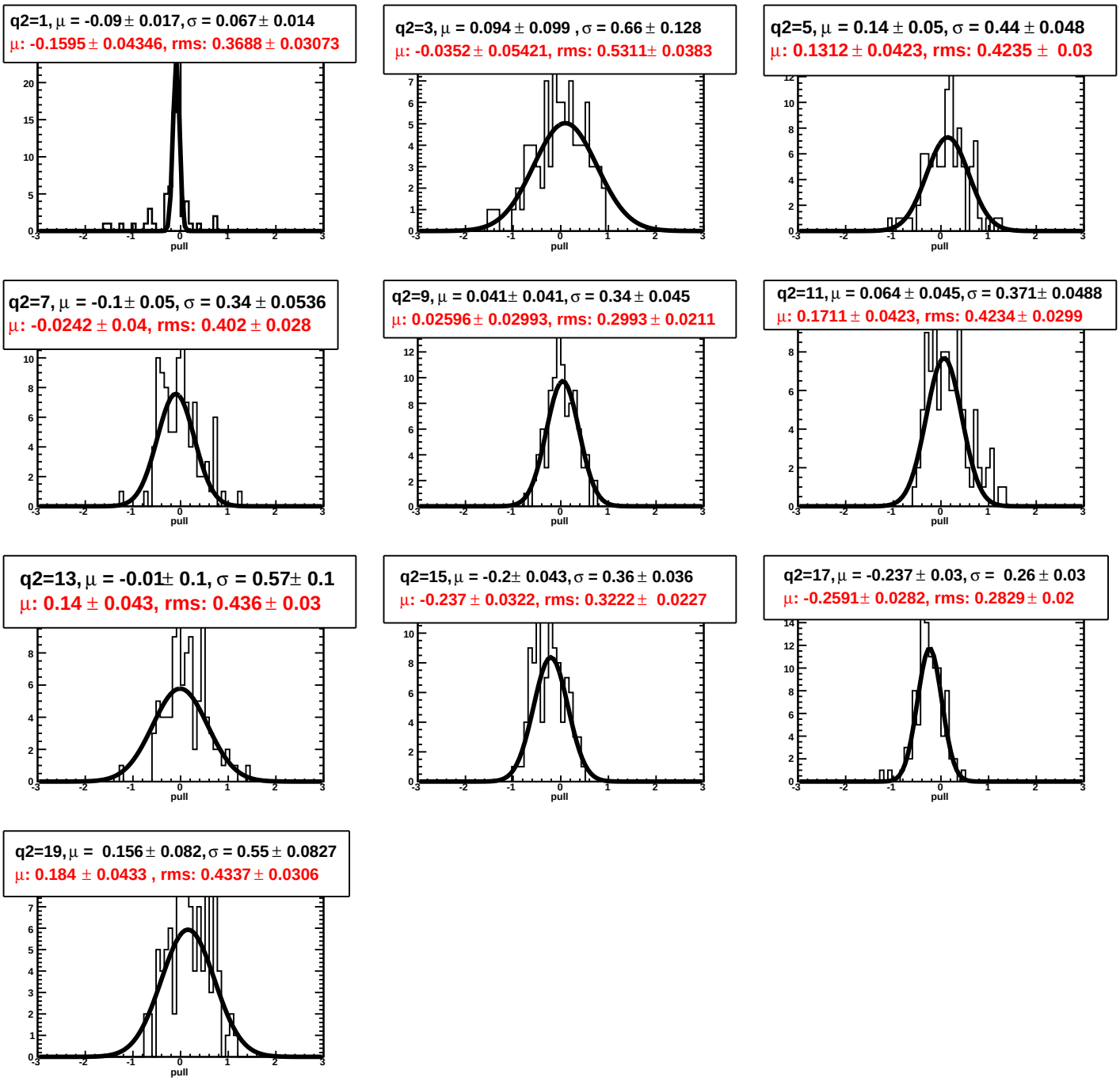

Figure 3.21: $B \to \rho^0 \mu\nu$ signal-background fit pulls from 100 toys in individual q^2 bins, $\lambda_b = \lambda_s = 1$.

3.4 1-D fits in U

In this section, we switch to using 1-D fits in the U variable with a $M(\pi\pi) \in [0.67, 0.87]$ GeV cut. Our signal pdf remains Eq. 3.13. As in the 2-D fits from the previous section, the signal pdf shape is taken from a fit to signal MC and the shapes of the low- and high-side "tails" (3rd and 4th bifurcated Gaussians in Eq. 3.13) are fixed from this fit. The background pdf is kept as a simple bifurcated Gaussian with the mean constrained to lie in $U > 50$ MeV, so that the background shape is disjoint from the signal pdf shape (in other words, this ensures that the background does not peak at $U = 0$). The fit steps remain as outlined in Sec. 3.3.5, except that the fits are 1-D binned fits in U. The initial *start values* for both the signal and background pdf's are taken from the MC. The signal and background normalizations are always kept unrestricted and floating. For the shape parameters, for a given value x_0, extracted from fits to the MC, we constrain the range in the final fit to the Data between λx_0 and x_0/λ, where $\lambda \leq 1$ denotes how strongly we constrain the shapes to the MC. We consider different values of the λ parameter for the signal and background pdfs, λ_s and λ_b, respectively. In all, there are 14 fit parameters: s_1, μ_1, σ_1^L, σ_1^R, s_2, μ_2, σ_2^L, σ_2^R, s_3 and s_4 in Eq. 3.13 for the signal, and 4 parameters for the background bifurcated Gaussian.

For systematic studies, we repeat the entire fit procedure for $\{\lambda_b = 0.7, \lambda_s = 0.95\}$, $\{\lambda_b = 0.9, \lambda_s = 0.9\}$, $\{\lambda_b = 1, \lambda_s = 1\}$, and three different values of $N_c = \{50, 60, 70\}$. We also reiterate that the e and μ samples are processed separately, since they have very different signal and background characterestics. In the next two subsections, we point out some of the charaterestics of the different choices for λ_s and λ_b, employing 100 bootstrap toys constructed out of the entire available MC samples.

3.4.1 Case $\{\lambda_b = 1, \lambda_s = 1\}$

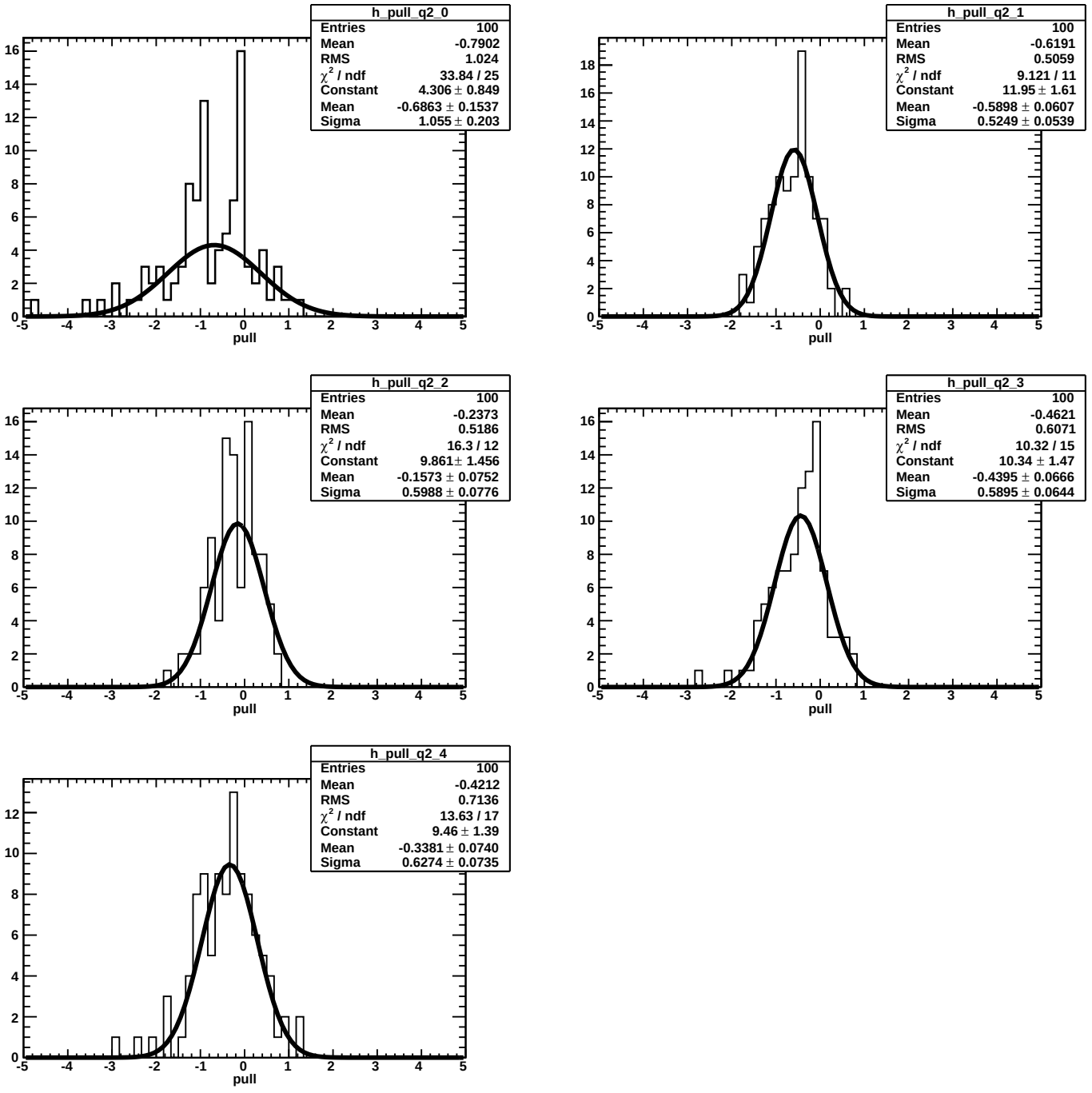

Figure 3.22: $B \to \rho^0 e\nu$ signal-background fit pulls from 100 toys in five 4-GeV^2-wide q^2 bins for $\lambda_b = \lambda_s = 1$ and 1-D fits in U.

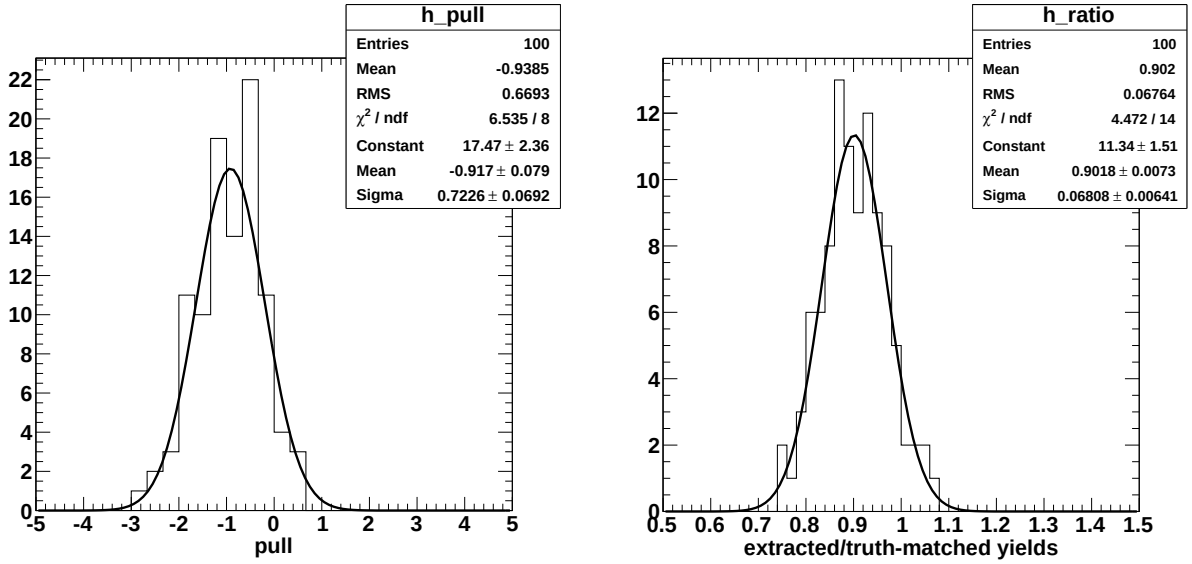

(a) (b)

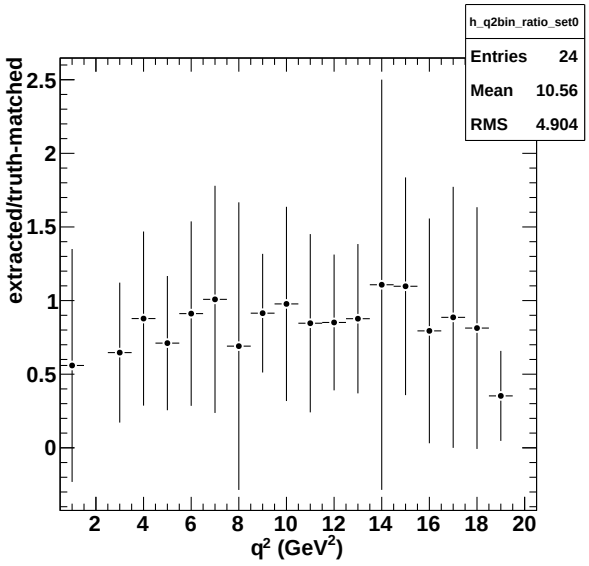

(c)

Figure 3.23: $B \to \rho^0 e\nu$, $\lambda_b = \lambda_s = 1$: (a) pulls from 100 toys (over all q^2 bins) (b) ratio between extracted and truth-matched yields from 100 toys (over all q^2 bins) and (c) ratio between extracted and truth-matched yields in twenty 1-GeV^2-wide q^2 bins for one particular toy sample.

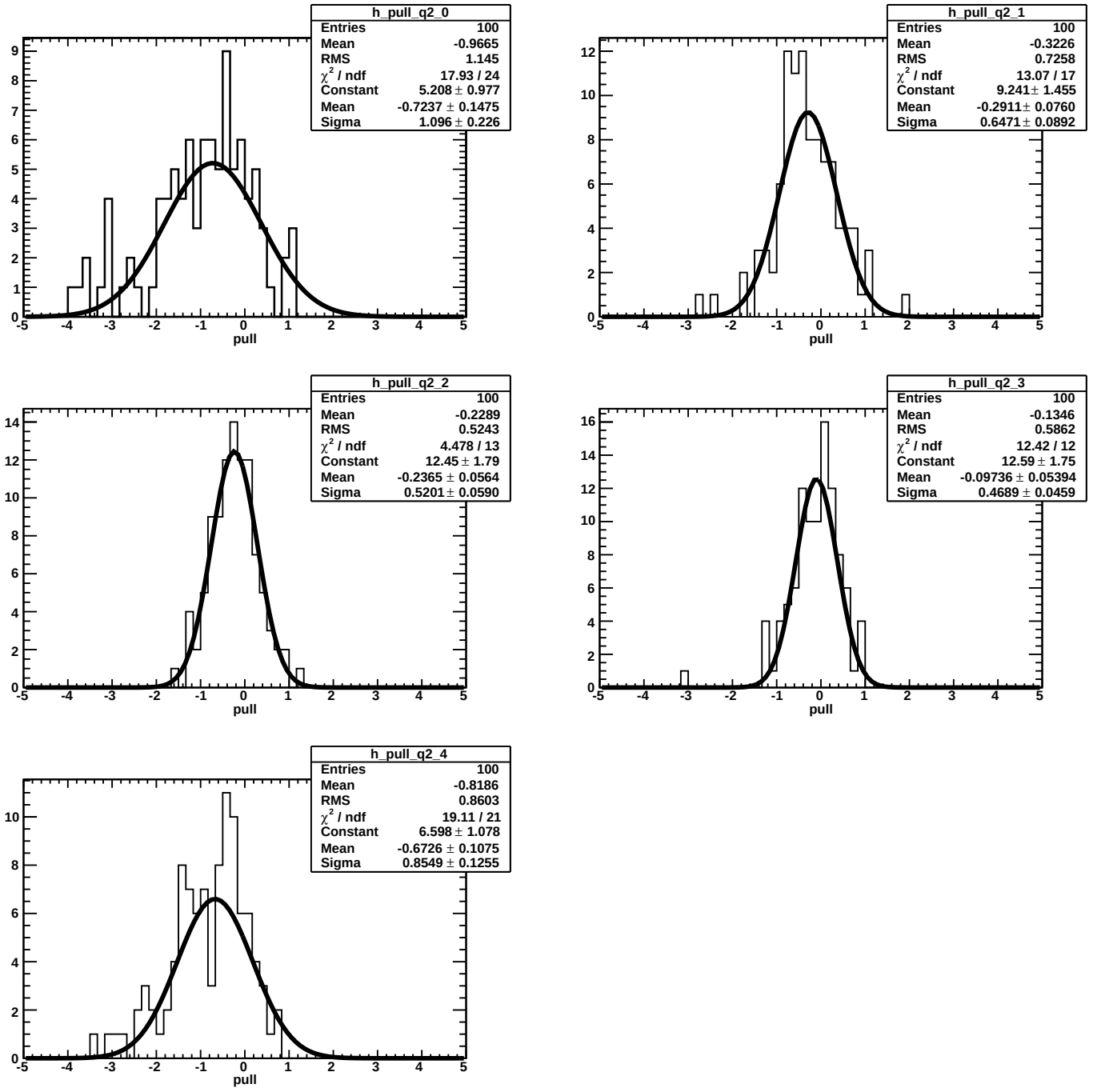

Figure 3.24: $B \to \rho^0 \mu\nu$ signal-background fit pulls from 100 toys in five 4-GeV^2-wide q^2 bins for $\lambda_b = \lambda_s = 1$ and 1-D fits in U.

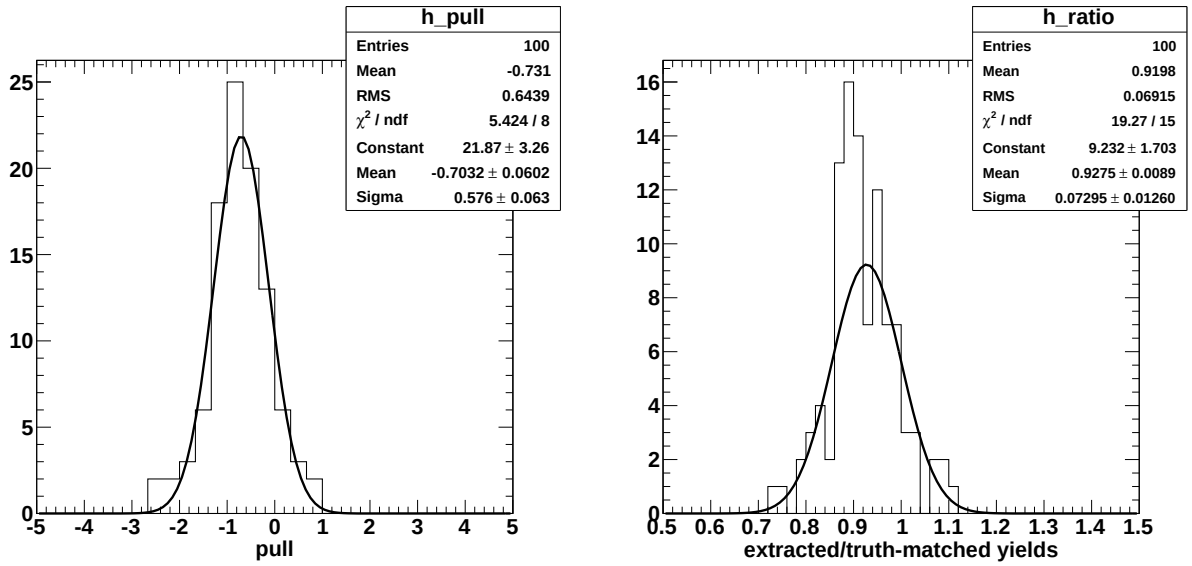

(a)

(b)

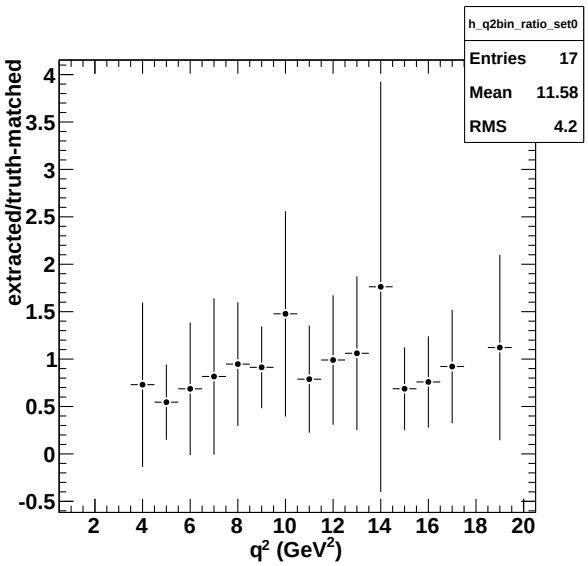

(c)

Figure 3.25: $B \to \rho^0 \mu\nu$, $\lambda_b = \lambda_s = 1$: (a) pulls from 100 toys (over all q^2 bins) (b) ratio between extracted and truth-matched yields from 100 toys (over all q^2 bins) and (c) ratio between extracted and truth-matched yields in twenty 1-GeV^2-wide q^2 bins for one particular toy sample.

3.4.2 Case $\{\lambda_b = 0.7, \lambda_s = 0.95\}$

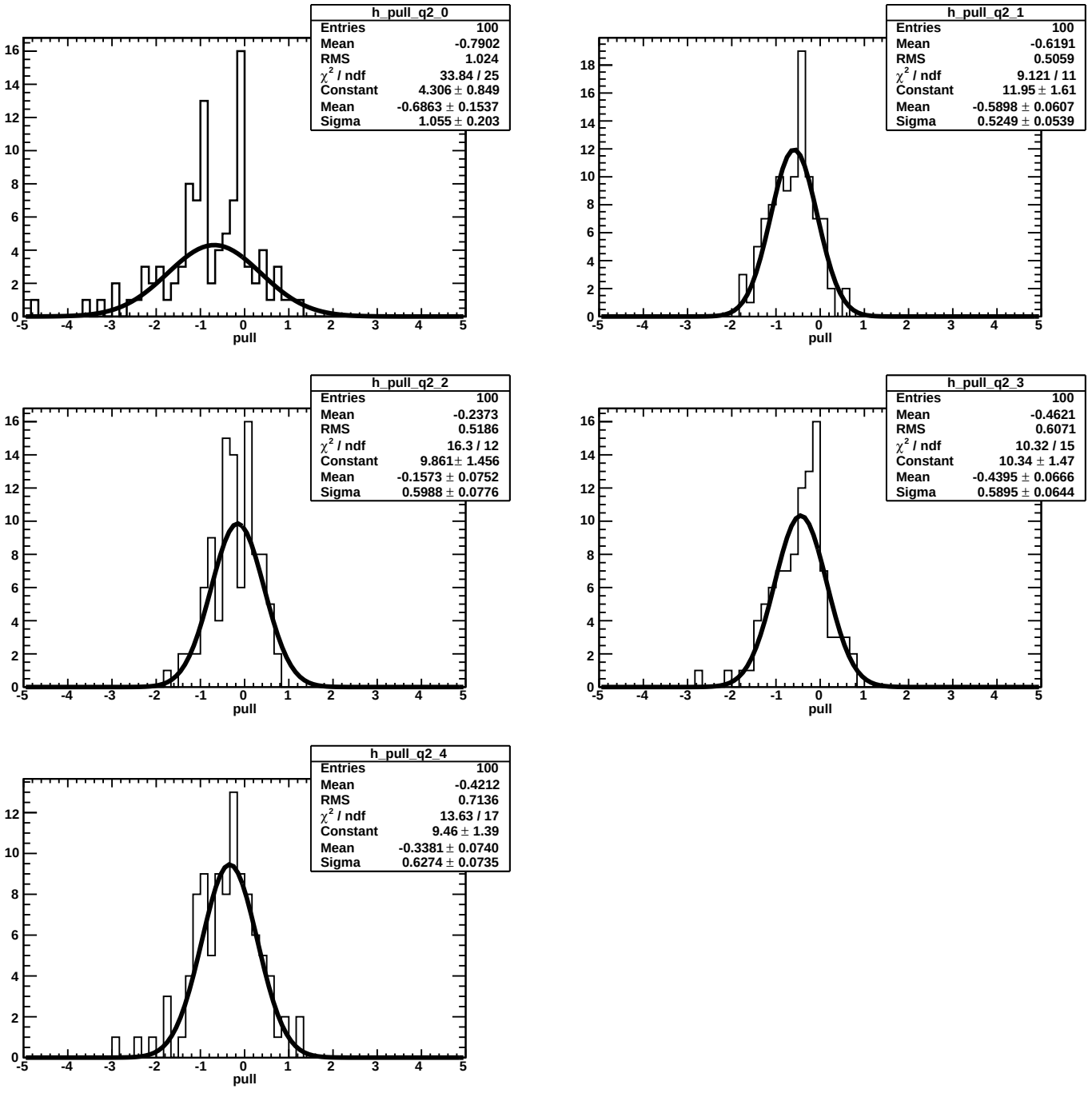

Figure 3.26: $B \to \rho^0 e\nu$ signal-background fit pulls from 100 toys in five 4-GeV^2-wide q^2 bins for $\lambda_b = 0.7$, $\lambda_s = 0.95$ and 1-D fits in U.

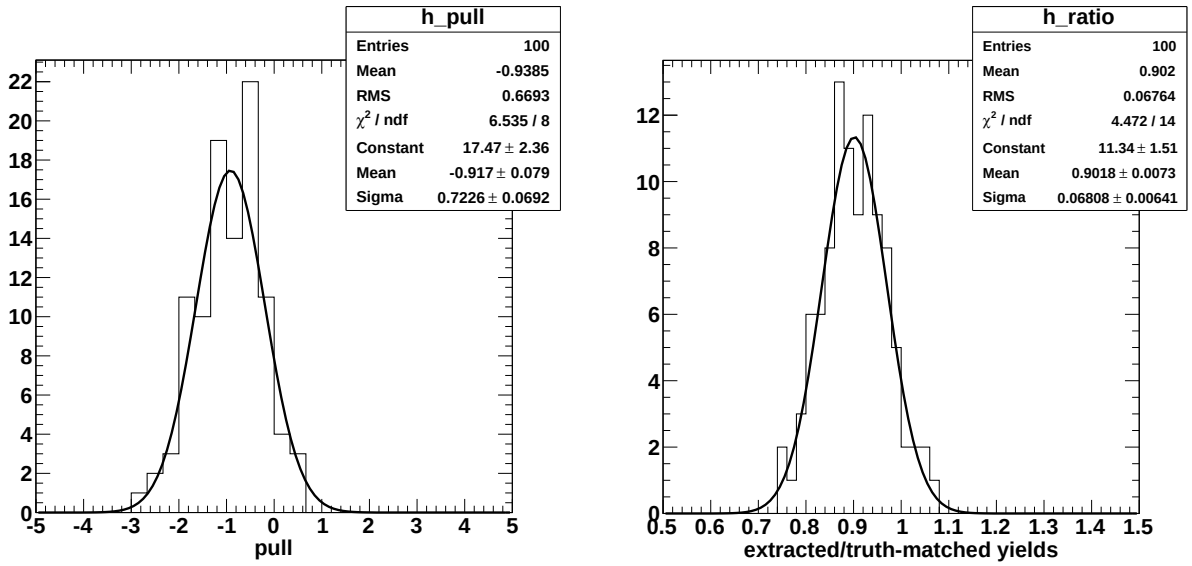

(a)

(b)

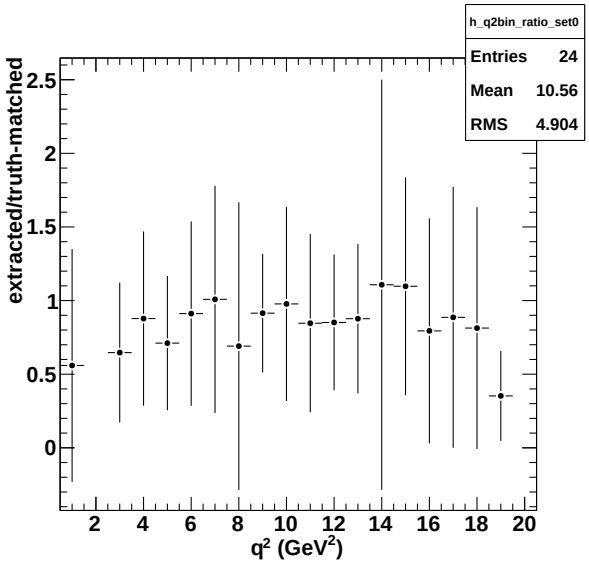

(c)

Figure 3.27: $B \to \rho^0 e\nu$, $\lambda_b = 0.7$, $\lambda_s = 0.95$: (a) pulls from 100 toys (over all q^2 bins) (b) ratio between extracted and truth-matched yields from 100 toys (over all q^2 bins) and (c) ratio between extracted and truth-matched yields in twenty 1-GeV^2-wide q^2 bins for one particular toy sample.

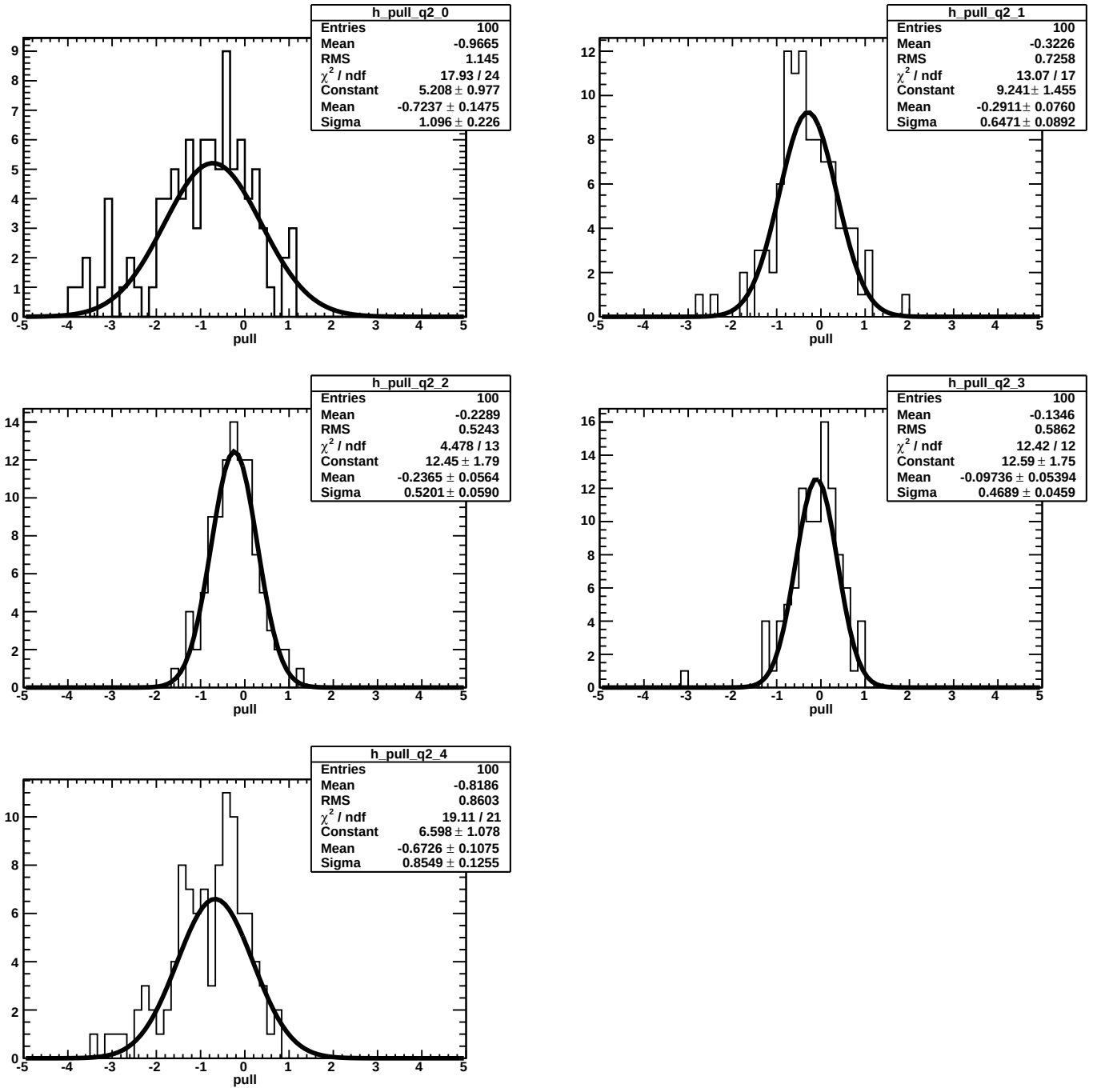

Figure 3.28: $B \to \rho^0 \mu\nu$ signal-background fit pulls from 100 toys in five 4-GeV^2-wide q^2 bins for $\lambda_b = 0.7$, $\lambda_s = 0.95$ and 1-D fits in U.

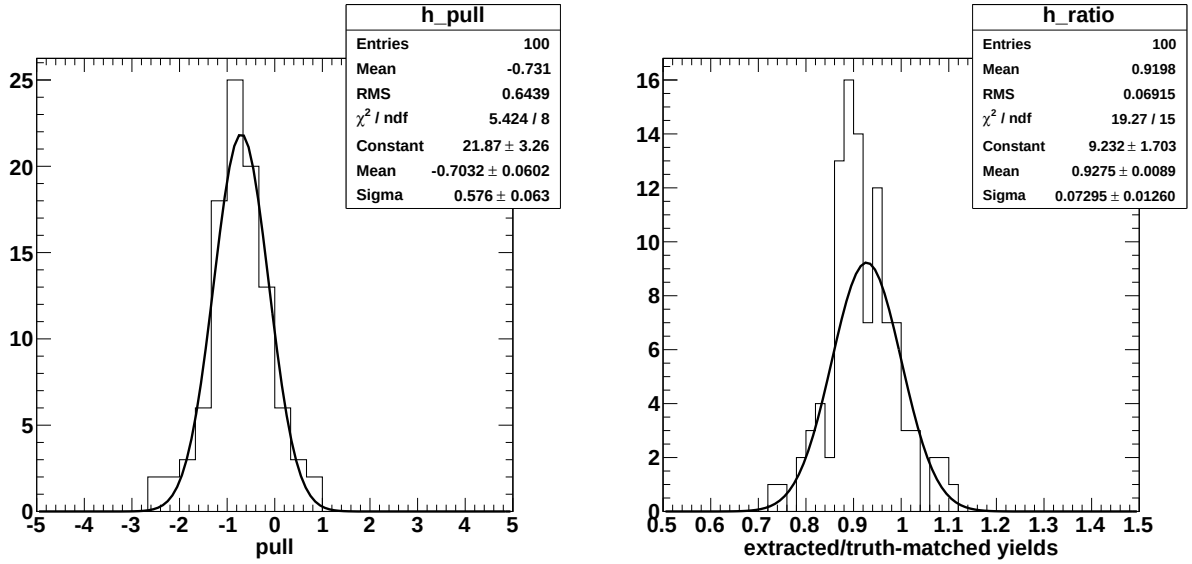

(a)

(b)

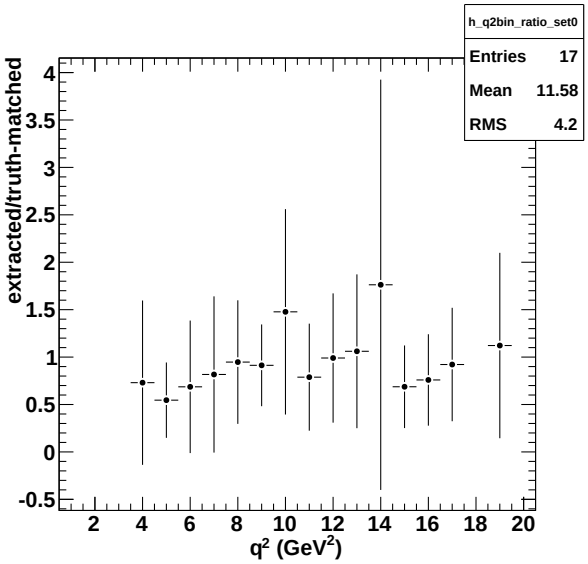

(c)

Figure 3.29: $B \to \rho^0 \mu\nu$, $\lambda_b = 0.7$, $\lambda_s = 0.95$: (a) pulls from 100 toys (over all q^2 bins) (b) ratio between extracted and truth-matched yields from 100 toys (over all q^2 bins) and (c) ratio between extracted and truth-matched yields in twenty 1-GeV^2-wide q^2 bins for one particular toy sample.

3.5 Comparisons between 1- and 2-D fit results

The 1-D and 2-D fits to extract the Q-values, as described above, follow very different procedures, and therefore involve different systematics. The 1-D fits are binned χ^2 fits with 14 parameters and a simplified setup, while the 2-D fits are unbinned ML fits with 28 parameters, that cater to the $M(\pi\pi)$ lineshape as well. In our final angular fits to extract the form-factor properties, we repeat the entire angular fit procedure for both 1- and 2-D fits, the three different sets of $\{\lambda_s, \lambda_b\}$ that quantify dependence on the MC pdf shapes and different values of the closest neighbor volume N_c. We note that Ref. [38] for previous CLEO analyses also mentions varying the phase-space volumes for estimating systematics from the usage of the overlapping event samples. Repeating the analysis for different values of N_c provides the equivalent check for our Q-value method.

Figs. 3.30a and 3.30b shows comparisons between truth-match and extracted backgrounds for the cases $\{\lambda_b = 0.7, \lambda_s = 0.95\}$, and $\{\lambda_b = 1, \lambda_s = 1\}$. The green curve shows the truth-matched background. The red(blue) curves are the extracted background from the 1D(2D) fits. The efficacy of plotting the background instead of the signal can be seen in focusing on the $U \approx 0$ region, where the difference between the extracted and truth-matched background is borne out. The difference is lower for $\{\lambda_b = 1, \lambda_s = 1\}$, where the pdf shapes are fixed to the MC. However, it is important to keep the $\{\lambda_b = 0.7, \lambda_s = 0.95\}$ choices into reckoning as well, since this enters into our systematics on the pdf shapes. However, we also note the consistency between the 1- and 2-D fits.

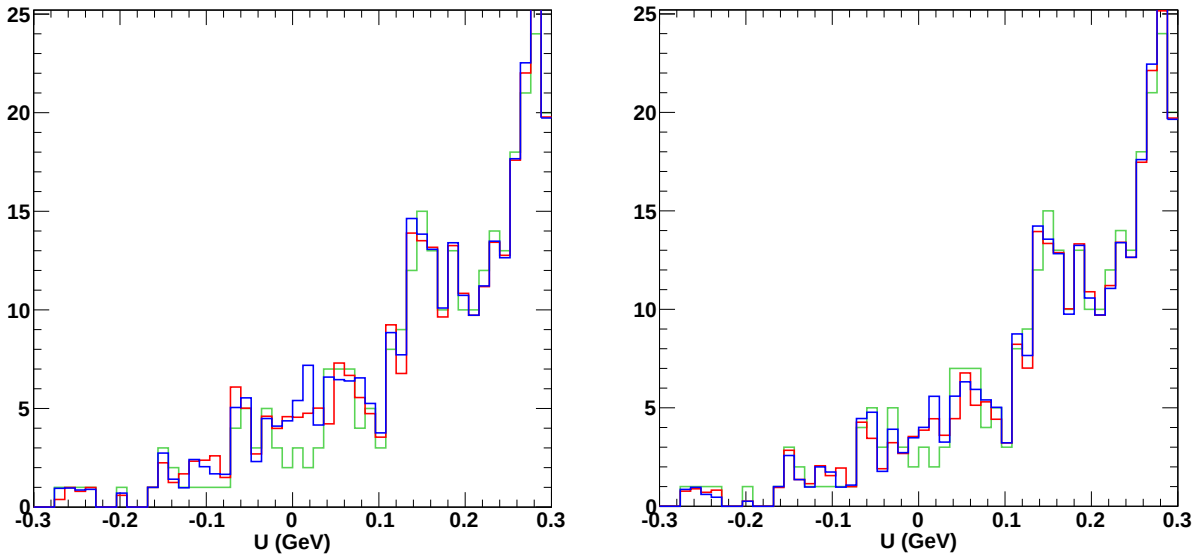

(a) (b)

Figure 3.30: Comparison between 1-D and 2-D fits for (a)$\{\lambda_b = 0.7, \lambda_s = 0.95\}$ (b) $\{\lambda_b = 1, \lambda_s = 1\}$. The green curve shows the truth-matched background. The red(blue) curves are the extracted background from the 1D(2D) fits.

Chapter 4

Angular fit

4.1 The minimization function

We mostly follow the formalism described in Chung [39]. The phase-space kinematic variables on which the differential rate depends, as $\phi = \{q^2, \chi, \cos\theta_\ell, \cos\theta_V\}$. The probability distribution function (pdf) for detecting an event within the phase-space element $[\phi, \phi + \Delta\phi]$ is

$$\mathcal{P}(\vec{x}, \phi) = \frac{\frac{dN}{d\phi}\eta(\phi)\Delta\phi}{\int \frac{dN}{d\phi}\eta(\phi)d\phi}, \tag{4.1}$$

where $\eta(\phi)$ is the (possibly) phase-space dependent detector efficiency or acceptance, and $\vec{x}$ denotes some set of parameters (the fit variables) that the differential rate might depend on. The normalization integral

$$\mathcal{N} = \int \frac{dN}{d\phi}\eta(\phi)d\phi \equiv \bar{N} = N_{data} \tag{4.2}$$

ensures that the pdf is properly normalized to unity, and we have assumed the estimated (from the fit) yield, $\bar{N}$, to be equal to the actual measured yield [1]. The likelihood function is then defined as

$$\mathcal{L}(\vec{x}) = \prod_{i=1}^{N_{data}} \mathcal{P}(\vec{x}, \phi_i). \tag{4.3}$$

The likelihood function is insensitive to the overall scale of the rate function, since this cancels out in the pdf definition.

[1] Strictly speaking, this should be equal to the average experimental yield upon repeating the experiment many times.

4.1.1 The minimum NLL's

The objective of the angular fit is to maximize the likelihood function that depends on the free fit parameters $\vec{x}$. Since the logarithm function is monotonic, maximizing the log of the likelihood is equivalent to maximizing the likelihood itself. Furthermore, it is convenient to minimize the negative log likelihood (NLL), instead of the maximizing the log likelihood itself. For the likelihood function in Eq. 4.3, the NLL reads

$$\begin{aligned} -\ln \mathcal{L}(\vec{x}) &= -\sum_{i=1}^{N_{data}} \ln \mathcal{P}(\vec{x}, \phi_i) \\ &\simeq N_{data} \ln [\mathcal{N}(\vec{x})] - \sum_{i=1}^{N_{data}} \ln \left[\frac{dN}{d\phi} \eta(\phi) \right]_i . \end{aligned} \tag{4.4}$$

4.1.2 Acceptance calculation using FLATQ2 signal Monte Carlo

In Eq. 4.4, as noted earlier, the η term denotes the detector acceptance. On a first approximation, this can be taken as flat in ϕ. However, in the general case, the acceptance might be dependent on ϕ and also on the physics model which changes the angular distributions. In this section we describe how to incorporate this effect in the fit using Monte Carlo. We employ the FLATQ2 generator, which generates $\Upsilon(4S) \to B_{\rm tag} B_{\rm sig}$ in a P-wave, with $B_{\rm tag}$ decaying generically. On the signal side, the $B_{\rm sig}$ goes to $\rho \ell \nu$ only, and the generator with a probability that is flat in ϕ.

The reason we need the Monte Carlo is that $\eta(\phi)$ is not known as an analytic function and η goes into the normalization integral. We make use of the approximation

$$\mathcal{N} = \int \frac{dN}{d\phi} \eta(\phi) d\phi \equiv \left(\int d\phi \right) \langle \frac{dN}{d\phi} \eta(\phi) \rangle_{avg.} \tag{4.5}$$

Now the average efficiency-incorporated rate term can be easily calculated using N_{MC}^{gen} MC events generated flat in ϕ as

$$\langle \frac{dN}{d\phi} \eta(\phi) \rangle_{avg.} = \sum_{i=1}^{N_{MC}^{gen}} \frac{dN}{d\phi} \eta(\phi) / N_{MC}^{gen} = \sum_{i=1}^{N_{MC}^{acc}} \frac{dN}{d\phi} / N_{MC}^{gen}. \tag{4.6}$$

In the last step we have incorporated the acceptance by summing over only the "accepted" MC events after passing through the detector simulator. That is, η is either 1 or 0 (the event is either recorded or missed).

Putting everything together and ignoring terms that are not variable in the fit, we can write

$$-\ln \mathcal{L}(\vec{x}) = N_{data} \times \ln \left[\sum_{i=1}^{N_{MC}^{acc}} \frac{dN}{d\phi} \right] - \sum_{i=1}^{N_{data}} \ln \left[\frac{dN}{d\phi} \right]_i \tag{4.7}$$

$$\tag{4.8}$$

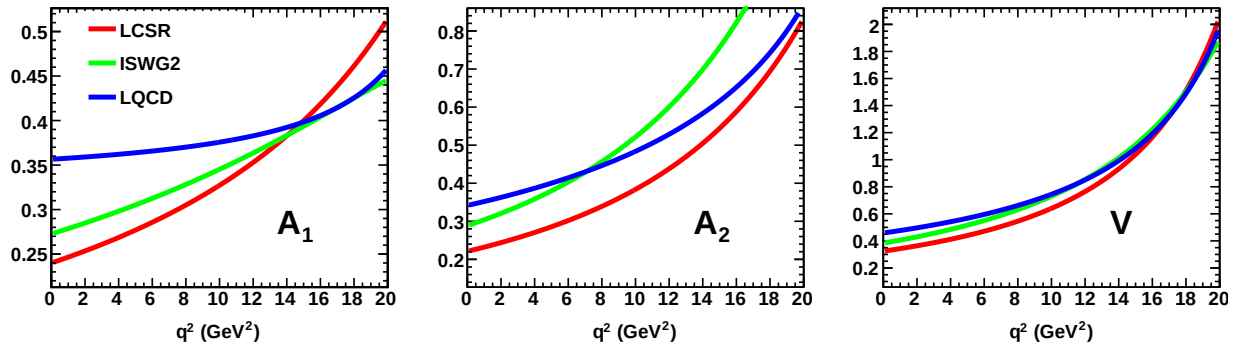

Figure 4.1: Comparisons of the three available FF calculations – ISGW2 [40], LCSR [41] and LQCD [42].

4.1.3 Incorporating background subtraction

Background subtraction can be easily incorporated in the Eq. 4.7 above by weighting the data terms by their correponding Q-values. Thus, our final NLL to minimize are

$$-\ln\mathcal{L}(\vec{x}) = \left[\sum_{i=1}^{N_{data}} Q_i\right] \times \ln\left[\sum_{i=1}^{N_{MC}^{acc}} \frac{dN}{d\phi}\right] - \sum_{i=1}^{N_{data}} Q_i \ln\left[\frac{dN}{d\phi}\right]_i \tag{4.9}$$

We note that here, acceptance correction has been folded into the minimization function itself (the first term in the above equation). Usually, the model-dependance of the acceptance is incorporated in a recursive fashion – one updates the model from a fit to the data, uses the updates the model to regenerate MC, the regenerated MC is used to calculate a new set of accepatnce matrix, and the process is repeated until the final acceptance-corrected results do not change. We have replaced this entire processed by updating the acceptance *during* the angular fit itself.

4.1.4 The Master formula

Finally, we consider constraining the FF shapes to theory calculations. This can be incorporated by adding a χ^2 component to the minimization function f:

$$f = -2\ln\mathcal{L}(\vec{x}) + (\chi^2)_{theory} \tag{4.10}$$

4.2 FF parameterizations

Angular analyses for the $B \to \rho\ell\nu$ case is complicated by several factors compared to $\pi\ell\nu$ (where most of the world analyses exist). First, the ρ is a broad resonance and we have seen from the previous chapter that this enormously complicates the signal-background separation procedure. Second, since the ρ is a vector meson, there are three FF's, which means, thrice

the number of parameters needed in the fits, as compared to the pseudoscalar case. Third, the theory predictions for the FF's are scant and much less reliable here than the $\pi\ell\nu$ case.

Primarily there are three theory calculations available – quark-model based ISGW2 [40], sum-rules [41], and lattice QCD [42]. Fig. 4.1 shows comparisons between the three FF calculations. The ISGW2 and LQCD predictions tend to be more reliable at $q^2 \to q^2_{max}$, while the LCSR predictions apply to $q^2 \to 0$. The LQCD calculations are quenched and treat the ρ as a stable particle, which further dent their reliability. Indeed, it seems that there are no immediate plans in the lattice community to devote resources towards unquenched ρ and ω calculations, since these are extremely difficult.

As apparent from Fig. 4.1, the generic shape of the FF's is a slowly rising behavior with increasing q^2. Fig. 4.2 shows a simple cubic polynomial fit to each of the nine FF shapes (3 for each model). We note that these cubic shapes are not our final parameterizations; Fig. 4.2 merely depicts that individually, the FF's expected to be are well-behaved with smooth functional forms that are easily parameterizable.

However, this does not mean that measuring $A_1(q^2)$, $A_2(q^2)$ and $V(q^2)$ via a fit to the differential rate is trivial for $B \to \rho\ell\nu$. For $B \to \pi\ell\nu$, instead of fitting to $d\Gamma/dq^2$, from Eq. 1.34, one can fit to $\sqrt{(d\Gamma/dq^2)/\mathbf{k}^3}$, which is completely equivalent to fitting to the $f_+(q^2)$ directly. In other words, for the pseudoscalar case, a fit to $d\Gamma/dq^2$ is tantamount to a fit to the form-factor itself.

For the vector meson case, the equivalent would be to extract the first nine moments listed in Table 1.2. For a given value of q^2, these nine numbers uniquely (within statistics) overdetermine the three numerical values of A_1, A_2 and V. In this fashion the functional form of $A_1(q^2)$, $A_2(q^2)$ and $V(q^2)$ can be built up and this would comprise a direct measurement. This is also equivalent to performing a fit to the full differential rate given in Eq. 1.38. Unless this is done, it remains unclear whether one has actually measured the FF themselves, or some ansatz forms of the FF's that somehow have conspired to produce the reduced rates (ie., integrated over one or more variables) that one is measuring.

For $B \to D^*\ell\nu$, HQET helps in simplifying the FF parameterizations from HQET. For the light quark sector, even this is not applicable, which complicates the problem further. Previous CLEO $B \to \rho\ell\nu$ analyses [43] have inspected the problem of being able to differentiate between theory calculations, but severe statistical limitations prohibited an actual fit. On the other hand, CLEO has preliminary fit results in $D \to \rho e\nu$ [44] based on ~ 447 ρ^0 and ~ 304 ρ^+ signal yields. The FF measurements make use of the single-pole form ansatz

$$f(q^2) = \frac{f(0)}{1 - q^2/m_R^2}, \tag{4.11}$$

where the "expectation" is

$$m_A = 5.32 \text{ GeV, and } m_V = 5.68 \text{ GeV}, \tag{4.12}$$

for the $V(A)$ FF's corresponding to the lowest B^* resonances with spin-parity $1^-(1^+)$. Fig. 4.3 shows fits to the model-predictions using a single-pole form with the pole masses fixed to the lowest B^* mass. As expected, the different models have different shapes that

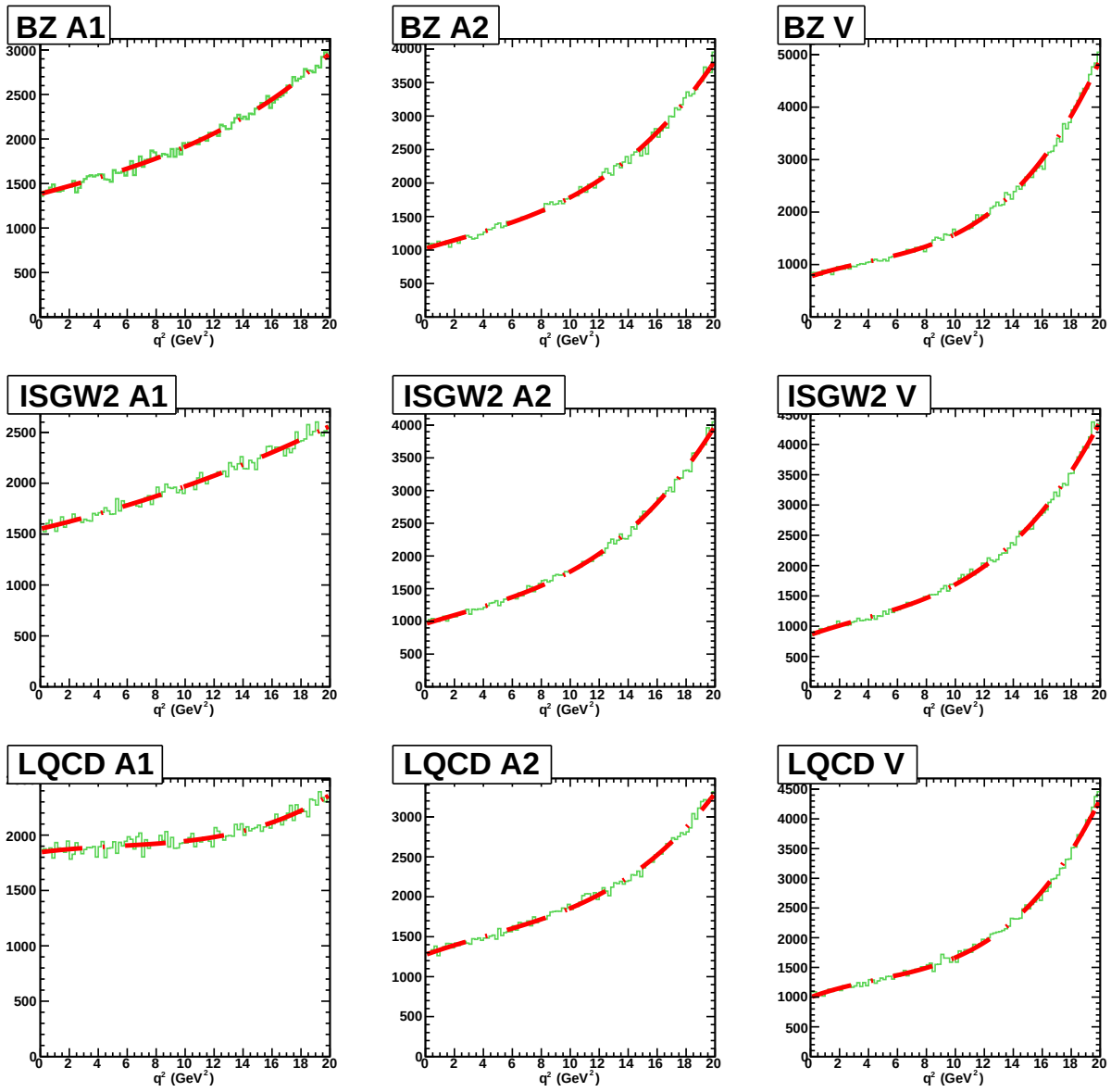

Figure 4.2: Sample fits to the nine FF shapes (three for each model calculation) to a cubic polynomial (red dot-dashed lines).

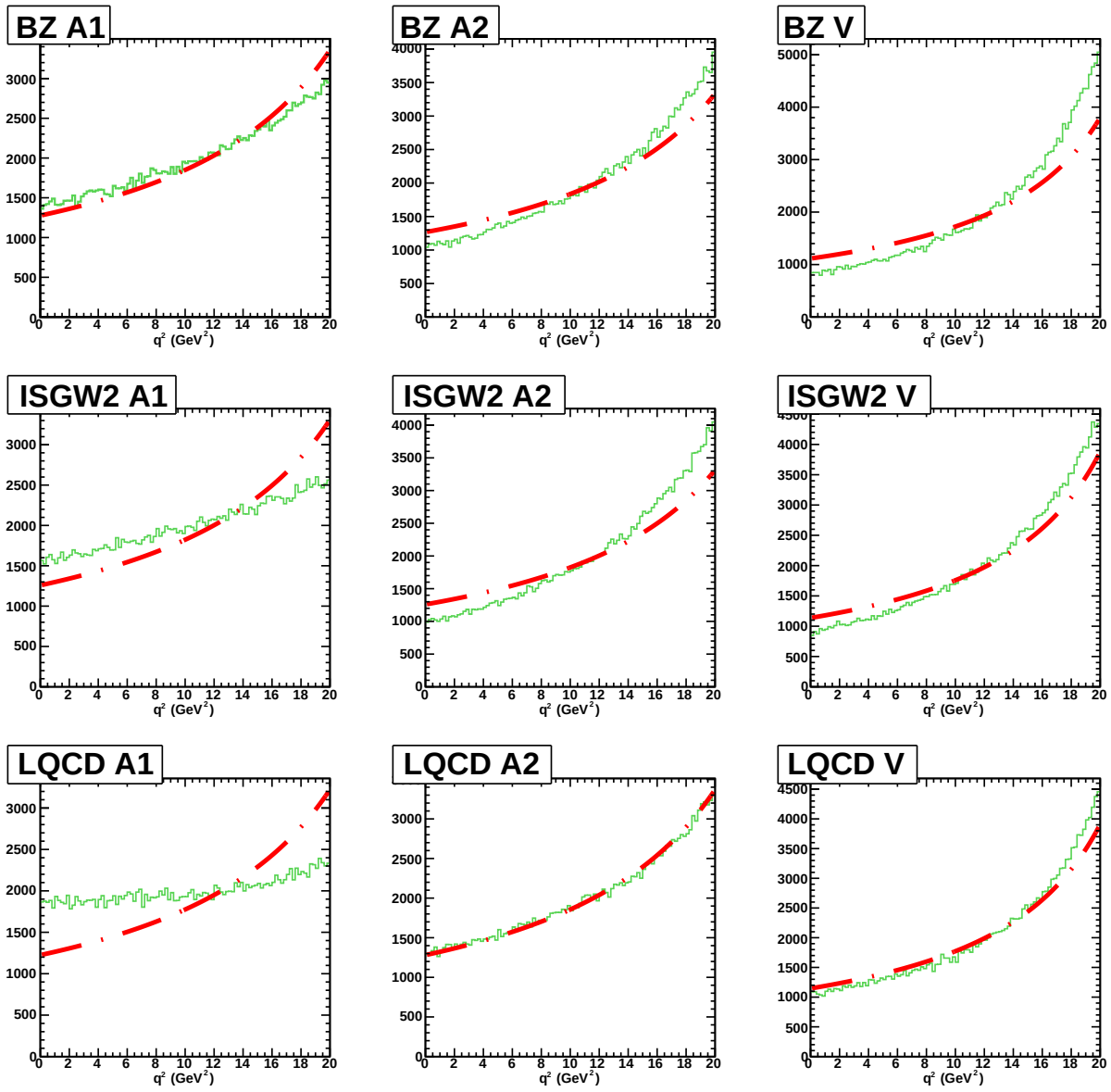

Figure 4.3: Sample fits to the nine FF shapes (three for each model calculation) to a single pole functional form (red dot-dashed lines) with the pole masses fixed to the lowest B^* mass.

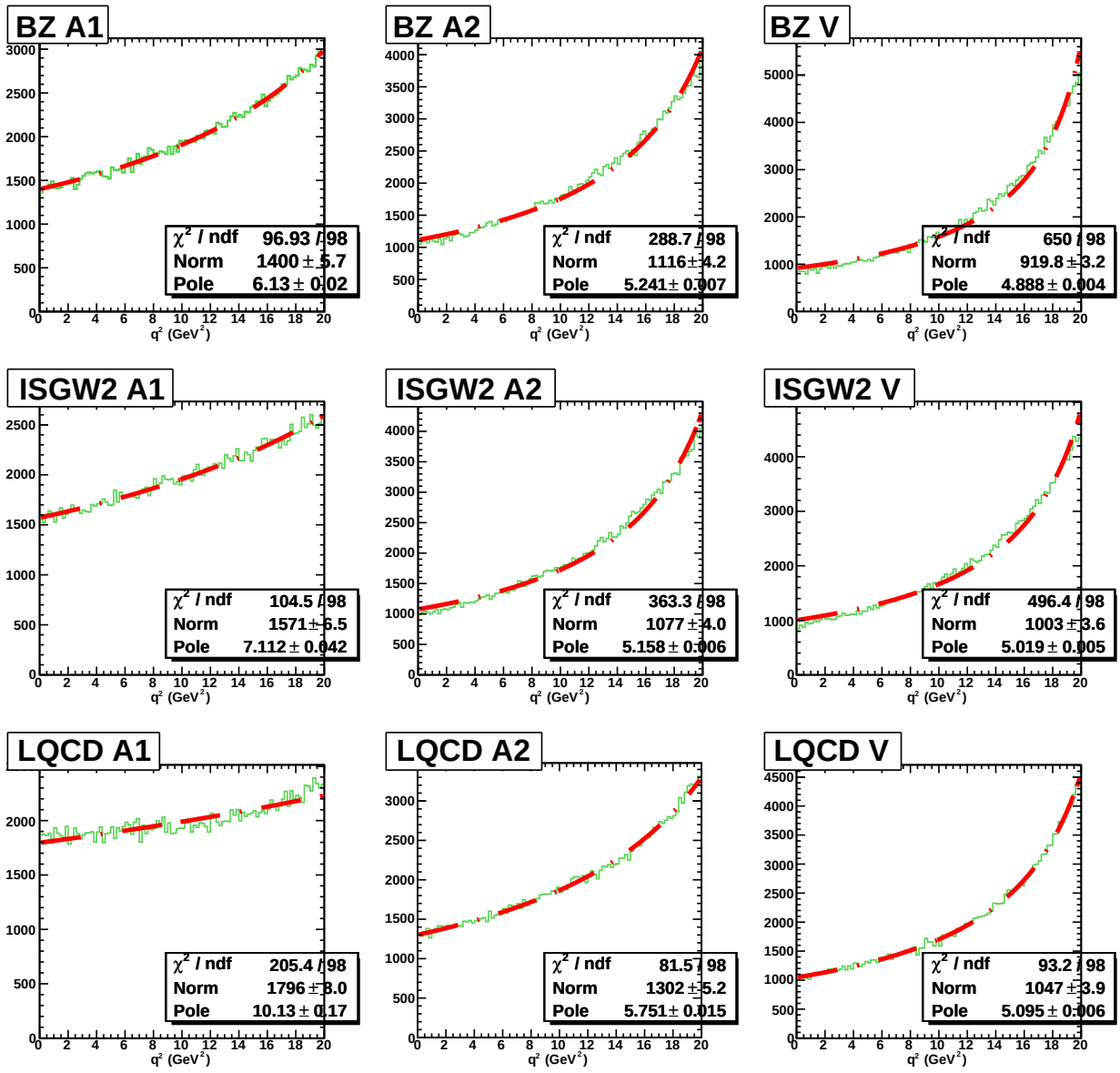

Figure 4.4: Sample fits to the nine FF shapes (three for each model calculation) to a single pole functional form (red dot-dashed lines) with the pole masses kept floating.

Parameter	Result
m_1	7.1
r_2	1.1
m_2	5.2
r_V	1.4
m_V	5.0

Table 4.1: The ISGW2 model single-pole ansatz parameterizations from the fit in Fig. 4.4.

might not conform to the fixed-pole shape. Fig. 4.4 shows the same shapes fit to a single-pole form with the pole masses kept floating. From here, we can conclude that the single-pole form can be used as a "reasonable" approximation if one allows for the pole mass to be taken as a strictly phenomenological term. The χ^2/ndf from the fits show that the the single pole form might not be a perfect ansatz and additional terms would certainly improve the fits. We also note that the higher the curvature of the FF shapes, the smaller is m_R (and vice versa). The LQCD $A_1(q^2)$ shape is almost-flat and leads to a very large effective m_R. Ab initio, we do not know what the curvature of the true FF shapes will be, so it is prudent to allow for a wide enough range during fits to the real data.

If the pole masses are allowed to float in the fit, the single pole ansatz for thre FF's lead to 5 free parameters, since the overall normalization is immaterial in the LH function. Therefore, we choose to normalize everything with respect to $A_1(0)$ and define the define the following fit parameters:

$$r_V = \frac{V(0)}{A_1(0)}, \text{ and } r_2 = \frac{A_2(0)}{A_1(0)} \tag{4.13}$$

Table 4.1 lists the FF parameters for the ISGW2 model from the fit fit results in Fig. 4.4. The signal $B \to \rho\ell\nu$ component in the generic MC used the ISGW2 model. Thus, we take Table 4.1 as the effective "true" results that we want to extract out of our angular fits to the "mock" Data sample constructed out of the MC.

4.3 Sample fits to "mock" Data from MC

4.3.1 Stability checks with TM-ed sample and $\times 10$ statistics

As noted earlier, the angular fit and the signal-background separation are two disjoint problems. In final fits to real data, it is possible that the pathology in one of these feeds into the other. To validate the angular fit in a stand-alone fashion, we first use the full statistics of the truth-matched signal MC component in the generic $B\overline{B}$ MC. That is, we fit to pure signal generated using the ISGW2 FF's, with roughly $\times 10$ statistics as expected in the final data sample. The aim is to validate the usage of Eq. 4.10 for acceptance correction and check stability of the fit results.

Table 4.2 lists the allowed ranges of the five fit variables. The lower bounds of the pole

Parameter	Range
m_1	[4.6,15] GeV
r_2	[0.5,20]
m_2	[4.6,15] GeV
r_V	[0.5,20]
m_V	[4.6,15] GeV

Table 4.2: The allowed ranges and start values of the five fit variables with a single-pole ansatz to the FF shapes.

masses have been kept such that the FF's remain positive at $q^2_{max} \approx 21$ GeV^2. Although we have a rough idea of what the final values of these parameters should be, we test whether the fit itself can pick out "reasonable" values. We run 100 fits with start values randomly chosen inside the ranges listed in Table 4.2. We look at only fits that converges and returns a positive-definite covariant matrix. Fig. 4.5 shows the fit results from one particular fit as 1-D projections – the red markers are the Data points and the blue markers are the MC weighted by the fit results. The results $m_1 = 7.0$, $r_2 = 1.16$, $m_2 = 4.8$, $r_V = 1.65$ and $m_V = 5.0$ are close to the values listed in Table 4.1.

We perform 100 iterations of the fit, choosing random start values of the five parameters within the start-value ranges in Table 4.2. All of the fits converged, while 84 of the fits returned a positve-definite covariance matrix after a `HESSE` step. Fig. 4.6 depicts the stability of the fit results. It is reasonable to conclude that with reasonable statistics and a clean enough data set, robustness in finding a global NLL minimum is not a problem.

4.3.2 Stability checks with TM-ed sample and comparable statistics

The previous sub-section catered to ensuring that in the absence of pathologies from low statistics and background, the fit machinery gives sensible and robust results. We next perform the same checks on the truth-matched signal MC component in the generic MC, with a data sample comparable in statistics to that expected in real Data. Fig. 4.7 shows results of one fit with the extracted parameters: $m_1 = 15.2 \pm 12.2$ GeV, $r_2 = 1.161.2 \pm 0.05$, $m_2 = 5.5 + 0.7$ GeV, $r_V = 0.9 \pm 0.23$ and $m_V = 5.1 \pm 0.5$ GeV. As earlier, red is Data and blue is `FLATQ2` signal MC weighted by the fit results. Fig. 4.8 shows the "islands" of solutions in the five variables. Compared to Fig. 4.6, we see that even without any background we find multiple sets of solutions due to lower statsitics. We also point out that the ISGW2 $A_1(q^2)$ shape is nearly linear – that is, the effective m_1 pole is expected to be large and with low statsitics, the fit simply doesn't find enough discrimination among the different solutions. For fits to real data, if the different sets of solutions yield close enough values of the likelihood function, one can quote all of them as potential solutions. One could also constrain the values of $A_1(0)$, $A_2(0)$ and $V(0)$ to the LCSR values (within errors) and quote that set of solution(s) as well.

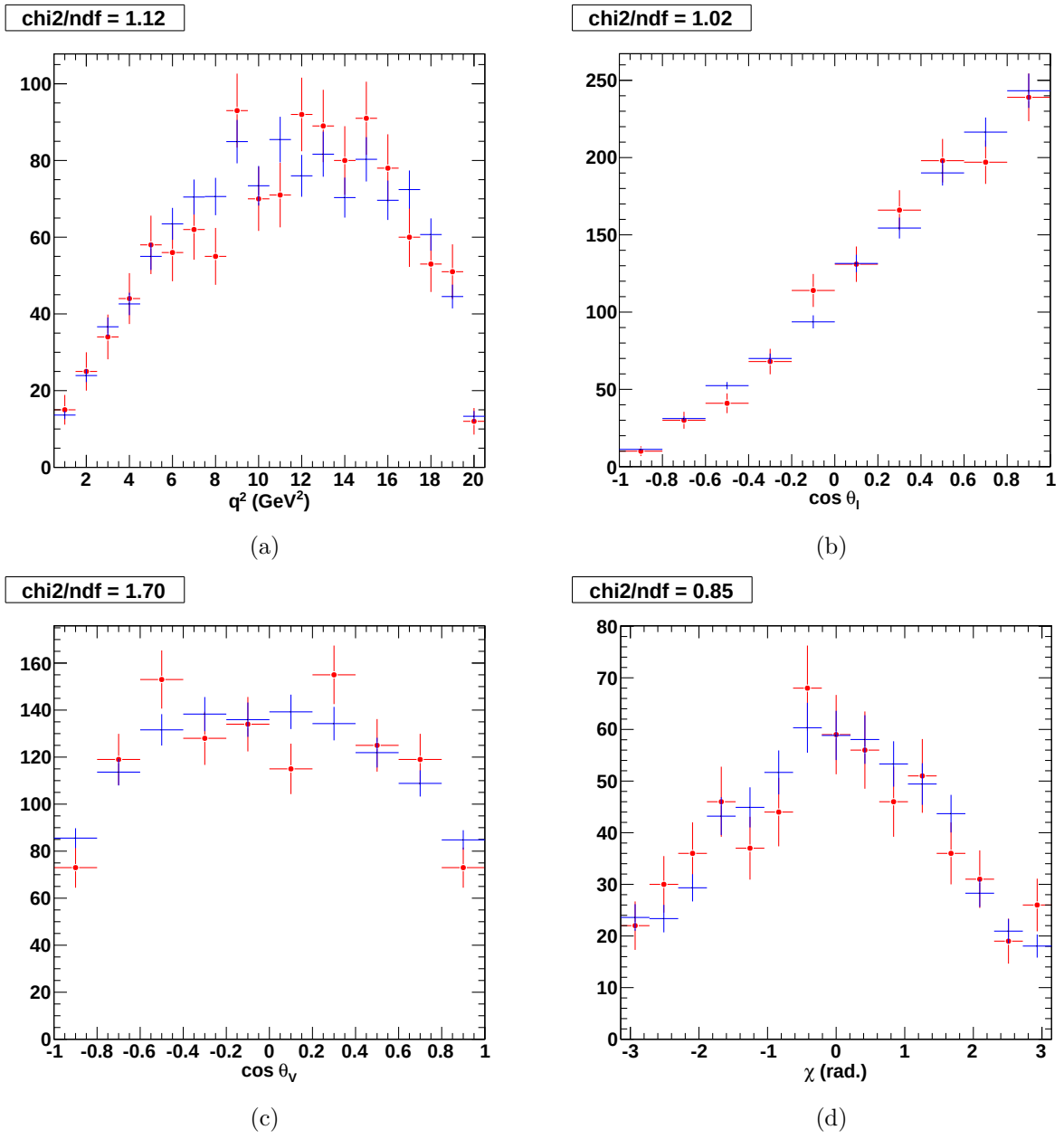

Figure 4.5: 1-D projections of fit results to truth-matched signal MC component in the generic $B\overline{B}$ MC sample using a single-pole ansatz for the FF's: (a) q^2 (b) $\cos\theta_\ell$ (c) $\cos\theta_V$ and (d) χ with $\cos\theta_V < 0$. The extracted parameters are: $m_1 = 7.0$ GeV, $r_2 = 1.16$, $m_2 = 4.8$ GeV, $r_V = 1.65$ and $m_V = 5.0$ GeV.

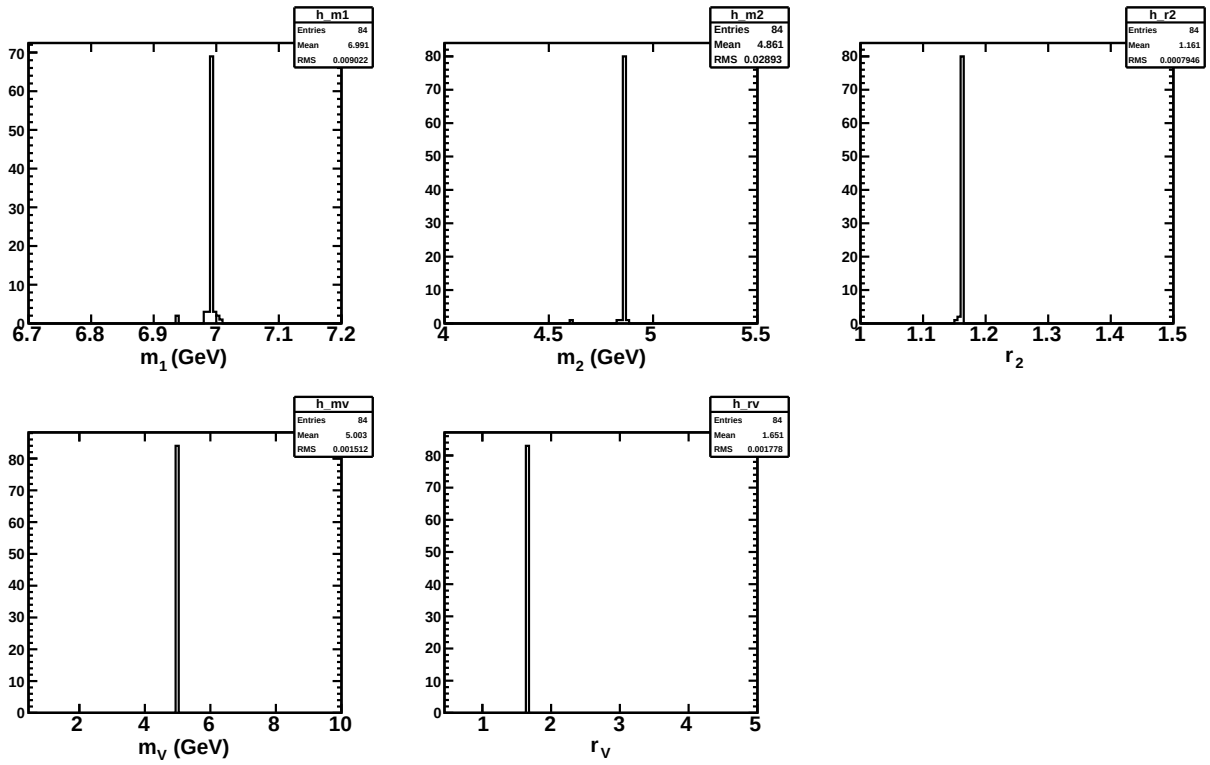

Figure 4.6: The results from 84 well-behaved fits (with random start values) to the full 4-D angular distribution for the TM-ed signal MC with $\times 10$ statistics as Data. Clearly, there is a unique set of solutions which the fits can pull out in a robust fashion.

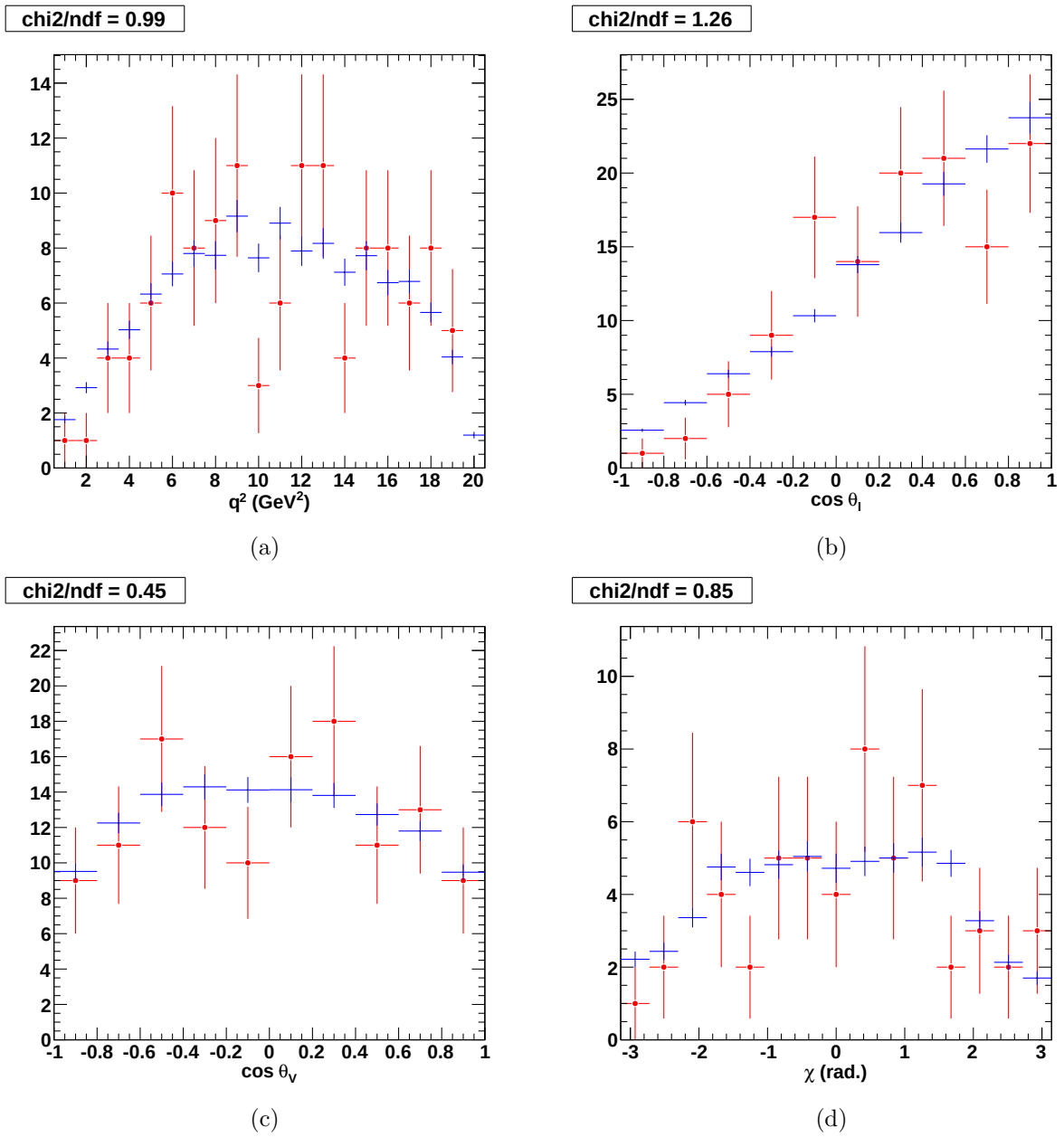

Figure 4.7: 1-D projections of fit results to truth-matched signal MC component in the generic $B\overline{B}$ MC sample using a single-pole ansatz for the FF's: (a) q^2 (b) $\cos\theta_\ell$ (c) $\cos\theta_V$ and (d) χ with $\cos\theta_V < 0$. The extracted parameters are: $m_1 = 15.2 \pm 12.2$ GeV, $r_2 = 1.161.2 \pm 0.05$, $m_2 = 5.5 + 0.7$ GeV, $r_V = 0.9 \pm 0.23$ and $m_V = 5.1 \pm 0.5$ GeV. All errors are statistical.

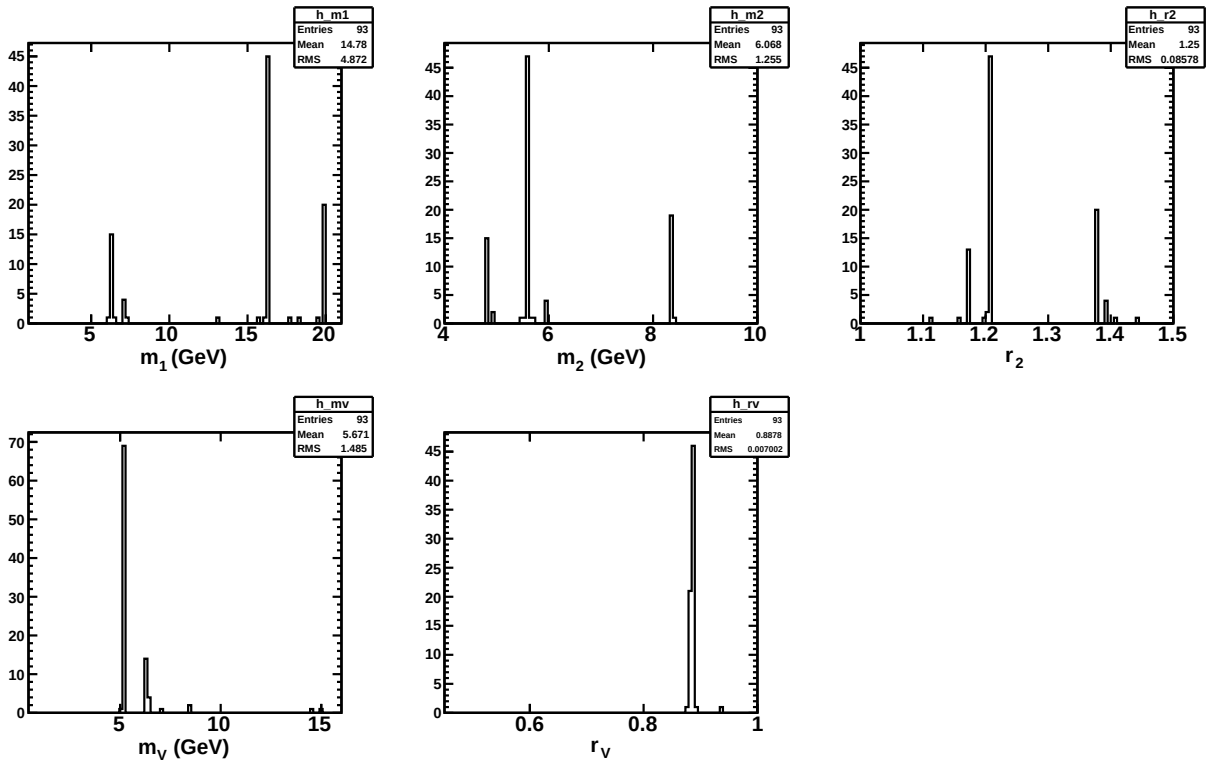

Figure 4.8: The results from well-behaved fits (with random start values) to the full 4-D angular distribution for the TM-ed signal MC with comparable statistics as Data. Note the multiple solutions.

Bibliography

[1] CKMfitter Group (J. Charles). *Eur. Phys. J. C41, 1-131 (2005) [hep-ph/0406184], updated results and plots available at: http://ckmfitter.in2p3.fr.*

[2] Vera Luth. Semileptonic b Meson Decays. *Annual Review of Nuclear and Particle Science*, 61:119–148, 2011.

[3] Philip Urquijo. Semileptonic B_s decays. *ICHEP 2012*, 2012.

[4] Yadong Yang, Hongjun Hao, and Fang Su. Testing the chirality of b to u current with $B^0 \to \rho^- \ell^+ \nu$. *PHYS.LETT.B*, 618(14):97, 2005.

[5] Andreas Crivellin. Effects of right-handed charged currents on the determinations of $|V_{ub}|$ and $|V_{cb}|$. *Phys. Rev. D*, 81:031301, Feb 2010.

[6] G. Isidori A. J. Buras, K. Gemmler. Quark flavour mixing with right-handed currents: an effective theory approach. *Nucl. Phys. B843, arXiv:1007.1993 [hep-ph]]*, pages 107–142, 2011.

[7] Florian Bernlochner. Inclusive Vub: Experimental Mini-Review. *The 7th International Workshop on the CKM Unitarity Triangle*, 2012.

[8] Frederick J. Gilman and Robert L. Singleton. Analysis of semileptonic decays of mesons containing heavy quarks. *Phys. Rev. D*, 41:142–150, Jan 1990.

[9] Jeffrey D. Richman and Patricia R. Burchat. Leptonic and semileptonic decays of charm and bottom hadrons. *Rev. Mod. Phys.*, 67:893–976, Oct 1995.

[10] Jeffrey D. Richman. Heavy-quark physics and CP violation. 1997. Les Houches Session LXVIII.

[11] J.G. Korner and G.A. Schuler. Exclusive semileptonic heavy meson decays including lepton mass effects. *Zeitschrift fur Physik C Particles and Fields*, 46(1):93–109, 1990.

[12] K. Hagiwara, A.D. Martin, and M.F. Wade. Helicity amplitude analysis of $B \to D^* \ell \nu$ decays. *Physics Letters B*, 228(1):144 – 148, 1989.

[13] K. Hagiwara, A.D. Martin, and M.F. Wade. Exclusive semileptonic B-meson decays. *Nuclear Physics B*, 327(3):569 – 594, 1989.

[14] Jong-Phil Lee. CP violating transverse lepton polarization in $B \to D^{(*)}\ell\bar{\nu}$ including tensor interactions. *Physics Letters B*, 526(12):61 – 71, 2002.

[15] Thomas G. Rizzo. Right-handed currents in B decay reexamined. *Phys. Rev. D*, 58:055009, Jul 1998.

[16] Chuan-Hung Chen and Chao-Qiang Geng. Charged Higgs on $B^- \to \tau\bar{\nu}_\tau$ and $\bar{b} \to p(v)\ell\bar{\nu}_\ell$. *JHEP0610:053*, 2006.

[17] J.G. Korner, K. Schilcher, and Y.L. Wu. T-odd and CP-odd triple momentum correlations in the exclusive semi-leptonic bottom meson decay $B \to D^*\ell\nu_\ell$. *Physics Letters B*, 242(1):119 – 127, 1990.

[18] I.A. Balakireva, N.V. Nikitin, and D.A. Tlisov. Asymmetries in rare radiative leptonic and semileptonic decays of B mesons. *Physics of Atomic Nuclei*, 73(10):1713–1739, 2010.

[19] C. S. Kim, Jake Lee, and W. Namgung. CP violation in the semileptonic B_{l4} decays $B^\pm \to \pi^+\pi^- l^\pm\nu$. *Phys. Rev. D*, 60:094019, Oct 1999.

[20] C. S. Kim, Jake Lee, and W. Namgung. CP violation in the semileptonic $b_{l4}(B \to D\pi\ell\nu)$ decays: A model independent analysis. *Phys. Rev. D*, 59:114005, Apr 1999.

[21] C. S. Kim, Jake Lee, and W. Namgung. CP violation in the semileptonic $B_{l4}(B \to D\pi\ell\nu)$ decays: Multi-Higgs-doublet model and scalar-leptoquark models. *Phys. Rev. D*, 59:114006, Apr 1999.

[22] Robert Garisto. CP-violating polarizations in semileptonic heavy meson decays. *Phys. Rev. D*, 51:1107–1116, Feb 1995.

[23] P. Castoldi, J.-M. Frère, and G. L. Kane. How to elucidate the mechanism of CP violation. *Phys. Rev. D*, 39:2633–2638, May 1989.

[24] Guo-Hong Wu, Ken Kiers, and John N. Ng. Polarization measurements and T violation in exclusive semileptonic B decays. *Phys. Rev. D*, 56:5413–5430, Nov 1997.

[25] Guo-Hong Wu, Ken Kiers, and John N. Ng. Testing time reversal invariance in exclusive semileptonic B meson decays. *Physics Letters B*, 402(12):159 – 166, 1997.

[26] Andrzej J. Buras, Katrin Gemmler, and Gino Isidori. Quark flavour mixing with right-handed currents: An effective theory approach. *Nuclear Physics B*, 843(1):107 – 142, 2011.

[27] Katrin M. Gemmler. TUM PhD thesis, Two Complementary Approaches to Right-Handed Currents.

[28] Chuan-Hung Chen and Soo hyeon Nam. Left-right mixing on leptonic and semileptonic $b \to u$ decays. *Physics Letters B*, 666(5):462 – 466, 2008.

[29] Chuan-Hung Chen and Chao-Qiang Geng. Lepton angular asymmetries in semileptonic charmful B decays. *Phys. Rev. D*, 71:077501, Apr 2005.

[30] Daniele del Re *et al.*. Semi-exclusive B reconstruction. *BAD271.*

[31] Manuel Franco Sevilla, David Lopes Pegna, and Vera Luth. Observation of the exclusive semileptonic decay $B \to D\tau^-\bar{\nu}_\tau$ and measurement of $R(D^{(*)})$. *BAD2201 and BAD2467.*

[32] D. M. Lindemann and S. H. Robertson. A search for the rare decay $B \to K^{(*)}\nu\bar{\nu}$ using hadronic tag reconstruction. *BAD2435.*

[33] CLEO Collaboration. First measurement of the Form Factors in the Decays $D^0 \to \rho^- e^+ \nu_e$ and $D^+ \to \rho^0 e^+ \nu_e$. *arXiv:1112.2884 [hep-ex].*

[34] Chunlei Liu. Semileptonic Charm Decays: mini review. *arXiv:1302.0227 [hep-ex].*

[35] D. Bernard *et al.*. Exclusive B Reconstruction into Charmonium Final States: Status Report, Appendix B. *BAD12*, 2000.

[36] W. D. Hulsbergen. Decay chain fitting with a Kalman lter. *Nuclear Instruments and Methods in Physics Research A*, 552:556, 2005.

[37] del Amo Sanchez *et al.*. Study of $B \to \pi l\nu$ and $B \to \rho l\nu$ decays and determination of $|V_{ub}|$. *Phys. Rev. D*, 83:032007, Feb 2011.

[38] R. J. Morrison D. M. Schmidt and M. S. Witherell. *Nucl. Instrum. Meth. A 328, 547 (1993).*

[39] S. U. Chung. Formulas for Partial-Wave Analysis. 2010.

[40] Daryl Scora and Nathan Isgur. Semileptonic meson decays in the quark model: An update. *Phys. Rev. D*, 52:2783–2812, Sep 1995.

[41] Patricia Ball and Roman Zwicky. $B_{d,s}to\rho, \omega, K^*, \phi$ decay form factors from light-cone sum rules reexamined. *Phys. Rev. D*, 71:014029, Jan 2005.

[42] UKQCD Collaboration, Luigi Del Debbio, Jonathan M. Flynn, Laurent Lellouch, and Juan Nieves. Lattice-Constrained Parametrizations of Form Factors for Semileptonic and Rare Radiative B Decays. *PHYS.LETT.B*, 416:392, 1998.

[43] David J. Lange. UCSB PhD thesis, Rare exclusive semileptonic decays at CLEO. 1999.

[44] S. Dobbs *et al.*. First Measurement of the Form Factors in the Decays $D^0 \to \rho^- e^+ \nu_e$ and $D^+ \to \rho^0 e^+ \nu_e$. *arXiv:1112.2884v1*, 2011.